NASA/CR—2014-216674

AG Channel Measurement and Modeling Results for Over-Sea Conditions

David W. Matolak and Ruoyu Sun
University of South Carolina, Columbia, South Carolina

June 2014

NASA STI Program . . . in Profile

Since its founding, NASA has been dedicated to the advancement of aeronautics and space science. The NASA Scientific and Technical Information (STI) program plays a key part in helping NASA maintain this important role.

The NASA STI Program operates under the auspices of the Agency Chief Information Officer. It collects, organizes, provides for archiving, and disseminates NASA's STI. The NASA STI program provides access to the NASA Aeronautics and Space Database and its public interface, the NASA Technical Reports Server, thus providing one of the largest collections of aeronautical and space science STI in the world. Results are published in both non-NASA channels and by NASA in the NASA STI Report Series, which includes the following report types:

- TECHNICAL PUBLICATION. Reports of completed research or a major significant phase of research that present the results of NASA programs and include extensive data or theoretical analysis. Includes compilations of significant scientific and technical data and information deemed to be of continuing reference value. NASA counterpart of peer-reviewed formal professional papers but has less stringent limitations on manuscript length and extent of graphic presentations.

- TECHNICAL MEMORANDUM. Scientific and technical findings that are preliminary or of specialized interest, e.g., quick release reports, working papers, and bibliographies that contain minimal annotation. Does not contain extensive analysis.

- CONTRACTOR REPORT. Scientific and technical findings by NASA-sponsored contractors and grantees.

- CONFERENCE PUBLICATION. Collected papers from scientific and technical conferences, symposia, seminars, or other meetings sponsored or cosponsored by NASA.

- SPECIAL PUBLICATION. Scientific, technical, or historical information from NASA programs, projects, and missions, often concerned with subjects having substantial public interest.

- TECHNICAL TRANSLATION. English-language translations of foreign scientific and technical material pertinent to NASA's mission.

Specialized services also include creating custom thesauri, building customized databases, organizing and publishing research results.

For more information about the NASA STI program, see the following:

- Access the NASA STI program home page at *http://www.sti.nasa.gov*

- E-mail your question to *help@sti.nasa.gov*

- Fax your question to the NASA STI Information Desk at 443–757–5803

- Phone the NASA STI Information Desk at 443–757–5802

- Write to:
  STI Information Desk
  NASA Center for AeroSpace Information
  7115 Standard Drive
  Hanover, MD 21076–1320

NASA/CR—2014-216674

AG Channel Measurement and Modeling Results for Over-Sea Conditions

David W. Matolak and Ruoyu Sun
University of South Carolina, Columbia, South Carolina

Prepared under Grant NXX12AR56G

National Aeronautics and
Space Administration

Glenn Research Center
Cleveland, Ohio 44135

June 2014

Level of Review: This material has been technically reviewed by NASA technical management OR expert reviewer(s).

Available from

NASA Center for Aerospace Information
7115 Standard Drive
Hanover, MD 21076–1320

National Technical Information Service
5301 Shawnee Road
Alexandria, VA 22312

Available electronically at http://www.sti.nasa.gov

AG Channel Measurement and Modeling Results for Over-Sea Conditions

David W. Matolak and Ruoyu Sun
University of South Carolina
Columbia, South Carolina 29208

Abstract

This report describes results from flight tests conducted in an over-sea environment, for the purpose of characterizing the air-to-ground (AG) channel, for future unmanned aircraft system (UAS) communication system analysis and design. These results are for the first of a set of several flight tests conducted in different ground site (GS) environments. An ultimate aim of all these tests is the development of models for the AG channel that can be used in communication system evaluation. In this report we provide measured results for propagation path loss, root-mean square delay spread (RMS-DS), and the correlation coefficient of the primary received signal components on the four antennas (two antennas for C-band, two for L-band). For path loss, the curved-earth two-ray model provides a reasonable fit to the measured data, altered by several dB at the shortest link distances by aircraft antenna pattern effects. This two-ray model also accounts for the majority of measured RMS-DS results of a few tens of nanoseconds, except for the occasional intermittent reflections from surface objects. These intermittent reflections yield RMS-DS values up to several hundred nanoseconds. For portions of the flight path that were over a harbor area highly populated with boats, the channel was found to be more "continuously dispersive," with RMS-DS reaching approximately 250 ns. A separate model will be developed for this over-harbor setting. The correlation coefficient results are still undergoing analysis; *preliminary* observations are that correlation between signals on the same-band antennas is generally large (>0.6) for the C-band straight flight paths, whereas for the L-band signals and for the oval-shaped flight paths the correlation is generally small (below 0.4). Inter-band correlations are typically very small, and are well modeled as zero-mean Gaussian in distribution, with a standard deviation less than 0.2. Hence the over-sea channel effects in the two bands can be considered uncorrelated, which will allow for good diversity gains in dual-band systems. We describe initial modeling approaches for the over-sea channel; complete models for this and the over-harbor setting will appear in a subsequent report.

1. Introduction

In this report we provide results from measurements for the air-ground (AG) channel taken in one specific environment: the over-sea setting. This is one of several environments in which these measurements were taken [1]-[5]. In principle, this environment represents one of the simplest possible, in that the ground site (GS) was placed near the coastline with a clear view to the ocean, and the flight paths taken by the test aircraft were primarily over the ocean. Hence the AG channel contains a line-of-sight (LOS) component, a surface reflection, and during some portions of the flight, multipath components (MPCs) from other ground or surface-based obstacles in the environment.

The aim of these measurements was to collect power delay profiles (PDPs) that enable estimation of the AG channel impulse response (CIR). From these PDPs we can also determine propagation path loss. For PDPs collected over various time periods—corresponding to portions of flights at different elevation angles, different trajectories with respect to the direct GS-to-aircraft line, and different aircraft attitudes—we can also track PDPs over time. These are of direct value in constructing models for the time-varying AG channel.

Observations of the measurement data also revealed that in addition to the channel sounder's (internal) thermal noise, there exists an additional noise source (or sources) that alters the noise distribution seen in received PDPs. This additional noise is most likely due to aircraft electronics. Since this secondary noise has peak values well above the mean of the sounder's thermal noise, samples of this secondary noise that appear in PDPs with relatively low signal power can be more easily mistaken for MPCs than such samples emanating from the sounder's thermal noise.

Thus we have also performed an analysis and characterization of both the internal and secondary noise sources, and from this, have developed additional thresholding steps to eliminate these noise samples before processing PDPs for channel statistics.

The remainder of this report is organized as follows: Section 2 describes the over-sea measurement environment and flight conditions, and Section 3 provides analysis of the measured over-sea data. This analysis focuses on path loss and root mean-square delay spread (RMS-DS), the most common measure of the temporal spread of the CIR. We also provide some initial results on correlation between MPCs and across frequency bands. Section 4 provides initial channel modeling results, and in Section 5 we provide an update to the project literature review. Section 6 provides the conclusion. The report also contains three appendices: Appendix A contains results for the flight tracks not described in the report's main body; in Appendix B we describe the noise characterization; and in Appendix C we describe the noise removal algorithms.

2. Over-Sea Measurement Environment and Flight Conditions

For the over-sea measurements, the GS transmitter (Tx) was located in Oxnard, California, close to the beach bordering the ocean. The location of the Tx was latitude (*lat*) 34.177022, longitude (*long*) -119.235386, and altitude (*alt*) 23.4696 m, with *lat* and *long* values in degrees. The GS altitude is that of the antenna (~3.66 m elevation + 19.81 m antenna mast height). Both C- and L-band GS antennas were directed due west (270 degrees from magnetic north) with zero elevation angle. The magnetic declination was 12.65 degrees for Oxnard, CA, USA on 11 June 2013 according to the National Geographical Data Center [6]. (Magnetic declination is the angle between magnetic north and geographic north, with magnetic north ahead of geographic north clockwise denoting a positive declination.) The GS antennas directed to azimuth 283 degrees (from geographic north) and elevation 0 degrees were used to calculate the GS antenna's gains.

It was a clear day on 11 June 2013 for Oxnard, CA. The temperature was 14.4-21.1 degree Celsius according to the National Climate Data Center [7]. The test was conducted from approximately 9:53:01 am to 12:17:02 pm Pacific Standard Time. The total measurement time duration was 8641 seconds, approximately 2 hours and 24 minutes. Twelve (12) tracks of data were recorded, where each track represents a flight path or a portion of a flight path; many tracks cover nearly the same flight patterns. The altitude of the aircraft ranged from 783.5 m to 807.3 m, and link distance ranged from 776 m to 52,182 m; valid channel sounding data is generally limited to approximately 25 km for C-band, and approximately 52 km for L-band.

Figure 1 shows photographs of the GS environment, both looking toward the ocean, and looking from the beach toward the GS. The GS location was an empty lot, with some palm trees nearby, and some low-rise buildings to the rear.

Figure 1. Photographs of GS location, Oxnard, CA, 11 June 2013: view toward ocean (left), & view from beach toward GS (right).

The aircraft coordinates (lat, long, alt) were converted to East-North-Up (ENU) coordinates with the GS Tx as the reference point. Azimuth and elevation angle from the GS to the aircraft are then easily generated in the ENU frame. Figure 2 shows Google maps® views of the flight tracks. The red tracks with*out* a number suffix (e.g., "_*i*" for *i* from 1 to 12) in each figure denote flight paths during which no channel measurement data was taken. The basic flight paths were in a line directly away from (or toward) the GS over the Pacific ocean, or followed an oval-shaped path. This oval pattern allowed the orientation of the aircraft antennas with respect to the GS to change by a full 360 degrees. The aircraft was flown as level as possible for each track.

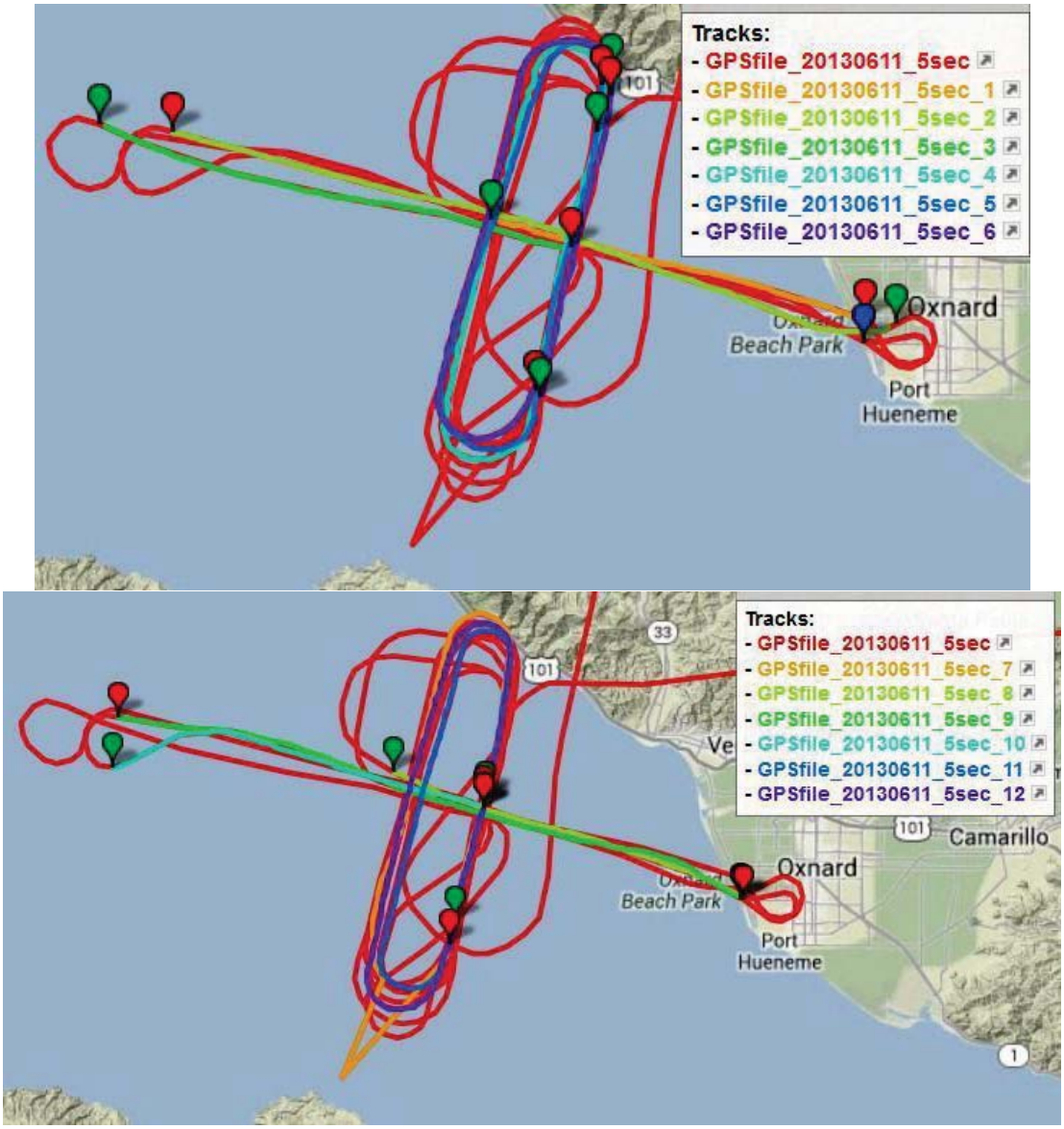

Figure 2. Flight tracks in Google Maps view. Top figure shows tracks 1-6, bottom figure shows tracks 7-12.

Figure 3 shows traces of several geometric parameters for all the flight tracks during the test: the flight tracks themselves in earth-centered, earth-fixed (ECEF) coordinates, the difference in altitude between the GS and the aircraft, the azimuth angle, and the elevation angle. These parameters provide useful information on the ranges of conditions, and enable us to bound effects such as GS antenna gains and surface reflection coefficients.

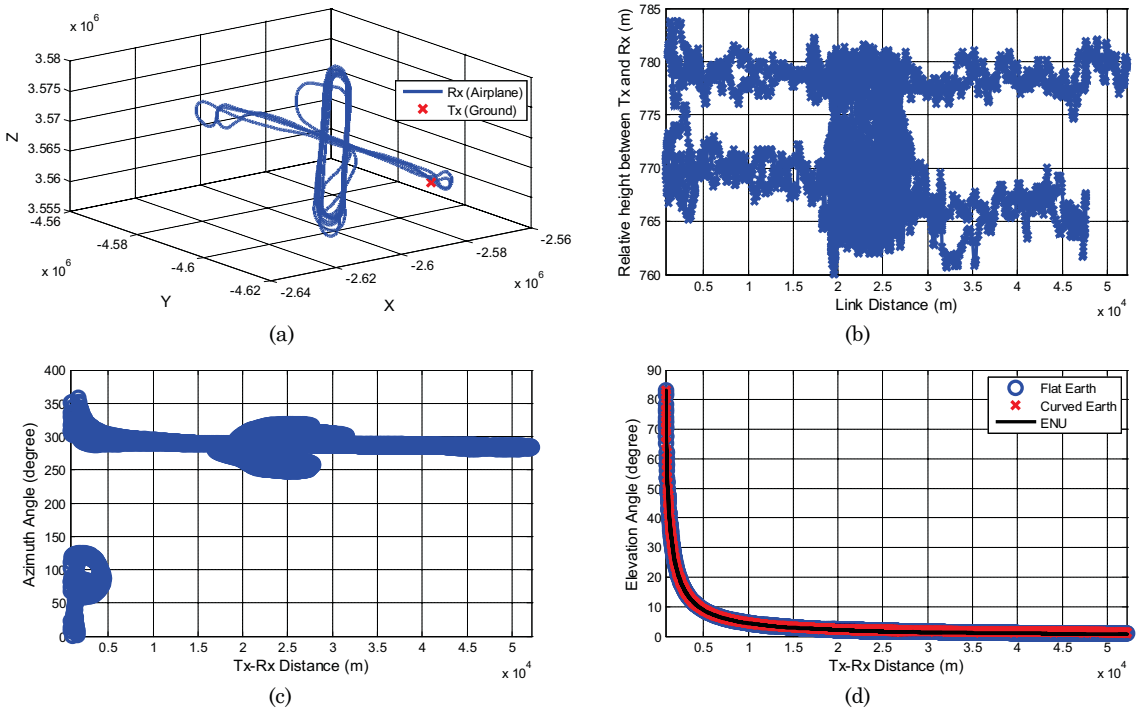

Figure 3. Geometric traces for flight tracks 1-12. (a) flight tracks in ECEF coordinates; (b) altitude difference between aircraft and ground station; (c) azimuth angle; (d) elevation angle.

3. Over-Sea Data Analysis

Data files in all tracks were segmented into blocks of 10,000 PDPs to facilitate processing. In our processing routines, for one of these 10,000-PDP files, it takes approximately 100 seconds to calculate our initial channel statistics (path loss and RMS-DS). There are 6709 files (66,956,474 PDPs) for the Oxnard tests in total. Processing all files for one receiver required approximately 46.6 hours; processing for all four receivers required approximately 186.4 hours. Additional processing steps, necessary for example for computing other channel characteristics and for thresholding noise, take additional time.

Sounder data is collected in short segments of several minutes, and with the sounder recording at a rate of approximately 2100 PDPs per second, many PDPs are recorded in each data file. For analysis, NASA (J. Ishac) has created software that scans the original files, removes any corrupted data, and as noted, parses the files into blocks of size 10,000 PDPs each; this pre-processing greatly facilitates our analysis. Subsequently, we align the PDP data with GPS data, confirm that received power is above threshold, time-align the PDPs, then compute our CIR statistics. A more comprehensive and formal algorithm that describes our processing procedures in detail is currently under development.

In this section we describe results for several flight tracks (FTs) in detail; results for the remaining FTs are described in Appendix A. The FTs described in this section were selected as representative of the over-sea conditions for various link distances and aircraft locations. Before describing our measurement results, we first provide a brief discussion on anomalous propagation conditions that can occur in over-sea transmission.

3.1 Over-Sea Propagation

The propagation of radio signals in over-sea environments has been studied for decades, for a wide range of frequencies, for both communications and radar applications. Despite the fact that the ocean usually offers a very open setting, meteorological conditions can yield atypical propagation effects. For signals from VHF through EHF, anomalous conditions can occur. This includes increased attenuation from hydrometeors and atmospheric gases, which can also occur over land. As noted in [1], these effects are essentially negligible at frequencies below about 10 GHz. For example, for a 30 km link, a 5 GHz signal will be attenuated by no more than 1.2 dB from atmospheric gases, and a 970 MHz signal by approximately half that amount. For the same 30 km path, heavy rainfall (100 mm/hr) can add up to 12 dB of attenuation at 5 GHz (0.4 dB/km), if the rain is uniformly heavy throughout the entire signal path, and again for L-band, the attenuation due to rain is negligible, approximately 0.3 dB (0.01 dB/km) for a 30 km link uniformly filled with heavy rain. Uniform heavy rainfall over such a wide area is also a rather rare condition except in severe tropical storms. More moderate rain rates (e.g., 10 mm/hr) reduce these dB-per-km attenuation rates by over a factor of twenty. Since no appreciable precipitation occurred during our flight testing, we can neglect these effects entirely for our data set.

An opposite effect—signal enhancement—can result from the propagation condition known as ducting. Given some of our observed path loss results in this set of over-sea measurements—which showed slightly smaller values of propagation path loss than expected—we investigated this phenomenon further. In [1], we provided a brief description of ducting, upon which we expand here.

Ducting can occur over land, usually from temperature inversions where cold dense air underlies warm air. Over water, ducting is far more common. These ducts act as leaky waveguides that can reduce signal attenuation below free-space path loss values. Ducting occurs during "anomalous" conditions where the index of refraction's variation with altitude changes from its usual functional form (exponentially decreasing with altitude). The presence of a duct depends upon various meteorological factors, including air and sea surface temperature, humidity, wind speed, etc. Multiple models for ducts exist [8], but obtaining all the local meteorological data for the model inputs is not always practical. The three types of ducts are evaporation ducts, surface ducts, and elevated ducts. The evaporation duct forms from the high humidity just above the water surface. These ducts are nearly always present, and can reach heights up to approximately 30-40 m, but much more typical heights are on the order of 12 m [9]. Since the duct essentially "traps" the transmitted signal, any evaporation ducts will not enhance propagation from a low-height ground station to an aircraft well above the maximum 40 m duct altitude. Worth noting is that, like conventional waveguides, ducts also have a lower frequency limit: this is typically about 100 MHz for surface and elevated ducts, but is near 2 GHz for evaporation ducts [10], [11], hence the evaporation duct would not enhance our L-band signals. The surface duct height can begin at the sea surface, or can begin at heights up to a few hundred meters [12]. The extent of the duct is typically no more than 150 meters in height and occurs with a probability of approximately 0.2 in the Pacific ocean near Oxnard [13]. As with the evaporation duct, propagation from the Oxnard ground site to the aircraft would be extremely unlikely to occur through a surface duct, since the aircraft altitude is well above the typical maximum surface duct height. The last type of duct, the elevated duct, appears as a trapping layer at some altitude above the earth, typically several hundred meters or more. Hence ground-based transmissions cannot generally couple into them, although airborne transmissions can. Elevated ducts can also be observed over land masses, although less commonly [14]. The ITU Recommendation P.834 [15] has information on ducting, in particular the elevation angle below which ground-based transmissions can be trapped by surface ducts, and the frequency above which such trapping can occur for both elevated and surface ducts. Both these parameters require knowledge of the local refractivity gradient as a function of altitude, which as noted, is not always available.

We have found two relatively recent papers that claim to have observed ducting effects in over-sea transmissions in an air-to-ground measurement [16], [17]; both references use the same

measurement data at 5.7 GHz, taken over the South China Sea. In [16], the authors report two-ray path loss effects for aircraft altitudes of 370 m, 910 m, and 1830 m with ground station antenna heights of 5.5 and 6.5 m. Path losses up to 10 dB smaller than that predicted by the two-ray model were reported, but this phenomenon was not discussed in detail in [16]. Worth noting is that the two-ray "lobing" effect was only partially present in the measured data in [16]; the authors also claim existence of a significant 3rd propagating ray, present up to approximately 5% of the time, and likely attributable to sea-surface roughness, or possibly to large ships or structures on the sea surface. Some of the multipath results in [16] though do not withstand a careful geometric analysis. For what appears to be a minimum link distance of 50 km, the maximum aircraft and ground site altitudes yield a two-ray path length difference of at most 0.44 m, which corresponds to a delay difference of approximately 1.5 ns; results in [16] show an example delay difference of over 100 ns for the primary reflected ray (and 1 microsecond for the 3rd ray), hence the example PDP shown in [16] is likely erroneous, as it is not possible for the measurement conditions described. Reported values of RMS-DS in [16] range from 20 to 480 ns. Only the values near the lower end of this range are realistic for these link distances and platform heights, when accounting for surface reflections. Reflections can occur from other large obstacles in the environment (e.g., large mountains—not present in this environment—or very large and distant buildings), but discussion of this possibility is absent in [16]. Actual delay values for the measured MPCs were not reported in [16].

In [17], these authors analyze the path loss data more closely, and claim that the reduced path loss (with respect to free-space) is due to coupling into and out of two ducts: an elevated duct near or below the aircraft, and the evaporation duct at the surface. Although the environment in this tropical area is indeed conducive to the presence of these ducts (i.e., probability of an elevated duct is near 10% for this area [13]), the propagation mechanism proposed in [17] is questionable. This mechanism is described as propagation from the aircraft through the air above the elevated duct, coupling into and propagation through this elevated duct, leakage out of this elevated duct and propagation through the air between the two ducts, then finally coupling into the evaporation duct to the ground site. Since ducts tend to "trap" energy, once the signal enters the duct, the amount that leaks through is unlikely to have appreciable strength. Also as noted in [9], the best coupling occurs when the antennas are within or very near the duct, and measured enhancements in this "best-coupling" condition very rarely reach 10 dB at the 5 GHz frequency used in [17]. Thus the physical description of the reduced path loss in these results is not convincing. It is possible for elevated ducts to have a "rising elevation" profile, and this type of structure could have allowed near perfect coupling from the aircraft to the GS in the measurements of [16] and [17]. Although this has been conjectured in [11], to our knowledge [11] is the only such paper to propose such an effect to obtain agreement with measured results. We believe that no significant ducting effects were present for our Oxnard flight tests.

Sea-surface roughness can also affect propagation results. Due to the roughness of the sea surface, the surface reflection is rarely specular, i.e., the sea-surface "reflection" is actually the incident signal scattered in multiple directions. This has the effect of reducing the depths of the nulls in the two-ray model's path gain, since the scattered component that reaches the receiver is smaller than that of a specular reflection. The sea roughness also changes the path length followed by the scattered component, and this has the effect of shifting the two-ray path gain nulls along the distance axis. This roughness effect can be approximated by a modification to the typical reflection coefficient magnitude. This modification assumes that the surface roughness can be modeled as Gaussian in distribution, and requires only one additional input to modify the two-ray models (both the flat-earth, and curved-earth two-ray models): the standard deviation of surface height. The modification multiplies the standard two-ray reflection coefficient magnitude by a roughness correction factor, which can be found in [11] and [18]. We employ this in some of our results, using estimated values of the standard deviation of sea surface height.

3.2 Flight Track 1

Figure 4 shows the geometric traces for FT1, in which the aircraft flew directly toward the GS. The total altitude variation was approximately 6 m. The azimuth angle (measured clockwise from geographic north with the GS as reference) was mostly near 300 degrees, and the elevation angle gradually decreased as the link distance increased. We also include plots of aircraft heading, pitch, and roll angles, computed from the aircraft's flight data recorder.

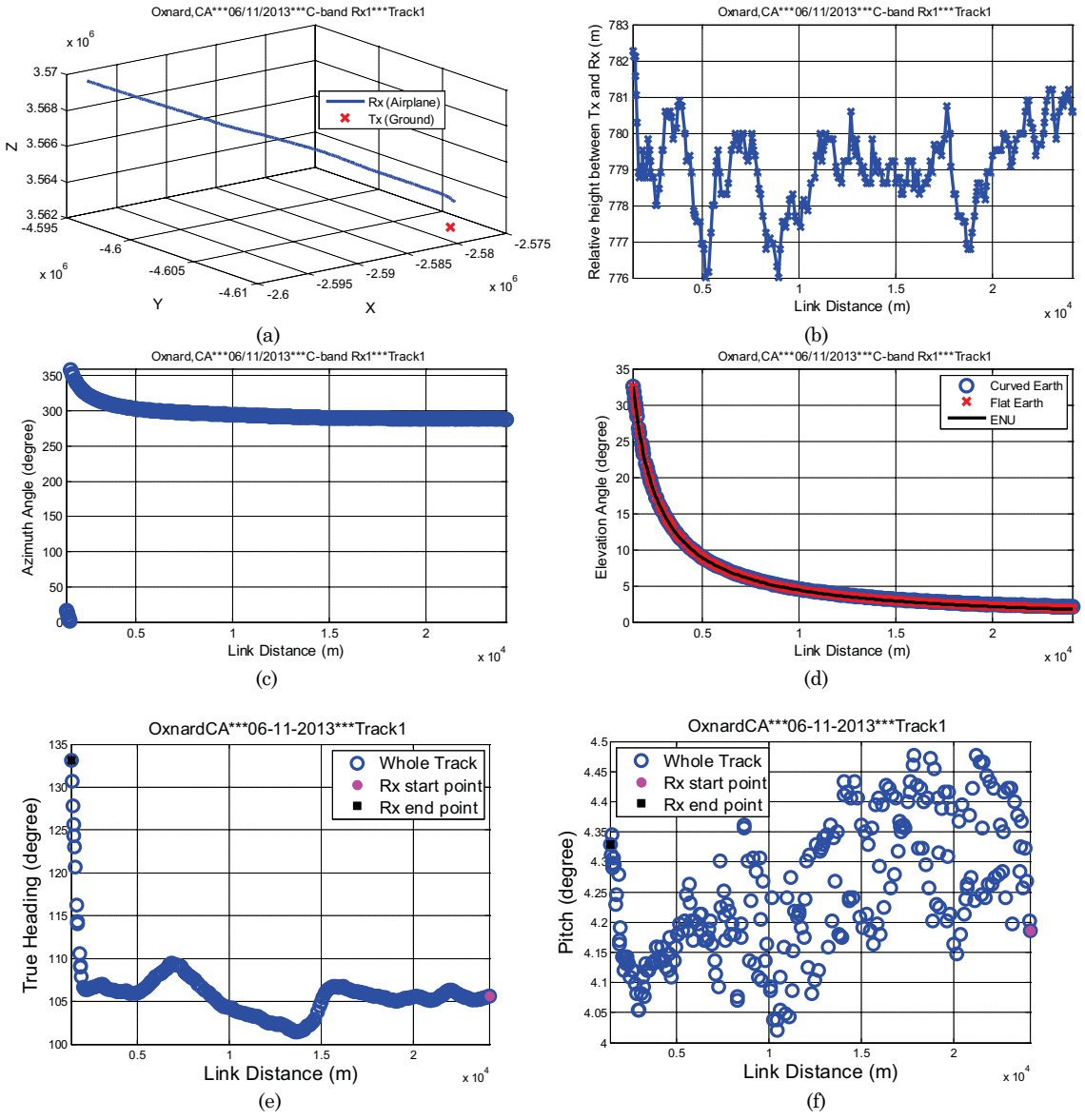

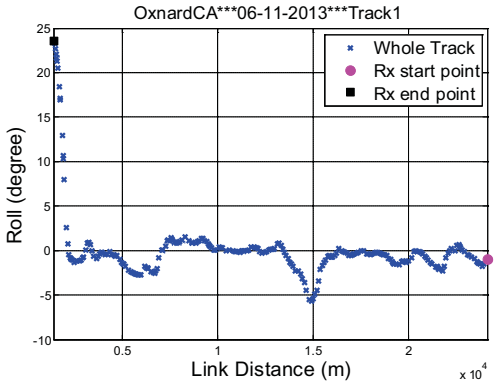

(g)

Figure 4. Geometric traces for flight track 1: (a) flight track in ECEF coordinates; (b) altitude difference between aircraft and ground station; (c) azimuth angle; (d) elevation angle; (e) AC heading; (f) AC pitch angle; (g) AC roll angle.

Although not directly used in initial data analysis, the AC attitude parameters (primarily pitch and roll angles) will be of use in diagnosing airframe shadowing effects. For example, at low elevation angles, even a pitch angle of 4 degrees may cause some shadowing by the aircraft tail. As seen in Figures 4 (f) and (g), the variation in roll and pitch were very small for this FT.

For this flight track, Figure 5 shows measured and analytical path loss vs. link distance, for C-band Rx1 and Rx2. The measured path loss is close to that of the free-space value, but slightly larger for short distances, and slightly less for large distances. Our current hypothesis for this discrepancy is the aircraft antenna—its gain varies with elevation angle. Depending upon aircraft attitude, some mild obstruction shadowing or reflections from the airframe may also occur at the short distances, reducing received power. Some of the "lobing" structure of the theoretical two-ray model can be seen in the measured data at the larger values of distance.

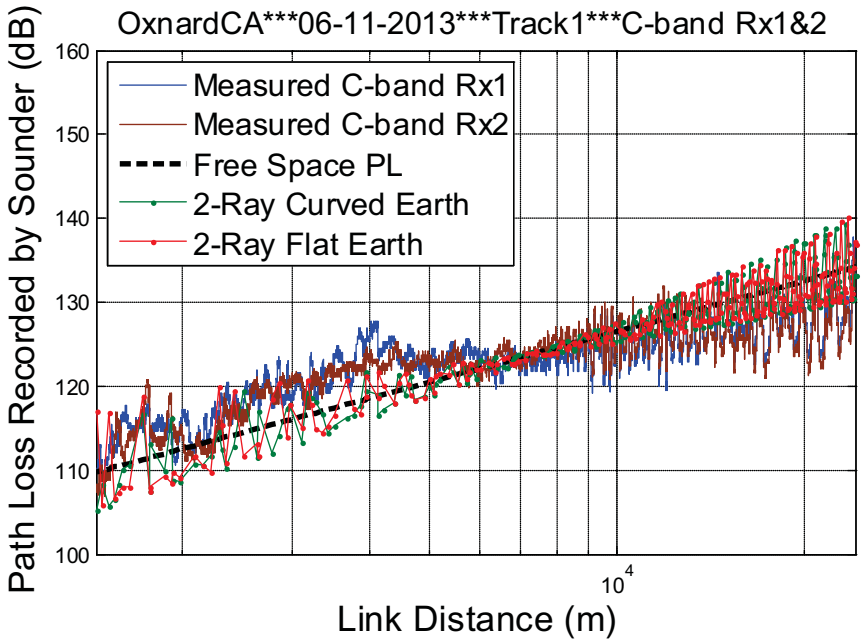

Figure 5. Measured results of C-band path loss vs. distance for Rx1 and Rx2, FT1.

The RMS-DS is the most common measure of the temporal dispersion of the channel; it is roughly the "spread" of the channel impulse response. For completeness we provide its formula here [5]; RMS-DS is denoted σ_τ, and is computed as follows:

$$\sigma_\tau = \sqrt{\frac{\sum_{k=0}^{L-1} \alpha_k^2 \tau_k^2}{\sum_{k=0}^{L-1} \alpha_k^2} - \mu_\tau^2}, \quad (1)$$

where α_k is the amplitude of the k^{th} MPC out of a total of L MPCs in the PDP, τ_k is the delay of the k^{th} MPC, and μ_τ is the mean energy delay, computed by the expression

$$\mu_\tau = \frac{\sum_{k=0}^{L-1} \alpha_k^2 \tau_k}{\sum_{k=0}^{L-1} \alpha_k^2}. \quad (2)$$

The denominator sum in both (1) and (2) is the total power in the PDP (either the average PDP for a given set of data, or for a single PDP—for the latter, (1) and (2) are termed the *instantaneous* RMS-DS and *instantaneous* mean energy delay).

Figure 6 shows RMS-DS vs. distance for FT1. In this figure, the RMS-DS is consistently larger than the single path value of approximately 10 ns only for the higher elevation angles at the shortest link distances. The RMS-DS is approximately 50-60 ns at the shortest link distances, and decreases to 10 ns as link distance exceeds ~2 km. This is as expected, since at larger link distances, the relative delay of the surface reflection decreases to below the C-band resolution of 20 ns. Several small "bumps" in the RMS-DS vs. distance plot are present, and these are indicative of likely reflecting objects on the sea-surface, or large ocean waves. We also include moving-average values of RMS-DS on the plots (averaging window length 1000) of RMD-DS vs. distance, as these can help distinguish actual changes in RMS-DS from isolated RMS-DS "spikes" due to noise.

In Figure 7 we plot RMS-DS vs. distance for a small section of FT1—the "bump" at approximately 2.27 km—which illustrates a short term increase in RMS-DS from approximately 10 to 50 ns, then a decrease back to 10 ns. This represents a segment of distance approximately 14 meters, and a time span of approximately 200 ms. The explanation for the increase in RMS-DS is shown in Figure 8, which plots a sequence of PDPs for the link distance range of Fig. 7. The LOS component is largest, with its power normalized to 0 dB, located at the 5th chip position. The sea-surface reflection at this link distance is at a relative delay of approximately 45 ns, approximately 2 chips from the LOS component. The MPCs indicated at approximately 22 chips from the LOS component (relative delay ~ 440 ns) produce the larger RMS-DS values in Fig. 7. The source of these MPCs is not known, but one hypothesis is a large ship in the ocean between the GS and AC; numerous boats and ships were indeed present in the vicinity during the flight tests. Another possibility is an offshore drilling platform. For either of these cases, with the aircraft velocity of near 90 m/s, a short-term reflection as in Figure 7 is indeed possible. Yet another possibility for the source of the reflection is an isolated large ocean wave.

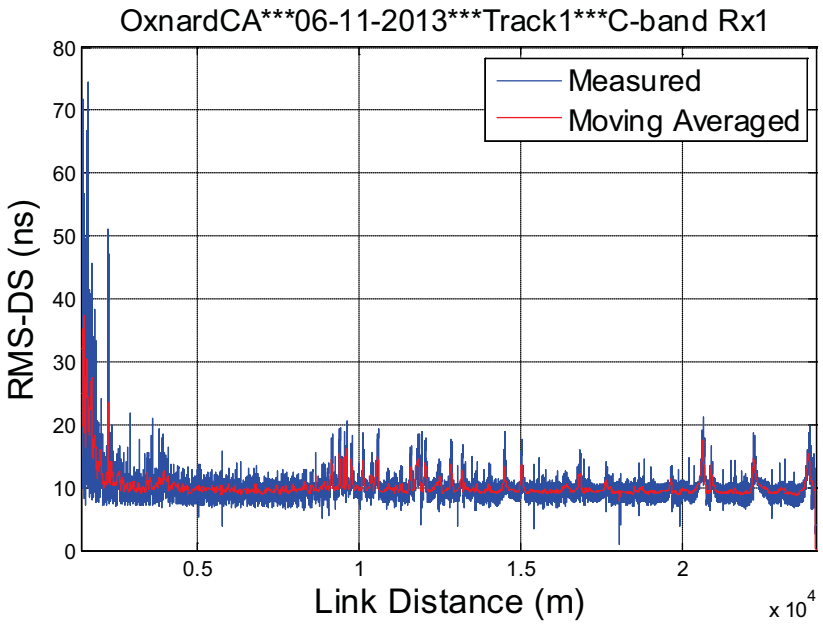

Figure 6. Measured C-band Rx1 RMS-DS vs. distance for entire FT1.

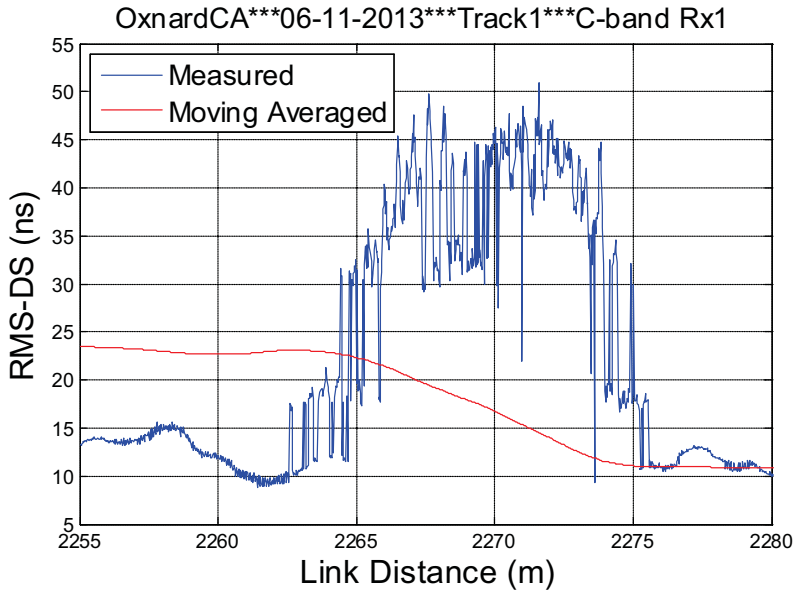

Figure 7. Measured C-band Rx1 RMS-DS vs. distance for small segment of FT1.

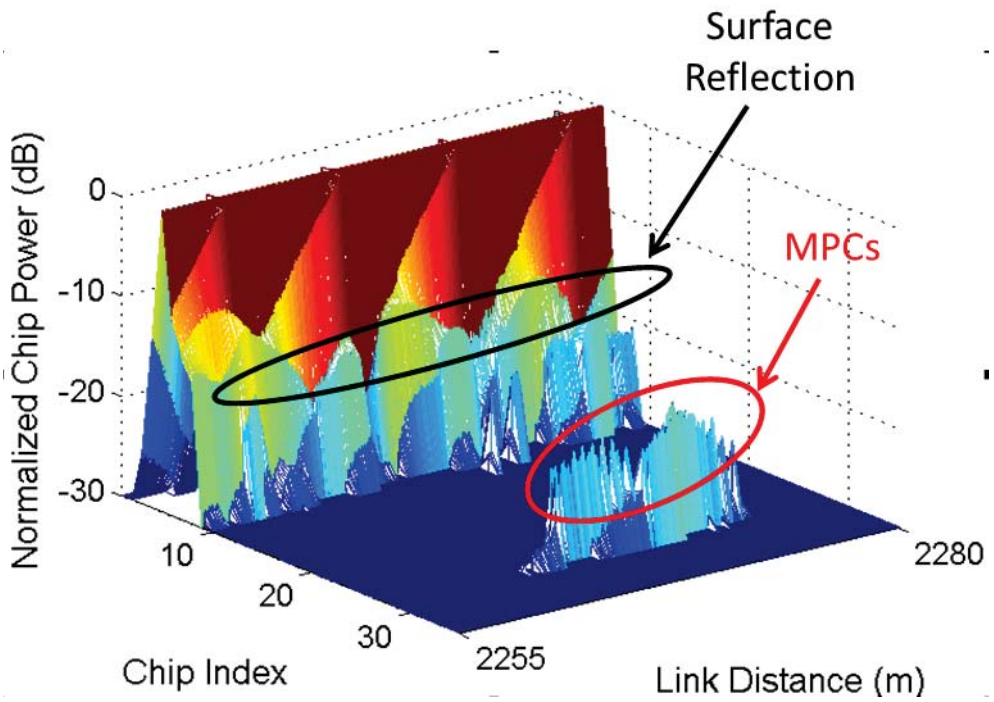

Figure 8. Sequence of PDPs for measured results of C-band Rx1, segment of FT1 of Fig. 7.

The RMS-DS for this receiver is mostly at the single-path value of approximately 10 ns, indicating that the sea surface reflection is unresolvable. For distances beyond a few km, geometric calculations easily confirm this. For some of the shortest-distance PDPs, when elevation angle is largest, RMS-DS values up to approximately 70 ns occur. Example PDPs for the sequence in Fig. 8 appear in Figure 9. Here the signal level is strong, and the second "cluster" of MPCs is 20-25 dB down from the LOS component, with relative delay of 5-10T_c~100-200 ns.

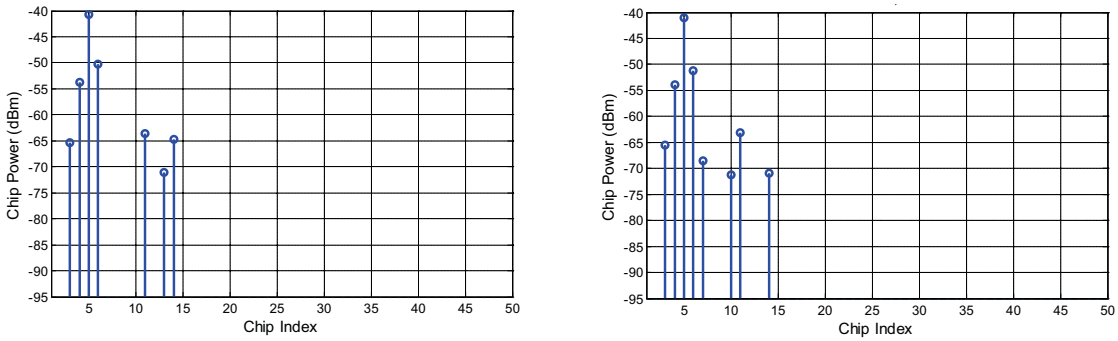

Figure 9. RMS-DS results for C-band Rx1, FT1, file 75 at small distance value (1.5 km) (a) PDP 4652; (b) PDP 4654.

Analysis of correlation coefficients is ongoing, since channel sounder variation and appropriate averaging times are still being analyzed. *Thus, all correlation coefficient results presented in this report are preliminary.* Plots in Figure 10 quantify the (spatial) correlation coefficient between the amplitudes of the received signals on the two C-band antennas. These antennas are separated by a physical distance of ~0.6 m. The amplitude correlation is computed by

$$\rho_{A_{C1},A_{C2}} = \frac{E\left[\left(A_{C1}-\mu_{A_{C1}}\right)\left(A_{C2}-\mu_{A_{C2}}\right)\right]}{\sigma_{A_{C1}}\sigma_{A_{C2}}} \quad (3)$$

where E denotes expectation, the A's in the numerator are sample vectors, and the μ's are the means of the A vectors. Specifically, $A_{C1} = (A_{C1,1}, A_{C1,2}, \ldots, A_{C1,i}, \ldots, A_{C1,n})$ is the vector of LOS amplitude samples for C-band Rx1; analogously, $A_{C2} = (A_{C2,1}, A_{C2,2}, \ldots, A_{C2,i}, \ldots, A_{C2,n})$ is the vector of Rx2 amplitude samples for its LOS component. The σ's are the standard deviations of the respective sample vectors. Element $A_{Ck,i}$ is the i^{th} amplitude sample (after time alignment, from the i^{th} PDP in a 1 ms delay bin) for Rxk, and vector length is n. We employed three different values of vector length n over which we compute the correlation: 500, 1000 and 5,000. Larger values of n provide correlation information between the two receivers for longer terms.

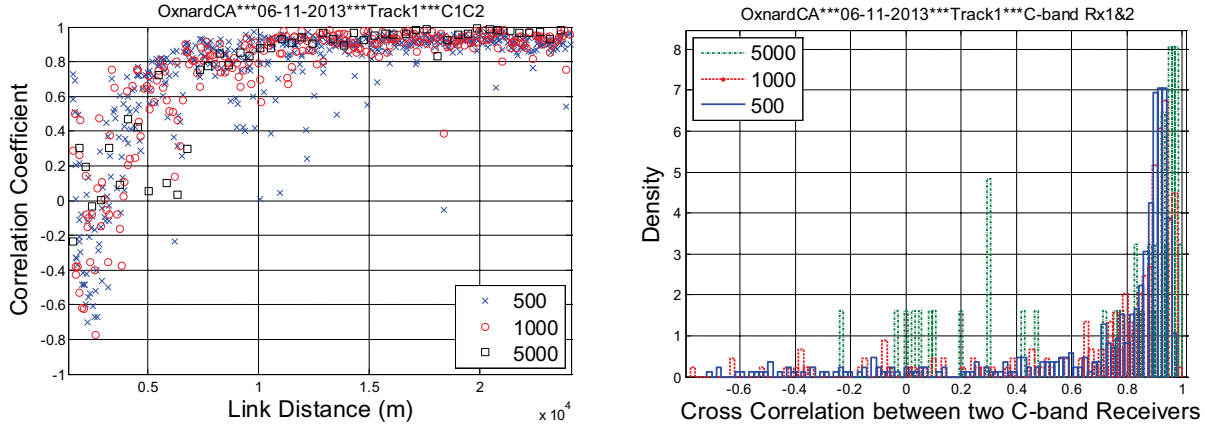

(a) (b)

Figure 10. Measured amplitude correlation coefficient between C-band Rx1 and 2 for FT1, for three different vector lengths: (a) correlation coefficient; (b) distributions of correlation coefficient.

In Fig. 10(a), the correlation ranges from approximately -0.8 to 0.8 for the shortest link distances, then increases to the value near 0.9 for link distances larger than approximately 5.3 km. The correlation for distances beyond 5.3 km is as expected: for these distances, the sea-surface reflection is unresolvable, and both receiver antennas maintain a constant orientation and relative distance to the GS. The path losses for the two receivers are also very similar. For the behavior at the shorter distances from ~1.45-5.3 km, we have observed from plots of the LOS component power that the trends in power for the two Rxs over this distance are opposing; this explains the behavior of the correlation for this short range, but at present we are still seeking an explanation for this unusual behavior of the LOS component powers; reflection by parts of the aircraft fuselage is one possibility. Figure 10(b) shows histograms of the correlation coefficients for the three different vector lengths. The statistics of the correlation coefficient for FT1 are listed in Table 1. The mean value of C-band spatial correlation is over 0.7, and that of L-band increases from 0.16 to 0.42 as the vector length n increases. The coefficient between receivers is denoted *FiGj* in Table 1, where *Fi* is *F*-band Rx*i* and *Gj* is *G*-band Rx*j*, with *F, G* either C or L, and *i,j* either 1 or 2.

Table 1. Statistics of Cross Correlation Coefficients for Oxnard, Flight Track 1 (straight path toward GS).

	C1C2			**L1L2**			**C1L1**	**C1L2**	**C2L1**	**C2L2**
Vector Length	500	1000	5000	500	1000	5000	1000	1000	1000	1000
Mean	0.72	0.72	0.72	0.16	0.22	0.42	-0.01	0.01	-0.01	0.02
Median	0.88	0.88	0.91	0.15	0.20	0.45	-0.02	0.01	-0.01	0.02
Max	0.98	0.98	0.99	0.73	0.77	0.87	0.68	0.80	0.63	0.66
Min	-0.70	-0.78	-0.24	-0.45	-0.53	-0.24	-0.76	-0.67	-0.55	-0.70
Standard deviation	0.36	0.37	0.36	0.19	0.18	0.23	0.22	0.20	0.19	0.20

We next look at the L-band results for FT1. As shown in Figure 11, the measured path loss for L-band receivers is also close to the free space path loss, and the two-ray lobes are more distinct than those at C-band for longer distances. This is because at L-band the sea is relatively smoother than at C-band, so the reflection is closer to specular, and also because the longer wavelength at L-band separates the peaks in the path loss by larger distances than at C-band.

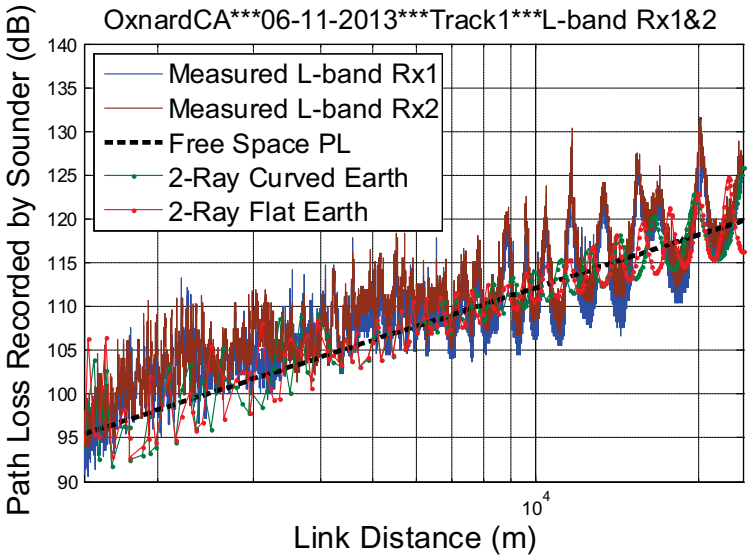

Figure 11. Measured path loss vs. distance results of L-band Rx1 & Rx2 for FT1.

The RMS-DS vs. link distance for L-band Rx1 shown in Figure 12 is between 40 ns and 140 ns, and this is essentially a single-path result (near what we obtain in back-to-back single-path tests—the variation is due to sample time offset and clock drift in the L-band transceivers). The surface reflection is always unresolvable since the L-band resolution is 200 ns. The "spikes" exceeding 150 ns in the RMS-DS vs. distance plot of Figure 12 are similarly due to internal sounder effects. These will be removed in future processing.

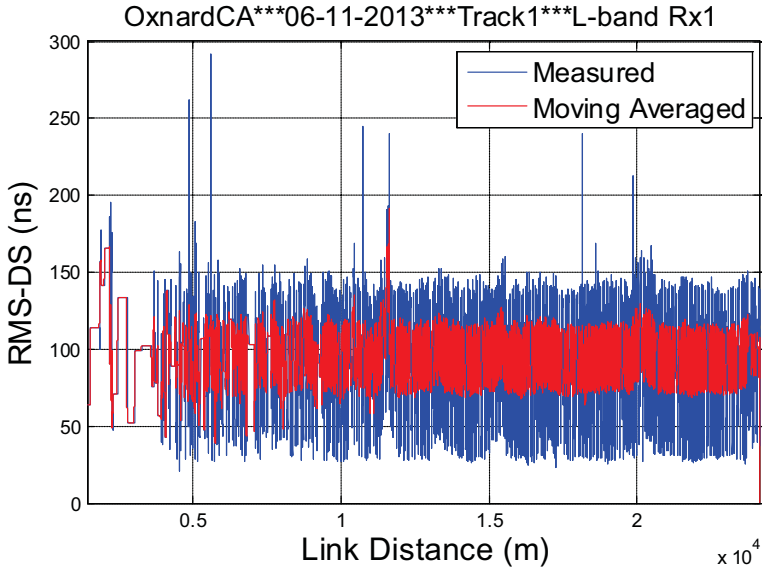

Figure 12. Measured RMS-DS vs. distance for L-band Rx1, FT1.

Analogous to the C-band results, Figure 13 shows the amplitude correlation coefficient vs. distance for the LOS components of the two L-band receivers. For short vector lengths (500), the amplitudes of the two received L-band LOS components are mostly uncorrelated, but the correlation generally increases as vector length increases. This can be explained via the two-ray model path loss plot in Figure 11: the trends for the two receiver components are more closely aligned when considered over larger distances, corresponding to longer vector lengths over which the correlation is computed. The smaller mean correlation values for the L-band are also likely due to the "noisier" L-band signal (this will be addressed in future analyses).

Additional correlation coefficient results between the LOS components of signals received at all combinations of antennas are provided in Table 1. The four antennas are located at the corners of a rectangle on the underside of the AC. Each band's two antennas are located at opposite corners of the rectangle, and the rectangle is approximately 0.4 m by 0.45 m. As can be seen from Table 1, LOS average amplitude correlations between bands are essentially zero; these inter-band LOS amplitude correlations are very near Gaussian in distribution.

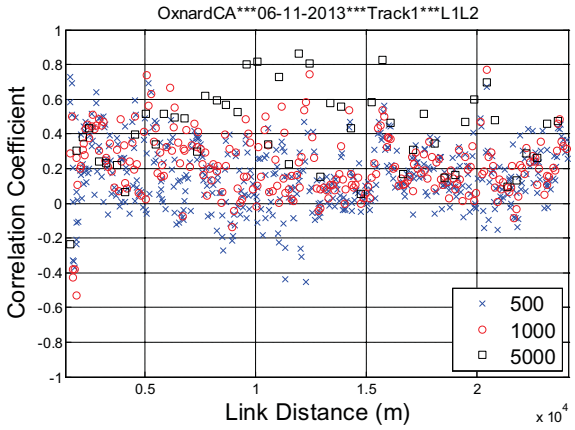

Figure 13. Measured amplitude correlation coefficient vs. distance between L-band Rx1 & 2 for FT1, three different vector lengths.

3.3 Flight Track 2

The next flight track we analyze is denoted FT2. Figure 14 shows the geometric traces for this flight track, in which the aircraft flew straight away from the GS. The total altitude variation was again approximately 8 m, and the azimuth angle was mostly near 280 degrees. The elevation angle behavior is similar to that of FT1, decreasing with distance. The link distances in FT2 are larger than those in FT1, reaching 45 km.

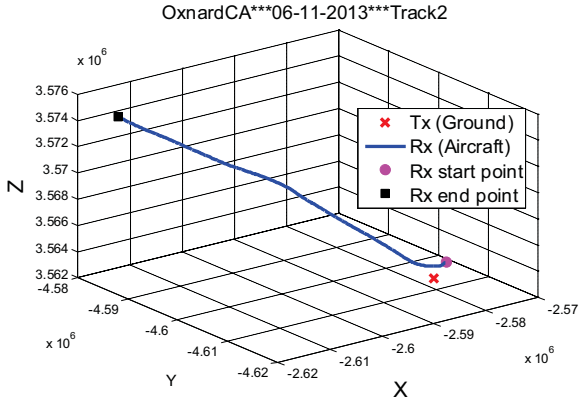

(a)

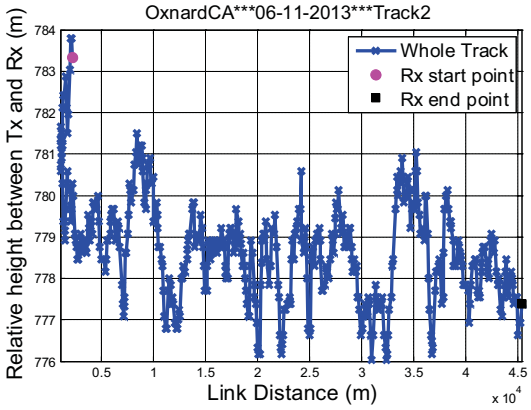

(b)

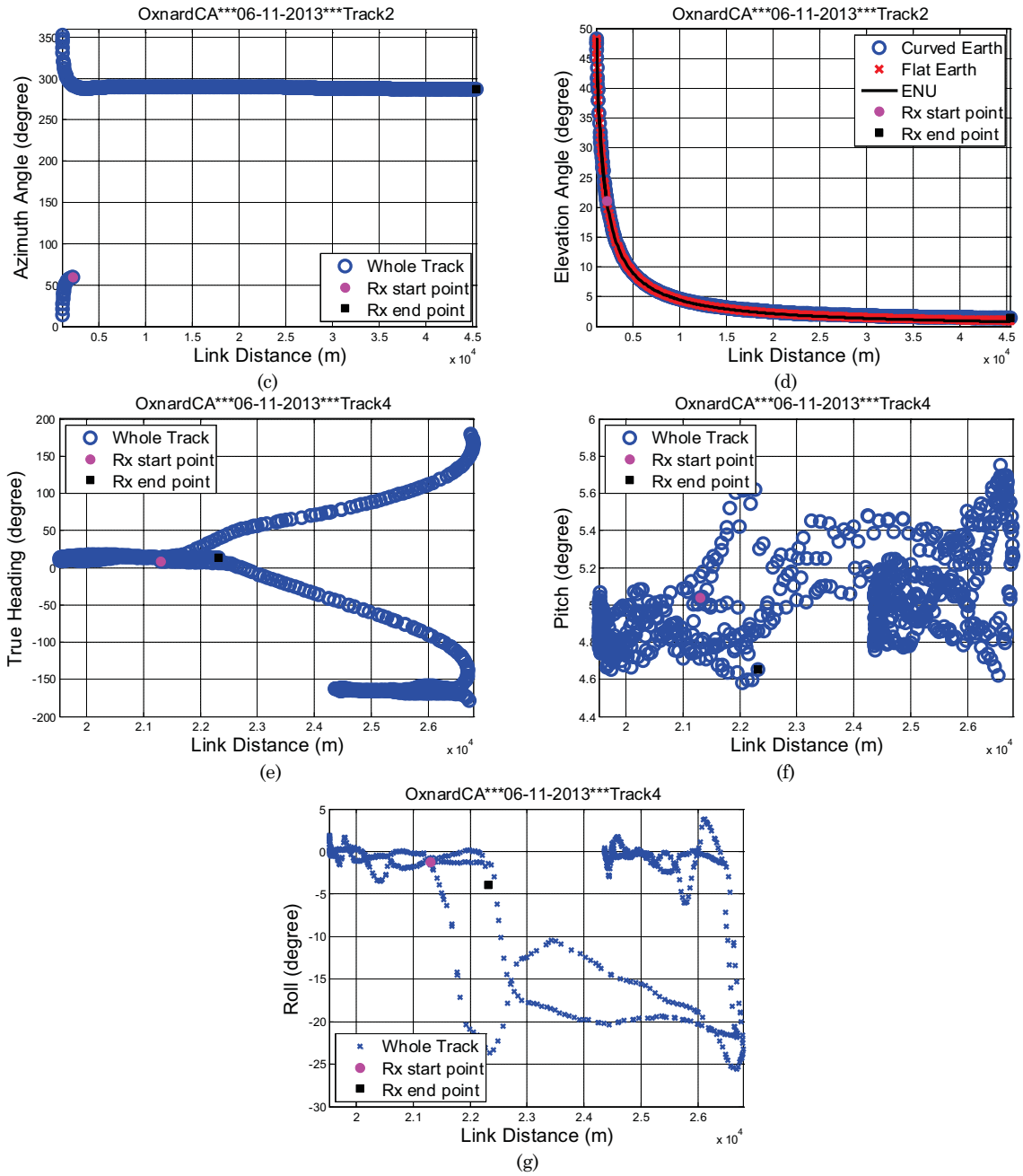

Figure 14. Geometric traces for FT4: (a) flight track in ECEF coordinates; (b) altitude difference between aircraft and ground station; (c) azimuth angle; (d) elevation angle; (e) AC heading; (f) AC pitch angle; (g) AC roll angle.

Figure 15 shows measured and analytical path loss vs. link distance for C-band Rx1 for FT2. The first three kilometers pertain to an "over-harbor" segment, which are discussed in a subsequent section of this report. The measured path loss for the over sea portion (> 3 km) is again close to that of the free-space value and two-ray values, and slightly less for large distances, again attributable to AC antenna effects.

Figure 16 shows RMS-DS vs. distance for FT2 for C-band Rx1. Most of the values beyond the 3 km link distance are near the single-path value of 10 ns, with a few "bumps" as in the FT1 results. Note also that some PDPs have an RMS-DS equal to zero. The zero values occur due to large path losses (cf. Fig. 15): in this condition all components in a PDP except for the single chip of the LOS component are attenuated below our noise removal threshold, and the single-chip RMS-DS is zero.

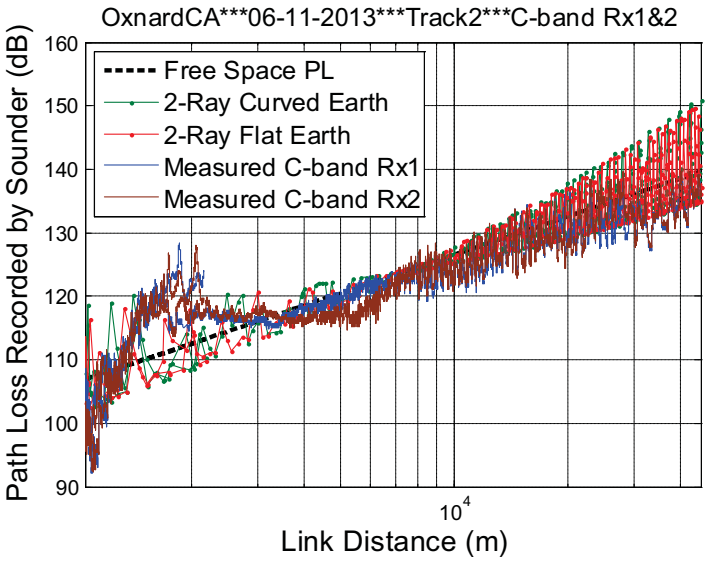

Figure 15. Measured path loss vs. distance for C-band Rx1 & 2, FT2.

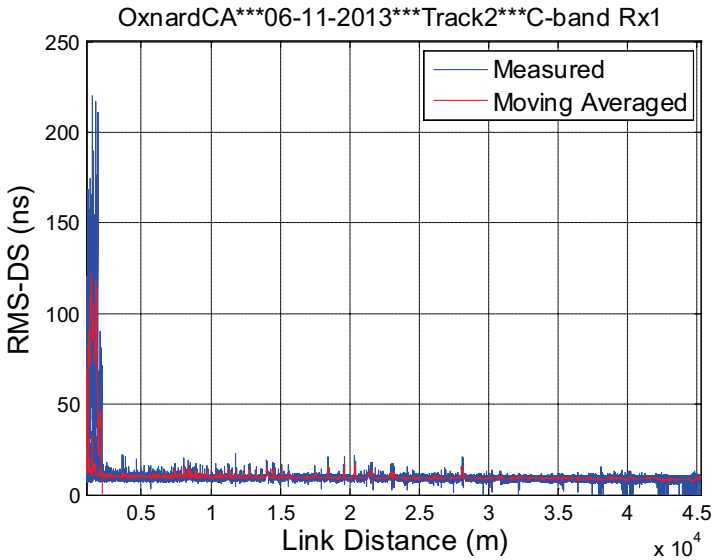

Figure 16. RMS-DS vs. distance for C-band Rx1, FT2.

The preliminary correlation coefficient results for the two C-band LOS component amplitudes for FT2 are shown in Figure 17. Here the correlations range from approximately -1 to 1, and the mean value increases from 0.52 to 0.85 as the vector length n increases. Note that at larger distance (beyond 25 km), the correlation for the shorter vector lengths tends to decrease. The histograms in Figure 17(b) illustrate the generally large positive correlations between the amplitudes for this straight FT.

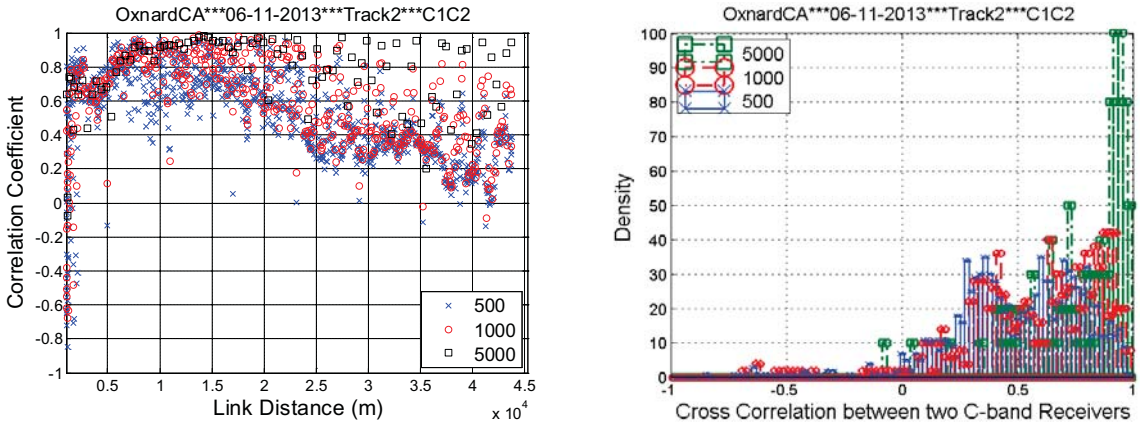

(a) (b)

Figure 17. Measured amplitude correlation coefficient between C-band Rx1 and 2 for FT2, for three different vector lengths: (a) correlation coefficient; (b) distributions of correlation coefficient.

The L-band path loss for FT2 appears in Figure 18. The path loss for the two receivers is nearly the same, and shows clear two-ray behavior. Figure 19 shows RMS-DS vs. distance for L-band Rx1 for FT2. As with the FT1 results, some isolated "spikes" above 200 ns are not attributable to actual MPCs, and these spikes will be removed in future processing.

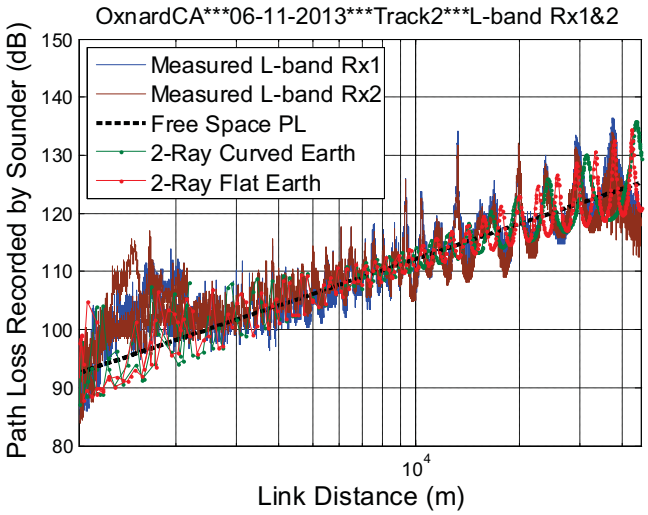

Figure 18. Path loss vs. distance for L-band Rx1 & 2 for FT2.

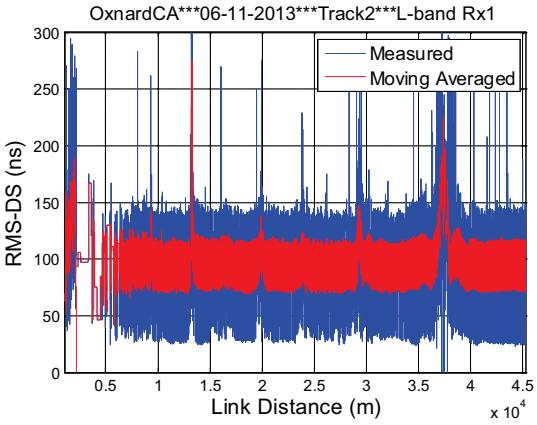

Figure 19. Measured RMS-DS vs. distance for L-band Rx1, FT2.

The preliminary correlation coefficient results for the two L-band receivers for FT2 appear in Figure 20. As with the C-band results, the correlation coefficient varies from near -0.8 to 1, and the mean value increases from 0.27 to 0.46 as the vector length n increases. These results are very similar to the results for FT1. The inter-band correlations for FT4 appear in Table 2. As with FT1, on average, the C-band and L-band LOS components are uncorrelated.

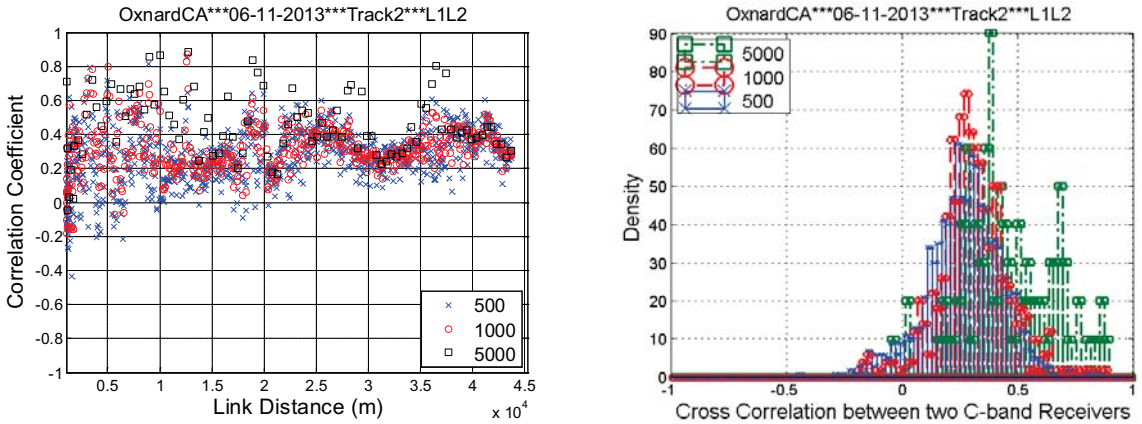

Figure 20. Measured amplitude correlation coefficient between L-band Rx1 and 2 for FT2, for three different vector lengths: (a) correlation coefficient; (b) distributions of correlation coefficient.

Table 2. Statistics of Cross Correlation Coefficients for Oxnard, Flight Track 2 (straight path away from GS).

	C1C2			L1L2			C1L1	C1L2	C2L1	C2L2
Vector Length	500	1000	5000	500	1000	5000	1000	1000	1000	1000
Mean	0.50	0.57	0.77	0.27	0.31	0.46	0.01	0.01	0.00	0.00
Median	0.52	0.63	0.85	0.28	0.30	0.43	0.00	0.01	0.00	0.00
Max	0.97	0.99	0.98	0.85	0.87	0.89	0.68	0.61	0.83	0.86
Min	-0.85	-0.68	-0.07	-0.44	-0.18	-0.05	-0.58	-0.78	-0.63	-0.60
Standard deviation	0.29	0.29	0.22	0.16	0.15	0.19	0.16	0.16	0.16	0.16

3.4 Flight Track 4

The next flight track we analyze is denoted FT4. Figure 21 shows the geometric traces for this flight track, in which the aircraft flew in an oval-shaped pattern with the major axis of the oval perpendicular to the direct line from the GS to the aircraft. The total altitude variation was again approximately 6 m, and the azimuth angle ranged from approximately 250-320 degrees, whereas the elevation angle was below 2.5 degrees. As can be seen from parts (e)-(g) of Figure 21, the heading, pitch angle, and roll angle generally vary over larger ranges than in the straight flight paths of FT1 and FT2.

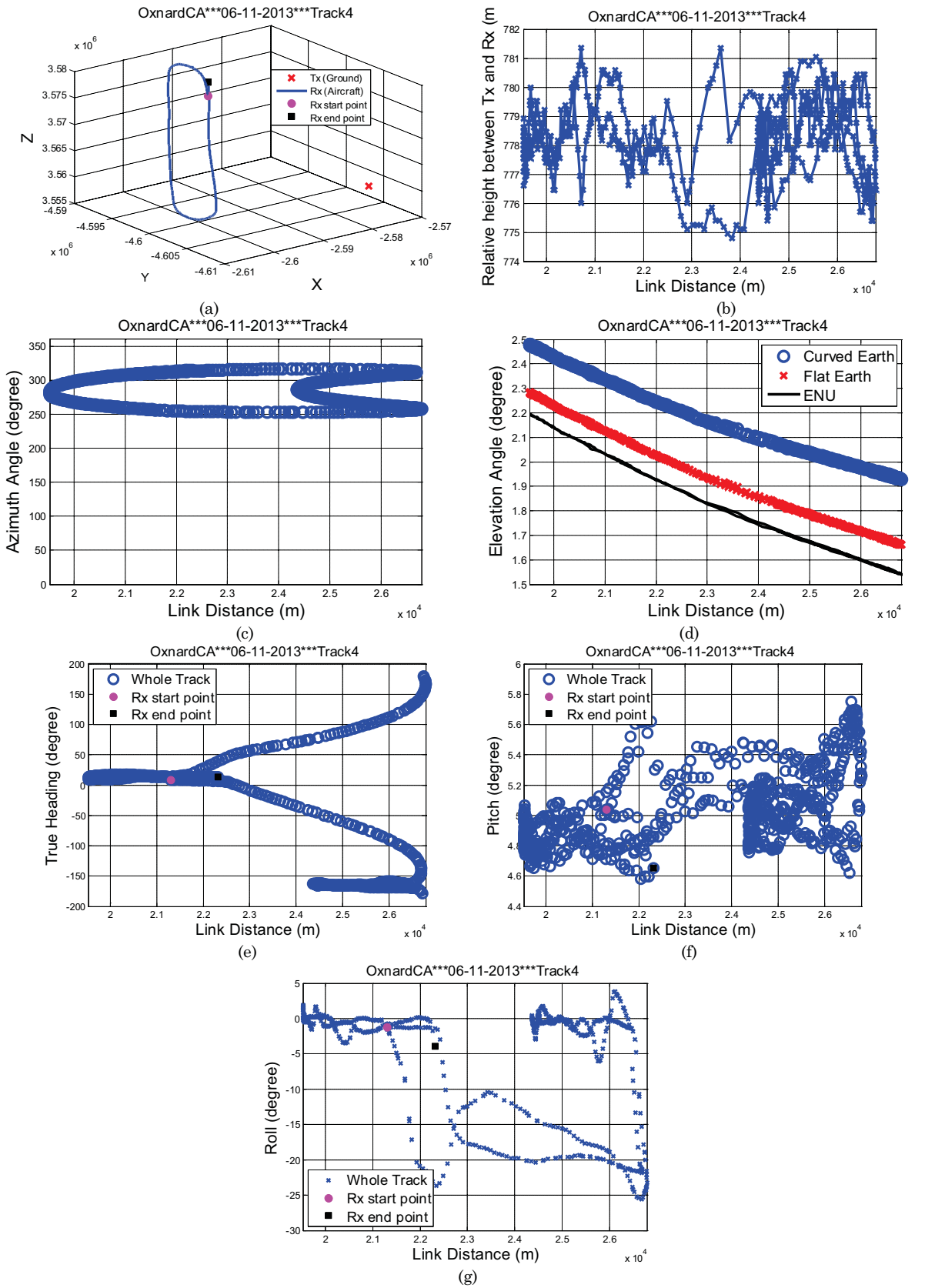

Figure 21. Geometric traces for FT4: (a) flight track in ECEF coordinates; (b) altitude difference between aircraft and ground station; (c) azimuth angle; (d) elevation angle; (e) AC heading; (f) AC pitch angle; (g) AC roll angle.

For FT4, Figure 22(a) shows measured and analytical path loss vs. link distance for C-band Rx1. The measured path loss is again close to that of the free-space value and two-ray values; as with the straight flight tracks, it is slightly more than free space for the shortest and largest distances, and slightly less for medium distances. The AC was making a "U-turn" at the oval path edges at link distances from ~22.5 to 26.8 km with a roll angle between -10 and -25 degrees. The large broad "dip" in the middle of the path loss vs. distance plot (22.5 - 24.2 km) is attributable to a slightly larger value of Rx antenna gain at these values of roll angle. In Figure 22(b) we illustrate the effects of sea-surface roughness on the analytical (curved-earth, two-ray) models. This effect is incorporated as a modification of the surface reflection coefficient magnitude, in which with a surface elevation modeled as Gaussian with standard deviation σ_h, the smooth surface reflection coefficient magnitude $|\Gamma_0|$ is replaced with the following [11]:

$$|\Gamma| = |\Gamma_0| exp[-2(2\pi g)^2] I_0[-2(2\pi g)^2] \quad (4)$$

where I_0 is the modified Bessel function of the first kind, order zero, and g is given by

$$g = \sigma_h sin(\psi)/\lambda \quad (5)$$

with ψ the grazing angle and λ wavelength. As expected, this modification only alters the two-ray resultant amplitude, and not its shape. For results in Figure 22(b), for σ_h we use the formula in [11] $\sigma_h = 0.0051u^2$, with u=wind speed in m/s.

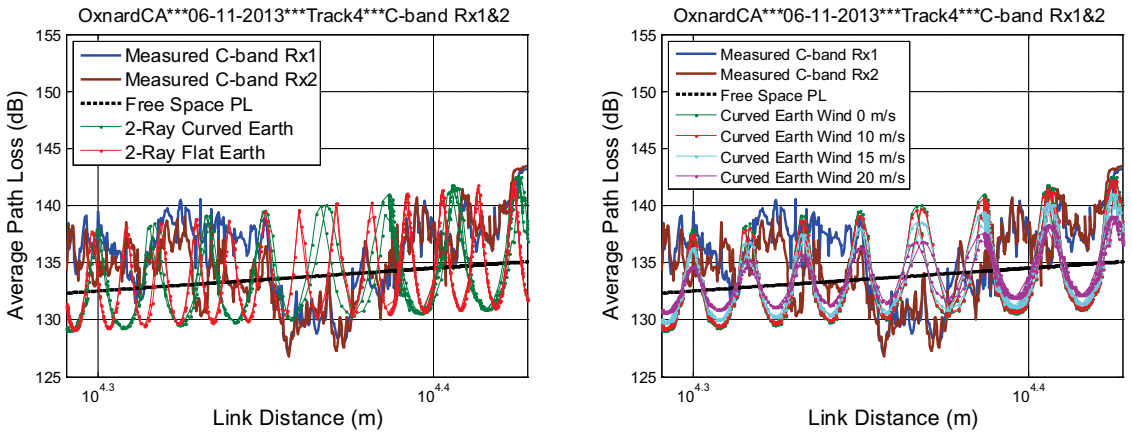

Figure 22. (a) Measured path loss vs. distance for C-band Rx1 & 2, FT4; (b) measured and analytical (curved-earth, two-ray) path loss showing effects of surface roughness.

Figure 23 shows RMS-DS vs. distance for FT4 for C-band Rx1. Most of the values are again, as expected, near the single-path value of 10 ns, with a few "bumps" as in the FT1 results. Note also that some PDPs have an RMS-DS equal to zero, explained by the large path loss values in Figure 22. A plot of RMS-DS for a short segment of FT4 is shown in Figure 24. Similar to the FT1 result, this short-term rise in RMS-DS is likely due to a reflection from a surface object or large ocean wave. Figure 25 shows the sequence of PDPs for the Figure 24 segment. Here the relative delay of the MPC is 10 chips or ~ 200 ns, even larger than that in FT1.

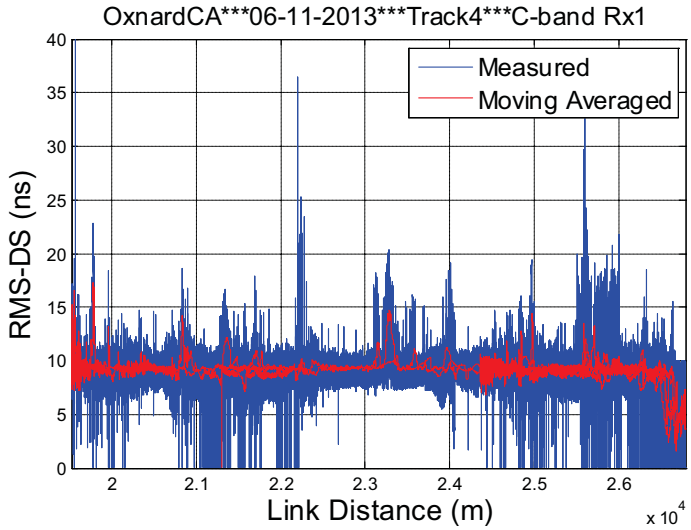

Figure 23. RMS-DS vs. distance for C-band Rx1, FT4.

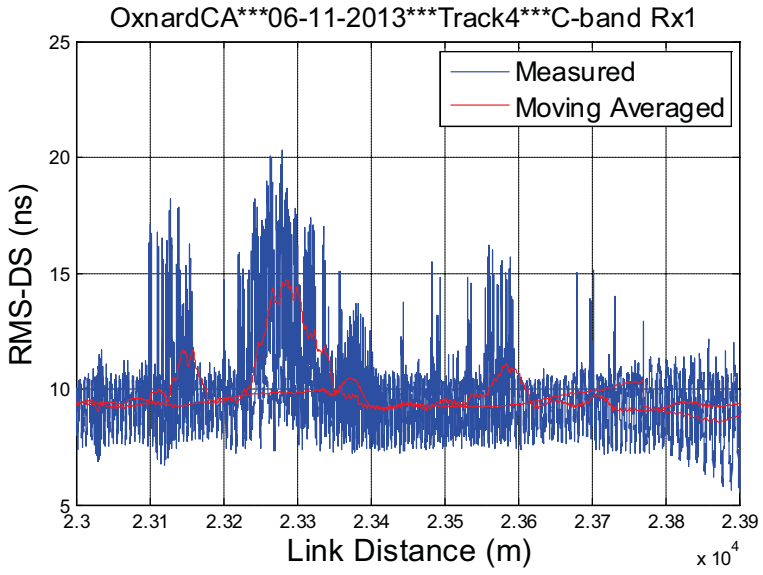

Figure 24. Measured C-band Rx 1 RMS-DS for small segment of FT4.

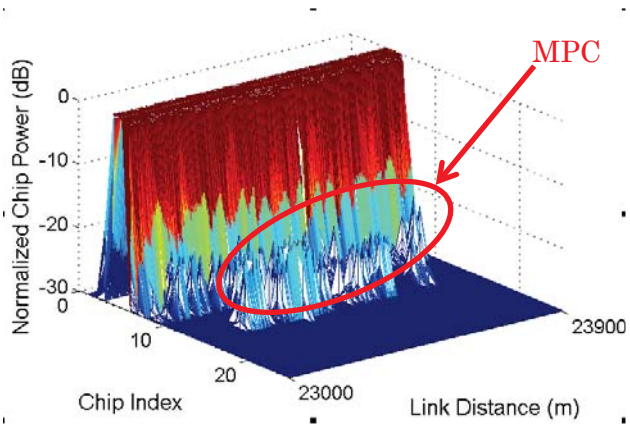

Figure 25. Sequence of PDPs for measured results of C-band Rx1, segment of FT4 of Fig. 24.

The initial correlation coefficient results for the two C-band LOS component amplitudes for FT4 are shown in Figure 26. Here the correlations range from approximately -0.9 to 1, and the mean value increases from 0.2 to 0.6 as the vector length *n* increases. In the oval shaped path of FT4, the relative separation of the C-band antennas changes as the AC orientation changes, and this will affect correlation. The averages correlation between the signals on the two C-band antennas is much smaller in the oval-shaped path than in the straight paths of FT1 and FT2.

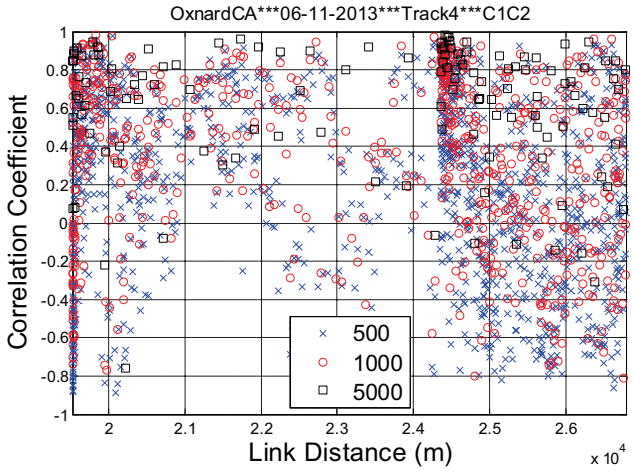

Figure 26. Measured amplitude correlation coefficient between C-band Rx1 and 2 for FT4, for three different vector lengths.

The L-band path loss for FT4 appears in Figure 27(a). The path loss for the two receivers is nearly the same, and again evinces the clear two-ray behavior, in reasonable agreement with the curved-earth analytical result. We also show the effects of surface roughness in Figure 27(b), analogous to the C-band results; at L-band, since the wavelength is larger, the roughness effect is less significant. Figure 28 shows RMS-DS vs. distance for L-band Rx1 for FT4. As with the FT1 results, the "spikes" above 200 ns are not attributable to actual MPCs, and these spikes will be removed in future processing.

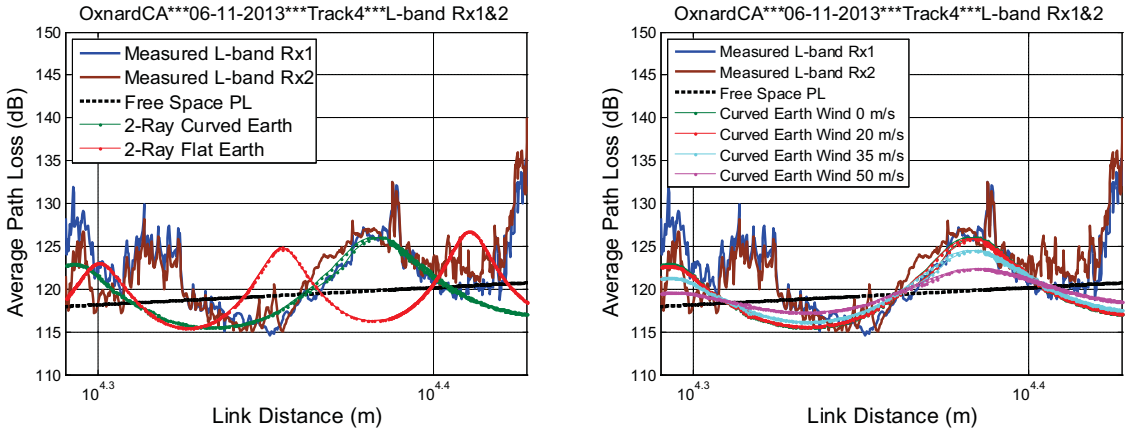

(a) (b)

Figure 27. (a) Path loss vs. distance for L-band Rx1 & 2 for FT4; (b) measured and analytical (curved-earth, two-ray) path loss showing effects of surface roughness.

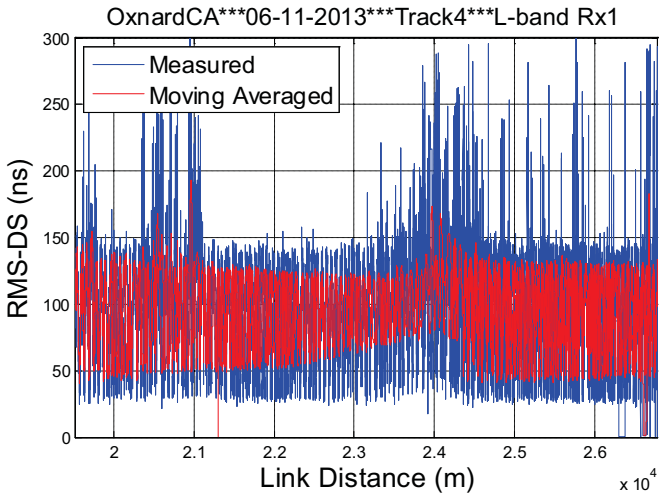

Figure 28. Measured RMS-DS vs. distance for L-band Rx1, FT4.

The preliminary correlation coefficient results for the two L-band receivers appear in Figure 29. Similar to the C-band results, the correlation coefficient varies from near -0.9 to 1, and the mean value increases from 0.14 to 0.46 as the vector length n increases. These L-band results are quite similar to the results for FT1. The inter-band correlations for FT4 appear in Table 3. As with FT1 and FT2, on average, the C-band and L-band LOS components are uncorrelated.

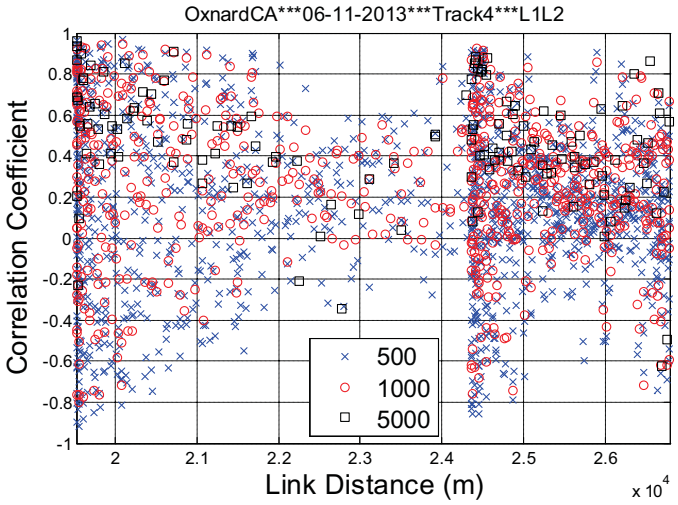

Figure 29. Measured amplitude correlation coefficient between L-band Rx1 and 2 for FT4, for three different vector lengths.

Table 3. Statistics of Cross Correlation Coefficients for Oxnard, Flight Track 4 (oval-shaped path).

	C1C2			L1L2			C1L1	C1L2	C2L1	C2L2
Vector Length	500	1000	5000	500	1000	5000	1000	1000	1000	1000
Mean	0.20	0.34	0.60	0.14	0.25	0.46	-0.02	0.00	0.00	-0.01
Median	0.26	0.42	0.70	0.15	0.28	0.47	-0.01	0.00	-0.01	0.00
Max	0.98	0.98	0.98	0.96	0.94	0.96	0.71	0.81	0.79	0.81
Min	-0.89	-0.81	-0.76	-0.92	-0.80	-0.63	-0.72	-0.72	-0.74	-0.67
Standard deviation	0.48	0.44	0.34	0.41	0.36	0.28	0.26	0.27	0.27	0.26

3.5 Flight Track 10

The next flight track we analyze is FT10. Figure 30 shows the geometric traces for this flight track, in which the aircraft flew mostly straight toward the GS, from link distances 18-45 km. The total altitude variation was again approximately 6 m, and the azimuth angle was approximately 280 degrees, whereas the elevation angle was below 2.5 degrees. Note again the fairly large range of AC roll angle values, from approximately -25 degrees to 25 degrees.

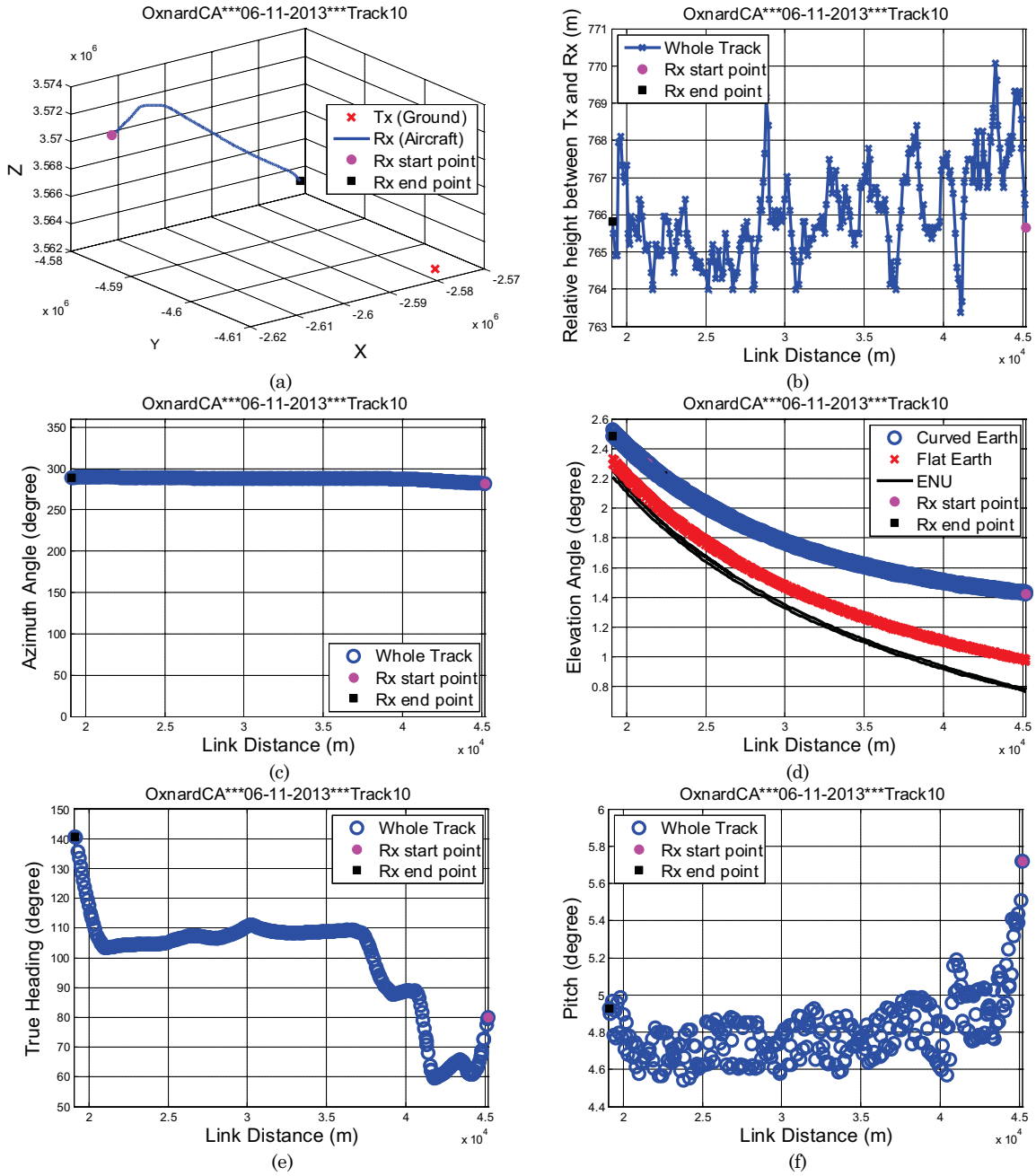

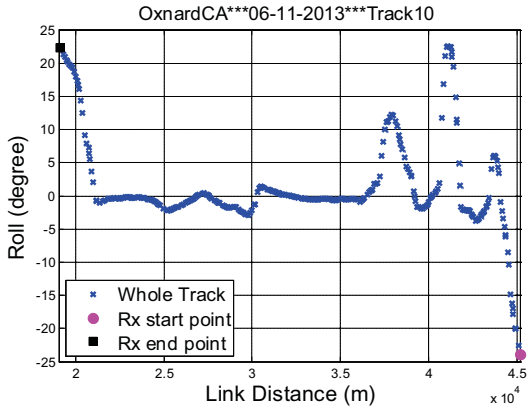

(g)

Figure 30. Geometric traces for FT4: (a) flight track in ECEF coordinates; (b) altitude difference between aircraft and ground station; (c) azimuth angle; (d) elevation angle; (e) AC heading; (f) AC pitch angle; (g) AC roll angle.

For FT10, Figure 31 shows measured and analytical path loss vs. link distance for C-band Rx1. The measured path loss is once again close to that of the free-space value and two-ray values.

Figure 32 shows RMS-DS vs. distance for FT10 for C-band Rx1. Most of the delay spreads lie near the single-path 10 ns value (with some zero values as well when path loss is large). We also note again several "bumps" in the RMS-DS vs. distance plots as in prior results.

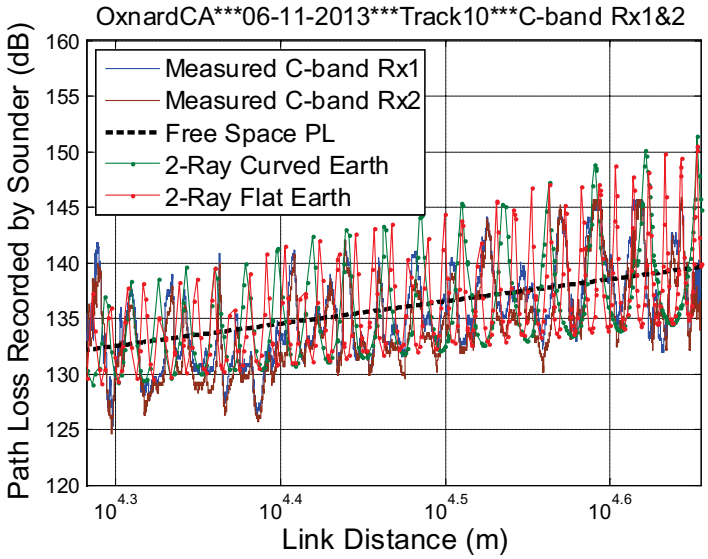

Figure 31. Measured path loss vs. distance for C-band Rx1 & 2, FT10.

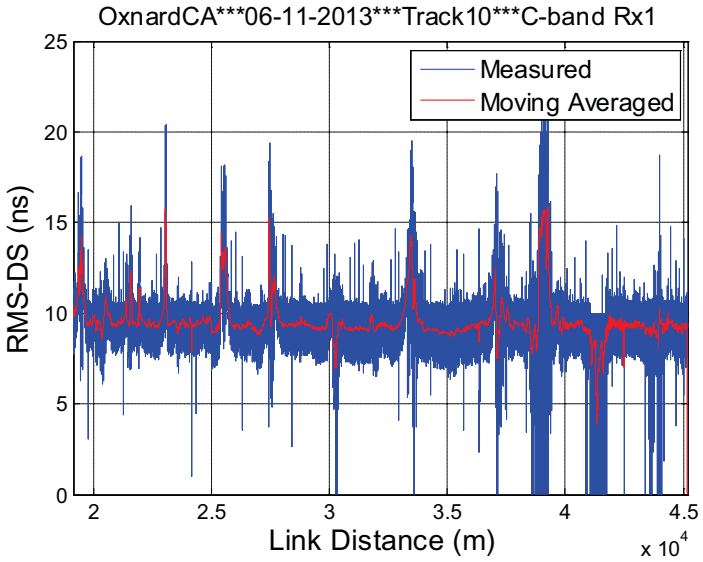

Figure 32. RMS-DS vs. distance for C-band Rx1, FT10.

The initial correlation coefficient results for the two C-band LOS component amplitudes are shown in Figure 33. Here the correlations range from approximately -0.8 to 0.9, and the mean value increases from 0.04 to 0.68 as the vector length *n* increases. Average correlations are smaller than in FT1 and FT2, but not as small as in the oval-shaped FT4.

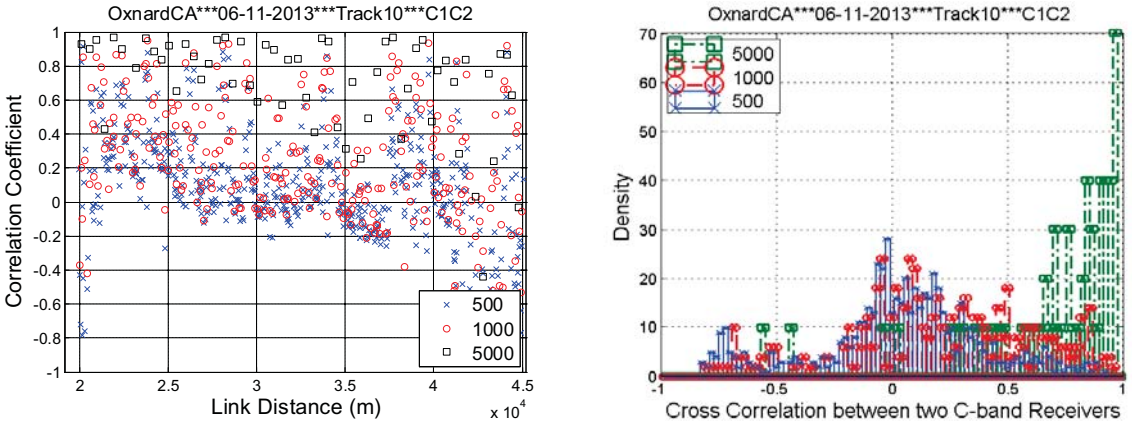

Figure 33. Measured amplitude correlation coefficient between C-band Rx1 and 2 for FT10, for three different vector lengths: (a) correlation coefficient; (b) distributions of correlation coefficient.

The L-band path loss for FT10 appears in Figure 34. Once again, the path loss for the two L-band receivers is nearly identical, exhibiting the expected two-ray behavior. Figure 35 shows RMS-DS vs. distance for L-band Rx1 for FT10. As with the FT1 results, some isolated "spikes" above 200 ns—not attributable to actual MPCs—exist; these spikes will be removed in subsequent processing.

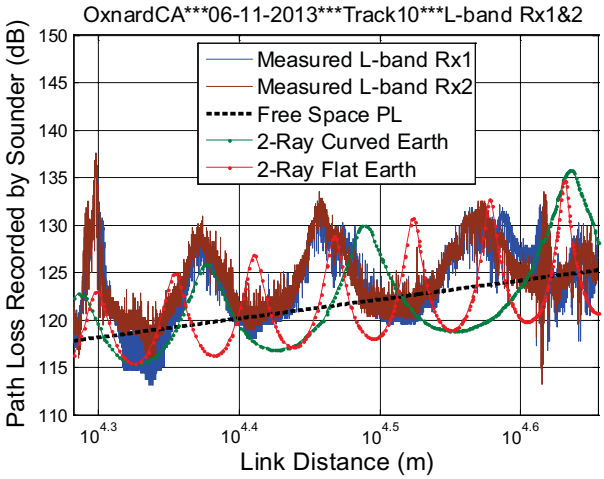

Figure 34. Path loss vs. distance for L-band Rx1 & 2 for FT10.

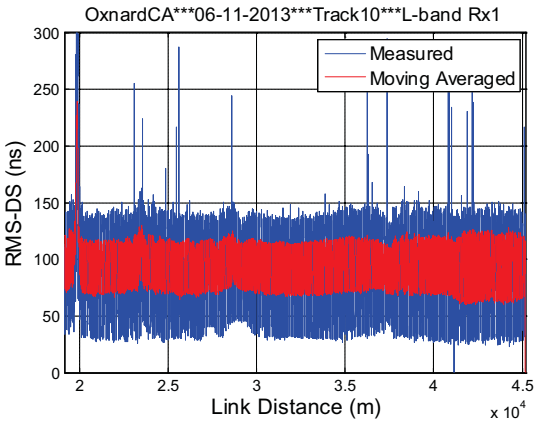

Figure 35. Measured RMS-DS vs. distance for L-band Rx1, FT10.

The preliminary correlation coefficient results for the two L-band receivers appear in Figure 36. Similar to the C-band results, the correlation coefficient varies from near -0.3 to 0.8, and the mean value increases from 0.21 to 0.31 as the vector length n increases. These results are very similar to the results for FT1. The inter-band correlations for FT4 appear in Table 4. As with FT1, on average, the C-band and L-band LOS components are uncorrelated.

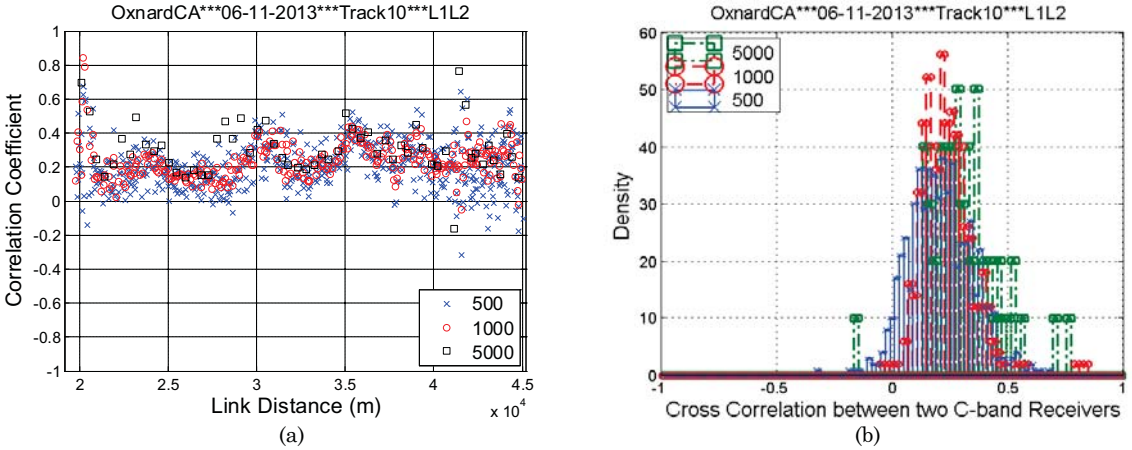

Figure 36. Measured amplitude correlation coefficient between L-band Rx1 and 2 for FT10, for three different vector lengths: (a) correlation coefficient; (b) distributions of correlation coefficient.

Table 4. Statistics of Cross Correlation Coefficients for Oxnard, Flight Track 10 (straight path toward GS).

	C1C2			L1L2			C1L1	C1L2	C2L1	C2L2
Vector Length	500	1000	5000	500	1000	5000	1000	1000	1000	1000
Mean	0.04	0.20	0.68	0.21	0.24	0.31	0.01	0.01	-0.01	-0.01
Median	0.06	0.19	0.81	0.21	0.22	0.28	0.01	0.02	0.00	0.00
Max	0.92	0.95	0.97	0.68	0.84	0.76	0.50	0.60	0.60	0.63
Min	-0.83	-0.80	-0.57	-0.32	-0.05	-0.16	-0.69	-0.76	-0.71	-0.72
Standard deviation	0.36	0.39	0.33	0.14	0.11	0.15	0.15	0.16	0.16	0.15

3.6 Over-Harbor Results

These results are from one specific portion of FT2, in which we observed some interesting results. Figure 37 shows a closer view of this portion of FT2. The GS near the shore has its transmitters denoted "Tx" in the figure. The aircraft flight path is shown as the two line segments (red and orange) with arrows, where the plane moves approximately southwest and then west. We provide analysis for two files in this FT, denoted file 1 and file 2. Note that for the entire red-segment portion of this flight, the aircraft was *not* in the main beam of the GS antenna, and hence antenna backlobe effects pertain. Nonetheless, since the link distance is short, received power is more than sufficient to collect valid data. In addition, despite the complicating effect of antenna backlobes, the results we observed are interesting and practically important, as they illustrate pertinent AG channel features that will arise in actual UAS operation. Since we have the pattern data for the GS antennas, we account for this effect.

Figure 38 shows the aircraft trajectory in ECEF coordinates, computed using the aircraft GPS data. Such trajectories of course allow us to compute link distances and to conduct our geometric analysis for the deterministic portion of the CIR, which consists of the LOS path (if it exists) and the single primary surface reflection. These LOS and surface-reflection components are largely predictable, although due to link considerations such as antenna pattern effects, prediction accuracy is limited. (This limited accuracy of the analysis is fully expected, and is part of the underlying motivation for measurements; measurements are also essential for the stochastic components of the CIR, the additional MPCs.) Figure 39 shows the elevation angle from Tx to Rx vs. distance. Note that for these relatively short link distances of a few km, the flat-earth approximation is sufficient as its elevation angle is essentially identical to the angle predicted by the complex computations used in the more accurate curved earth case.

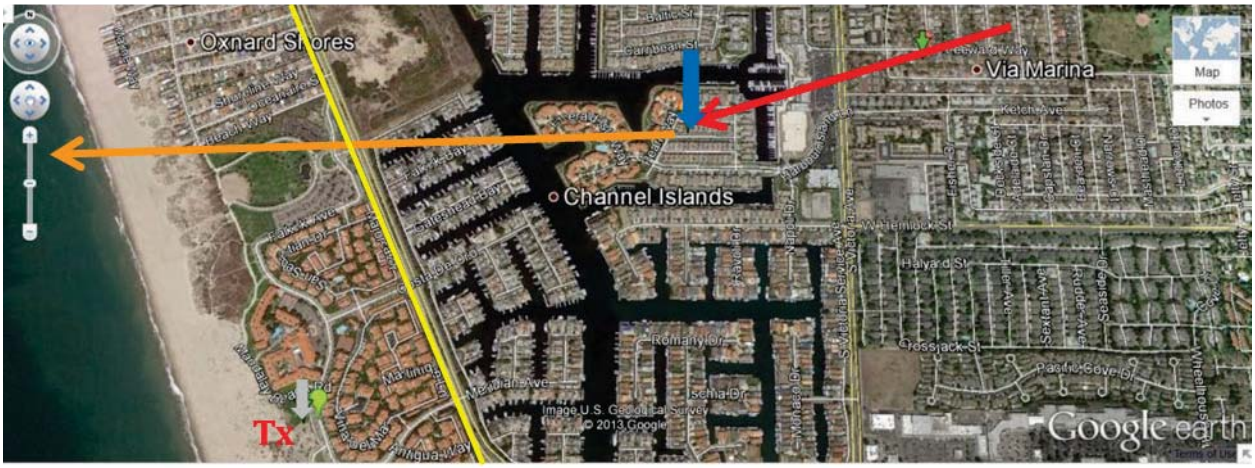

Figure 37. Portion of FT2 with ground site at Oxnard, 11 June 2013.

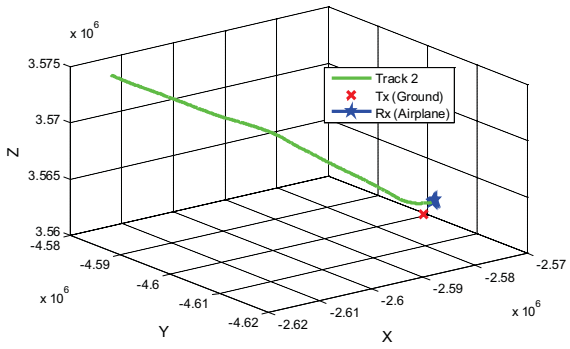

Figure 38. ECEF coordinates for portion of FT2, file 1, with ground site at Oxnard, 11 June 2013.

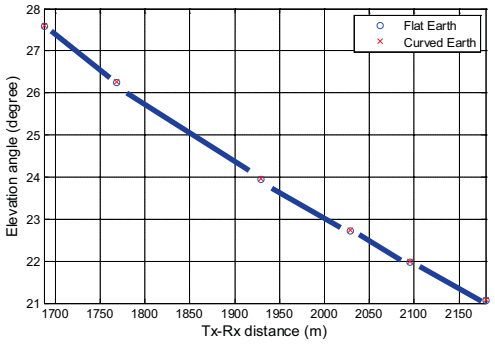

Figure 39. Elevation angle vs. link distance for portion of FT2, file 1, with ground site at Oxnard, 11 June 2013.

In Figure 40 we show C-band Rx1 path loss for both files 1 and 2 of FT2. This is plotted for both file 1 (left) and file 2 (right) vs. the PDP index, which as noted, is a count that identifies PDPs within each file. This index is roughly proportional to time and distance (i.e., the abscissa in the left plot in Fig. 40 roughly corresponds to the abscissa in Fig. 39).

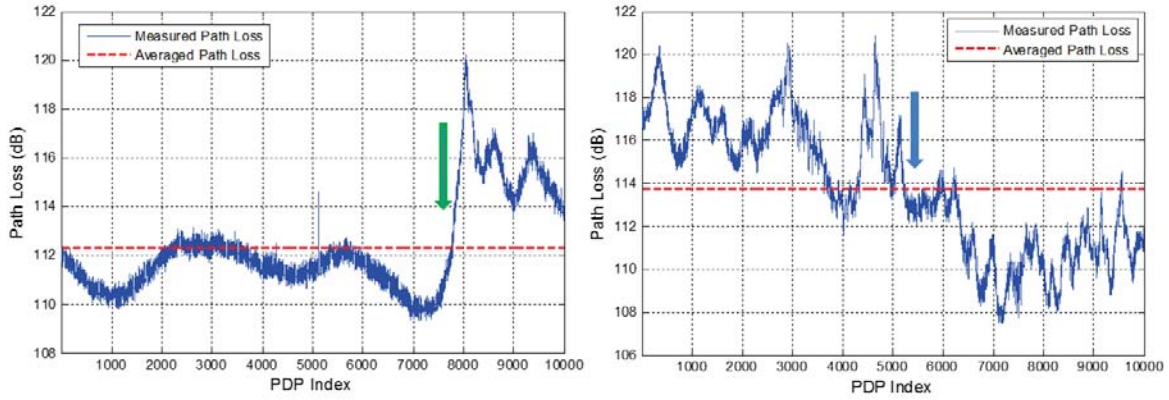

Figure 40. C-band Rx1 path loss vs. PDP index (~link distance) for portion of FT2, file 1 (left) and file 2 (right), with ground site at Oxnard, 11 June 2013.

Based on the GS antenna gain information provided by the manufacturer, using an elevation angle of 25 degrees and azimuth angle opposite to the maximum gain direction, the Tx antenna backlobe gain is ~-10 dB for C-band and ~-7 dB for L-band. The measured path loss agrees with the link budget (analytical path loss) nearly perfectly if these backlobe Tx gains are applied. Considering next the path loss *variation*, note that path loss increases by approximately 3-7 dB at PDP index values from ~7500 in file 1 to index value ~6000 in file 2. This time duration is approximately 6 seconds. During this period, we also observed several strong MPCs (~12 dB smaller than the LOS component) in many of the PDPs. The excess delay of these strong MPCs is within approximately 50 chips of the LOS component. This corresponds to $50T_c$ = 50×20 ns = 1 microsecond, or MPC delays of approximately 300 m relative to the LOS component.

Figure 41 shows computed RMS-DS vs. PDP index for the C-band measured data corresponding to Figure 40. Large RMS-DS values (above ~ 150 ns) are evident during the same time period as the path loss increase. Note again that this portion of flight corresponds to the red segment line in Figure 37. During this period, the aircraft moved from the upper right in Figure 37 (the small green arrow is the approximate starting point of the large path loss values) to the blue arrow toward the "Channel Islands" marker (this is the ending point of the large path loss values).

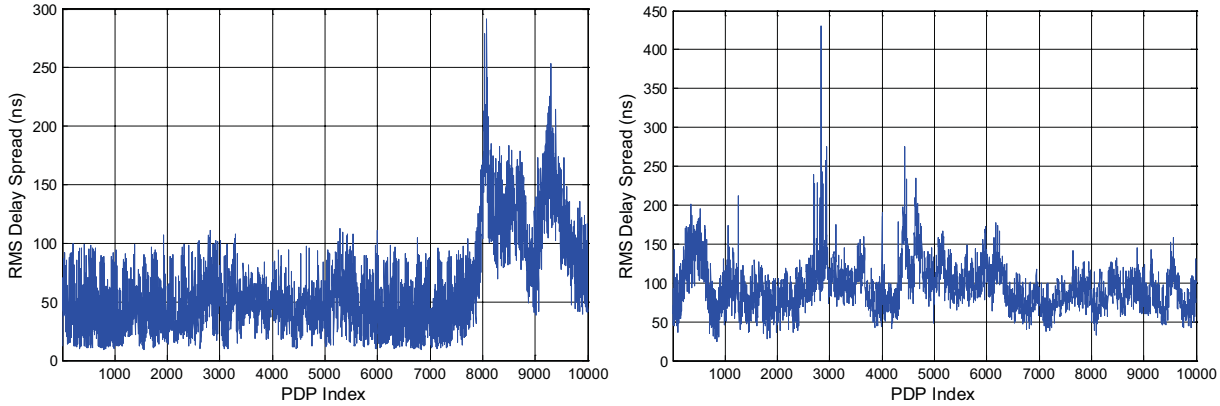

Figure 41. RMS-DS vs. PDP index (~link distance) for portion of FT2, file 1 (left) and file 2 (right) for C-band Rx1, with ground site at Oxnard, 11 June 2013.

The Channel Islands bay area, which lies between the Tx and Rx during this segment of flight, contains many residential houses. In addition, many boats can be clearly seen in the Google Earth view when "zoomed in," and these boats likely have large metallic surfaces. The large MPCs at large delay are due to reflections by this collection of boats[1], and possibly by the relatively calm water in the harbor as well. Thus even though the aircraft was not in the GS antenna main beam, and the GS antenna pattern in the backlobe direction alters the relative LOS component amplitude, these large MPCs do represent real reflections received from the boats, water, and potentially other structures between the Tx and Rx.

Shortly after the aircraft passed the middle point (blue arrow in Fig. 37, with flight track the orange line with arrow pointing west), the reflecting points of any ground-reflected MPCs (including those from boats) must lie on the west side of S. Harbor Boulevard (yellow line in the map of Fig. 37 to the left of the Channel Islands area). This means that MPCs due to boat and harbor water reflections cannot exist for this segment of flight. During this latter part of flight on the orange-segment path, the aircraft enters the GS antenna main beam. As noted, the "boat reflection" MPCs have excess delays up to 300 m, and this value is in approximate agreement with that computed via geometry. Example PDPs for the "boat reflection" condition are shown in Figure 42. The analytical result for the 2-ray (LOS plus single ground reflection) RMS-DS for FT2, file 1, is shown in Figure 43. When values in Fig. 42 are compared to results in Fig. 43, it is clear that *many* MPCs in addition to a surface reflection exist. Thus, these results show that significant multipath components exist in this AG channel "over-harbor" setting.

[1] Note that even though the Google Earth photo was not taken on the exact same day as the flight tests, it is still likely that the harbor area was highly populated with boats.

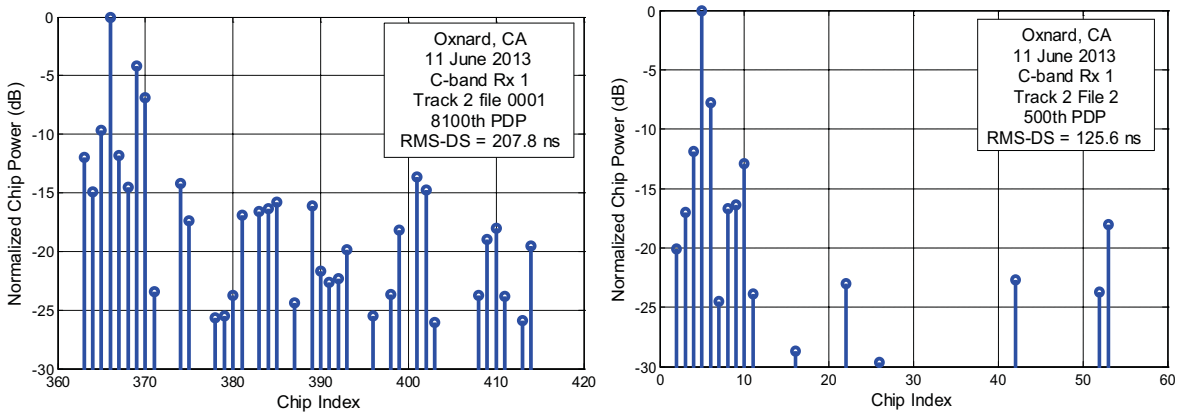

Figure 42. C-band Rx1 example PDPs for FT2 files 1 (left) and 2 (right), with likely MPCs from boat reflections, ground site at Oxnard, 11 June 2013.

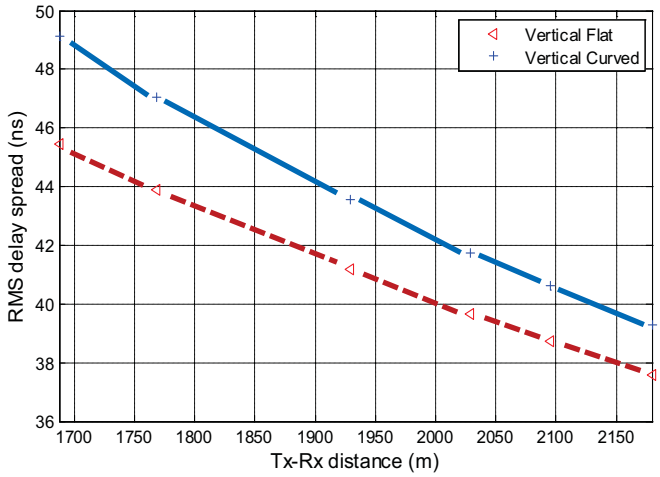

Figure 43. Analytical RMS-DS (2-ray model) for FT2 file 1, ground site at Oxnard, 11 June 2013.

Another interesting observation for FT2 files 1 and 2 concerns potential shadowing of the LOS MPC by the engine on the left wing. From flight recorder files for the period in which the path loss values were large, some fairly large values of roll angle (up to ~20 degrees) were observed. Although these roll angles are likely not the specific cause of the engine shadowing, it is possible that the C-band Rx1 connected to the antenna denoted LR (see Figure 44) was still partially obstructed by the engine during this portion of the flight.

Figure 44. View of underside of S3-B aircraft used in flight tests of 11 June 2013. Antenna locations are LF, LR, RF, and RR, with corresponding connections to the two L-band and two C-band receivers (Rx1 and Rx2 for each band).

In addition to engine shadowing and the GS antenna backlobe pattern, another contributing factor to the path loss variation in Fig. 40 is the variation of the *aircraft* antenna gain with aircraft orientation. Based upon manufacturer measured data, although the aircraft antenna patterns are nearly omnidirectional in azimuth, they are not omnidirectional in elevation, with a lobe that decreases in gain as elevation angle increases—this manufacturer data was also obtained with the antenna on a ground plane, without the pattern-deforming effects of the airframe itself, hence the manufacturer's patterns will not be precisely those in effect during flight tests. Unfortunately we can not easily measure the patterns for the antennas mounted on the aircraft, so this effect can only be estimated.

To illustrate the dynamic nature of the AG channel, in Figure 45 we show a sequence of C-band PDPs in time for FT2, file 2. This plot is for the fairly short link distances as indicated in Fig. 39, where the likely boat and harbor reflections occur. Figure 45 clearly illustrates the time variation of the CIR for both the main (LOS) component and the other MPCs.

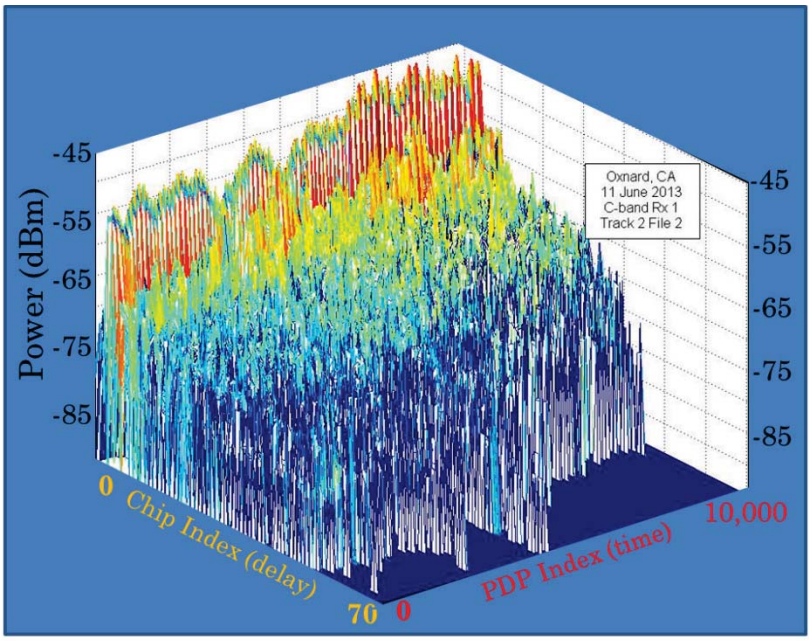

Figure 45. Sequence of C-band Rx 1 PDPs in time for FT2, file 2, ground site at Oxnard, 11 June 2013.

For comparison we also show some results for the L-band for this segment of flight (FT2). The flight track and elevation angle are those shown in Figures 38 and 39, and the following results are for L-band Rx1, file 1. In Figure 46 we show measured and analytical path loss. The L-band GS transmit antenna backlobe gain of -7 dB was used for estimating measured path loss in this case. The measured and analytical path loss values are within ~3 dB. Note also that significant MPCs from reflections can reduce received power when their phases oppose that of the LOS component, and this small-scale fading effect induces the fairly rapid (~3-8 dB) measured path loss variations in the figure.

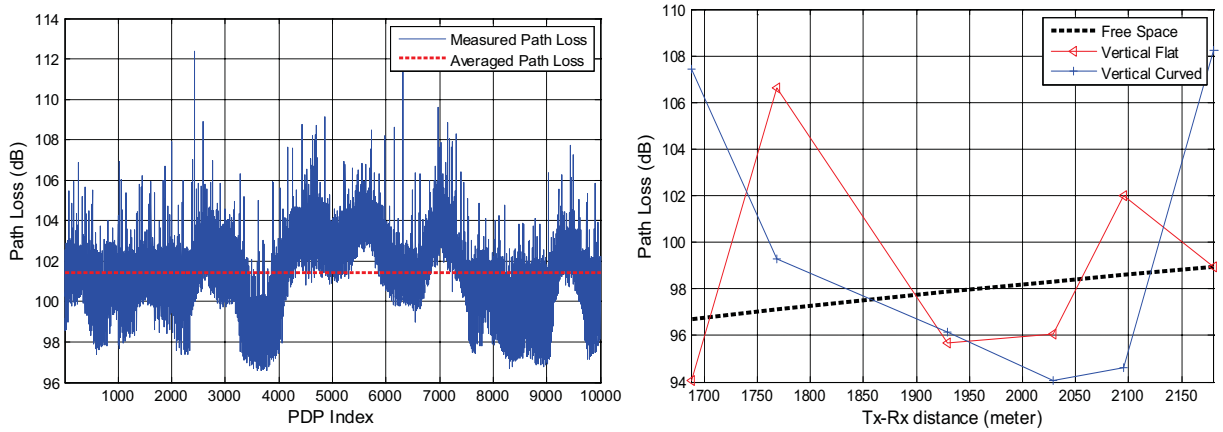

Figure 46. L-band Rx 1 measured path loss vs. PDP index (~time) (left) and analytical (2-ray) path loss vs. link distance (right) for FT2, file 1, ground site at Oxnard, 11 June 2013.

Figure 47 shows L-band RMS-DS vs. time for this file. Also included is a moving-average filtered version of the RMS-DS, to more clearly illustrate the trends. Note that in this plot we have removed approximately 5% of the RMS-DS values that were erroneous, referred to as "spikes" [1]. All RMS-DS values above 300 ns were removed. As with the C-band results, the analytical 2-ray RMS-

DS is much smaller (~40 ns) than the measured values, again corroborating the hypothesis of many MPCs due to boat and harbor reflections. An example PDP with large RMS-DS from this file is shown in Figure 48. The RMS-DS of this PDP is close to that found in C-band, shown in Figure 42 (left), illustrating expected consistency of these results across the two bands.

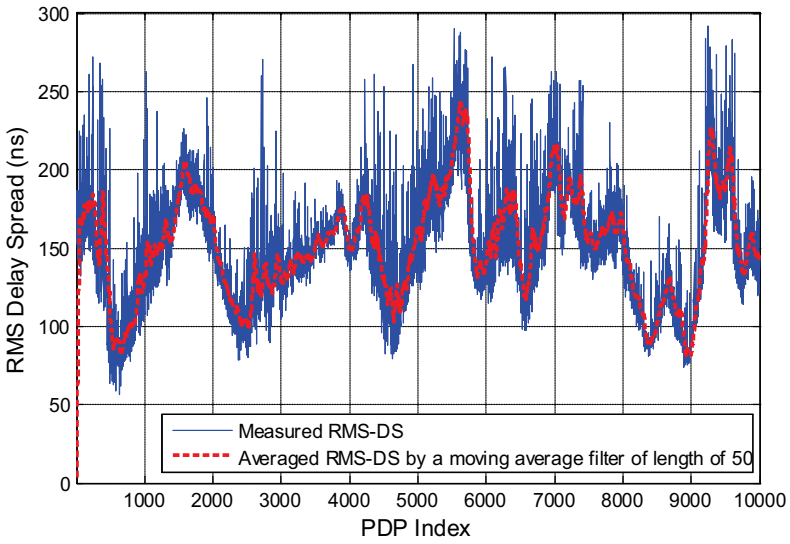

Figure 47. L-band Rx 1 measured RMS-DS vs. PDP index (~time) for FT2, file 1, ground site at Oxnard, 11 June 2013.

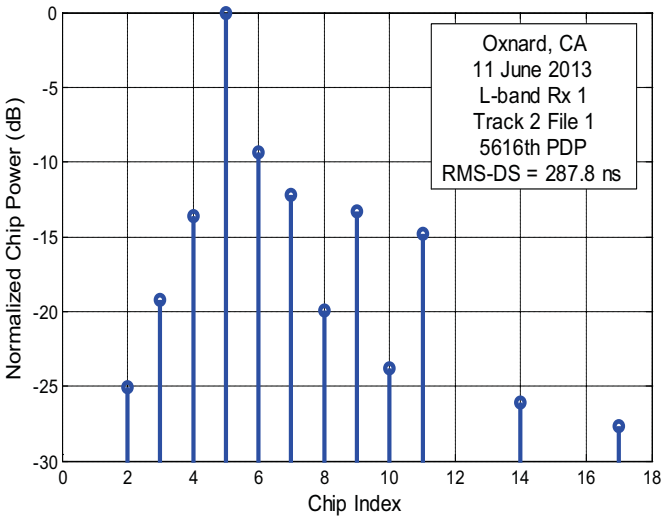

Figure 48. L-band Rx 1 example PDP for FT2, file 1, ground site at Oxnard, 11 June 2013.

4. Initial Channel Modeling

In prior reports (e.g., [19]) we discussed general modeling principles, model types, and the various structures of channel models commonly used in the modeling of time-varying wireless channels of various sorts. We repeat in Figure 50 a figure from [19] that shows the main elements used in constructing the AG channel models. In the work described here we have employed all the inputs noted at the top of this figure, with the possible exception of "GS features." In the over-sea measurements, no significant obstacles were near the GS, but we have used information regarding the GS antenna patterns.

From our geometric modeling we have the LOS and ground ray computations, which are best conducted using the curved-earth two-ray model. We also have measurement data that will enable us to compute MPC models—these are for the intermittent MPCs observed for most measurements, initially identified from their causing "bumps" in the RMS-DS vs. distance plots.

As yet we have no complete model for obstruction attenuation. For the vast majority of the flight tests in the over-sea setting, no airframe shadowing occurred. Occasional shadowing (or at least reflections) from parts of the airframe may have occurred for small portions of the measurements, but additional detailed geometric computations are required to clearly identify and quantify this. Since in other (not over-sea) flight tests, intentional wing shadowing was induced by specific flight maneuvers, we will likely begin our investigation of the airframe shadowing effect with data from those maneuvers. Information obtained from that data may then later enable us to quantify any shadowing present in the over-sea measurements. As noted though, since this shadowing—if it occurred—was very infrequent, initial AG channel models for this over-sea setting will not incorporate it.

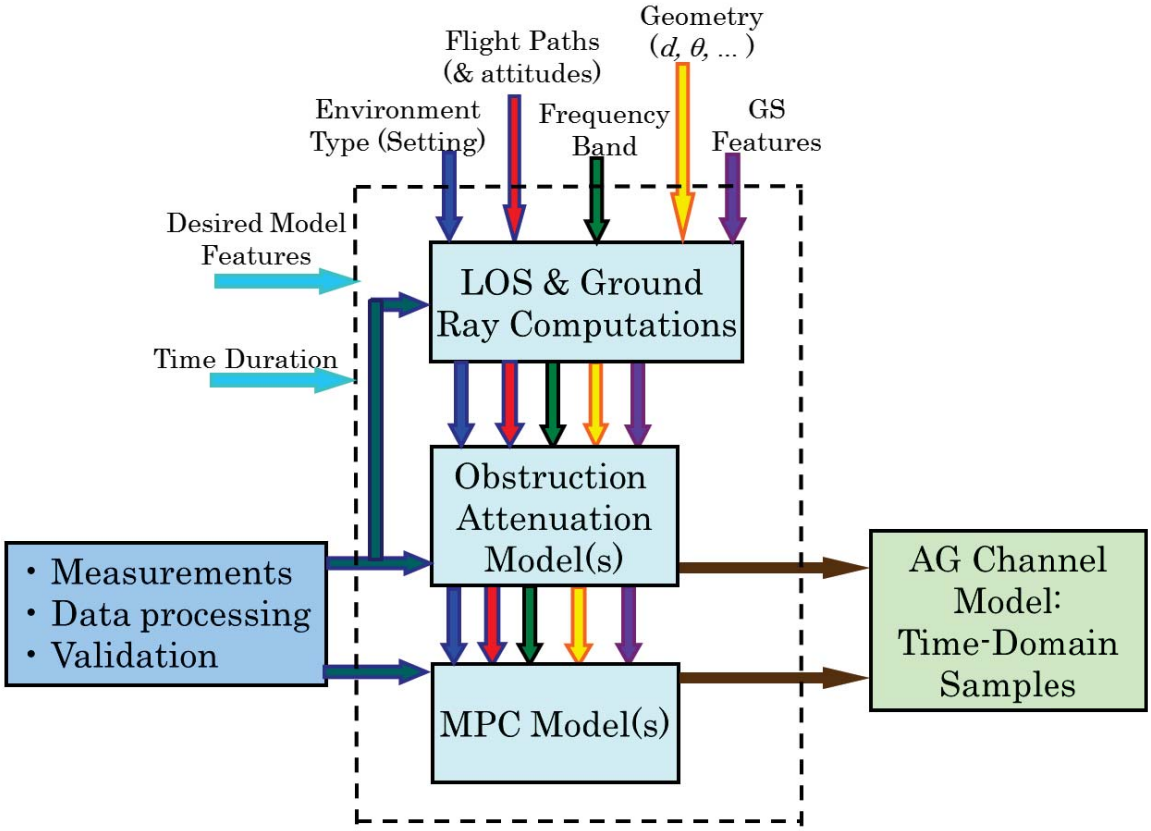

Figure 50. AG channel modeling procedure and model structure (from [19]).

The traditional method for modeling dispersive wireless channels is via the tapped-delay line (TDL) [20], a linear, finite impulse response filter with typically stochastic coefficients. More complex geometry-based stochastic channel models have also seen much recent attention [21], but the fairly simple over-sea environment may not warrant their complexity. A similar comment pertains to deterministic geometric models such as ray tracing [22]; a further shortcoming of deterministic models is that they cannot directly incorporate the rather rare or intermittent "third ray" we have observed in our measurements without a detailed model of the sea-surface and all objects that may be present on it.

For modeling propagation path loss, it is clear from our results that the curved-earth two-ray model incorporating sea-surface roughness does capture the essential trends in propagation path

loss. This model also captures the resulting two-ray RMS-DS characteristics, and these apply for link distances from approximately 1.5 km to 25 km. Before commenting further on refinements we may be able to apply to the curved-earth two ray model for path loss, we describe the TDL model.

Figure 51 illustrates the TDL structure. The input signal is $s(t)$, and the boxes with τ's inside denote delays: $\tau_s(t)$ is the time-varying relative delay of the surface reflection and $\Delta\tau_1(t)$ is the time-varying additional relative delay of the intermittent third ray. The LOS component is attenuated and phase shifted, and this is quantified by attenuation α_0 and phase shift ϕ_0, and analogous effects pertain to the surface-reflected component with attenuation α_s and phase shift ϕ_s. All parameters for the LOS and surface reflection (α_0, ϕ_0, τ_s, α_s, ϕ_s) can be computed from the curved-earth two ray geometry. The third ray effect is similarly modeled, but this component is modulated by a random "duration" process $z_1(t)$ [23], used to account for the appearance and disappearance of MPCs that cause the measured "bumps" in RMS-DS. Statistical characteristics for the delay $\Delta\tau_1(t)$, the amplitude $\alpha_1(t)$, and the duration process $z_1(t)$ will be obtained by aggregating measured results from all twelve flight tracks for which we have such data. Thus, the over-sea AG channel model will consist of the curved-earth two-ray model computations (see details in [1]), plus a set of statistics for the intermittent third ray component, consisting of statistical models for its frequency of occurrence, its duration, its delay (or propagation path length), its phase, and its relative amplitude.

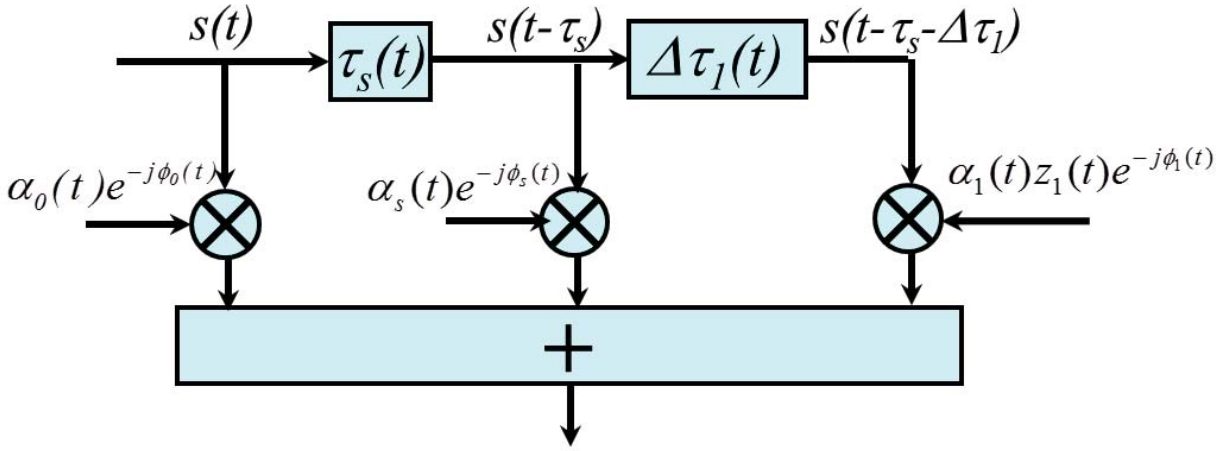

$$y(t) = \alpha_0(t)e^{-j\phi_0(t)}s(t) + \alpha_s(t)e^{-j\phi_s(t)}s(t-\tau_s(t))$$
$$+ z_1(t)\alpha_1(t)e^{-j\phi_1(t)}s(t-\tau_s(t)-\Delta\tau_1(t))$$

Figure 51. Tapped-delay line model for the over-sea AG channel.

We have begun processing the data for the intermittent 3rd ray, and in so doing, have also discovered the even rarer occurrence of a *4th ray*. This would be modeled by an additional tap in the TDL of Figure 51, along with its parameters ($z_2(t)$, $\alpha_2(t)$, $\phi_2(t)$, and $\Delta\tau_2(t)$). Table 5 contains the initial data on the 3rd & 4th rays, for C-band Rx1; additional similar data is being gathered for Rx2. The statistics are those derived from PDP data that show the "bumps" in RMS-DS vs. distance. We may in the near future refine the manner in which we define the data used for collecting 3rd and 4th ray statistics, but at present our criteria for identifying this data are as follows: (i) at least one individual instantaneous RMS-DS larger than 15 ns, and (ii) at least one value of the moving average RMS-DS (averaging window length 1000) larger than 15 ns. We also define bump boundaries where the rising and falling edges of the RMS-DS cross 12 ns. Once this data is isolated, we proceed to compute the required ray statistics. Data in *red italics font* for FTs 1 and 4 were illustrated in PDP sequence figures in prior sections of this report (Fig. 8 and Fig. 25). Data in *red italics font* for FTs 6 and 7 are illustrated in figures we describe subsequently. The column headings of Table 5 are defined as follows: ΔD is the link distance over which the aircraft traveled during the RMS-DS bump (note that for oval-shaped paths this distance may be very small during aircraft turns, but at a rate of

approximately 2000 PDPs/second, the bumps persist for durations from approximately 0.2 seconds up to 5 seconds); the Start Distance is the beginning link distance for the sequence of PDPs containing the RMS-DS bump; the number of PDPs in the bump is a measure of the bump duration and the Starting PDP Index is simply a counter that enables us to locate the third (and fourth) ray in the FT file; the RMS-DS statistics of maximum, median ("Med") and standard deviation ("Std") are provided for each bump; $\Delta\tau$ is the excess delay of the third ray relative to the LOS component; and statistics for relative power (minimum, Med, maximum, and Std) are given in the final four columns. From these statistics (aggregated with similar data from Rx2) we will develop models for the third, and possibly fourth ray as described in the previous paragraph.

Table 5. Statistics of the third ray found in RMS-DS "bumps" for FTs 1-10, C-band Rx1.

	Bump Index	Distance (m)		# of PDPs in Bump		RMS-DS (ns)			Δτ (ns)				Relative Power (dB)			
		ΔD	Start Dist.	#	Starting PDP Index	Max	Med	Std	Max	Mean	Min	Std	Min	Med	Max	Std
FT1	1	267	24112	4828	12753	19.8	12.7	2.2	80	68.7	60	0.50	26.9	20.3	10.4	2.6
	2	166	22338	4163	63771	18.7	12.5	2.2	80	60.0	60	0.05	27.0	21.7	15.9	2.6
	3	72	20956	2253	106233	16.6	12.3	1.9	80	63.6	60	0.38	27.9	23.9	18.0	2.5
	4	153	20730	4836	116199	21.2	14.0	2.4	80	60.1	60	0.06	27.8	20.1	12.1	3.9
	5	93	16906	2832	235031	15.9	11.6	1.7	80	65.3	60	0.44	29.3	26.0	17.3	2.5
	6	80	15101	2685	292066	17.6	12.2	1.8	80	62.6	60	0.33	28.7	23.9	18.0	2.6
	7	90	14575	2823	306213	19.0	11.7	1.8	120	66.0	60	0.53	29.7	25.5	17.4	3.0
	8	56	13241	1782	350729	16.8	12.2	1.7	80	67.4	60	0.48	29.2	24.6	16.9	3.0
	9	93	12914	3292	362154	17.7	12.0	2.0	80	64.2	60	0.41	29.5	25.3	16.3	3.0
	10	91	12130	2877	384478	17.8	12.6	1.6	80	65.7	60	0.45	29.2	25.0	15.4	2.9
	11	180	11949	3384	392859	18.5	12.5	2.4	80	63.0	60	0.35	28.6	22.6	12.9	3.8
	12	299	11661	7517	402201	16.6	10.0	1.8	80	67.3	60	0.48	30.0	27.2	16.9	2.8
	13	91	10632	2119	434659	19.4	13.3	2.1	80	61.4	60	0.26	29.3	22.8	13.0	4.1
	14	55	10182	1776	446976	18.6	12.9	2.1	80	62.9	60	0.35	29.0	24.3	14.8	3.3
	15	67	9839	2153	467938	18.3	12.8	1.8	80	61.8	60	0.29	29.8	24.5	15.1	2.9
	16	58	9671	1984	463324	20.5	14.0	2.2	80	61.9	60	0.29	27.6	20.8	12.1	3.8
	17	32	9575	2098	477779	18.9	13.3	1.8	80	60.5	60	0.15	28.8	23.1	14.3	3.6
	18	44	9457	1335	473164	19.5	14.5	2.4	80	60.3	60	0.12	28.2	20.5	11.3	4.2
	19	296	9225	9434	480476	18.5	10.7	1.8	80	67.1	60	0.48	30.0	26.0	15.5	3.2
	20	*99*	*2286*	*4392*	*715528*	*51.0*	*11.6*	*8.3*	*460*	*93.7*	*60*	*5.10*	*29.9*	*21.4*	*11.6*	*4.2*
FT2	1	344	8054	8469	290206	20.1	10.9	2.4	100	66.5	60	0.47	30.0	26.0	11.3	3.5
	2	83	18404	2974	627963	20.8	13.1	2.4	100	100.0	100	0.00	20.9	20.1	19.5	0.5
	3	103	19543	2296	652890	21.0	14.7	2.5	80	80.0	80	0.00	18.9	17.1	15.9	0.9
	4	80	2031	4910	685976	21.8	13.	2.5	100	100.	10	0.0	16.	16.	15.	0.7

			8				6			0	0	0	9	8	6	
	5	179	28022	7487	928999	20.9	11.5	2.6	80	80.0	80	0.00	19.9	17.4	13.5	1.4
FT3	1	245	42225	4505	235999	16.0	11.0	2.5	60	60.0	60	0.00	16.6	13.0	11.9	2.0
	2	522	34157	14239	509588	22.6	13.2	2.7	80	61.0	60	0.22	19.2	11.6	7.1	2.1
	3	226	23479	7979	831639	18.4	11.8	2.2	100	74.3	60	0.45	24.0	19.2	14.5	1.8
	4	213	20614	7204	938402	42.0	14.0	2.8	80	61.7	60	0.28	27.8	18.4	8.2	4.8
	5	203	19233	6014	973633	18.3	12.3	2.1	80	62.8	60	0.34	28.4	23.9	15.8	2.8
FT4	*1*	*139*	*23220*	*5102*	*113767*	*20.3*	*11.4*	*2.8*	*180*	*162.5*	*60*	*1.40*	*30.0*	*27.1*	*17.6*	*3.6*
	2	15	19570	7234	1490569	947.8	11.8	16.5	120	66.4	60	0.49	24.3	19.0	12.2	1.9
	3	1	19523	4143	1533328	17.2	14.3	1.4	80	62.1	60	0.31	21.1	16.8	14.2	1.4
	4	53	19743	15151	1693991	22.9	11.7	2.9	80	63.7	60	0.39	22.4	14.0	8.7	3.2
FT5	1	67	25439	6133	260643	295.7	10.5	59.9	100	75.5	60	0.43	21.6	19.1	16.5	1.1
	2	169	22429	6197	1081820	408.2	11.5	29.0	120	68.3	60	0.65	24.3	17.3	13.4	2.1
FT6	1	6	18977	1741	320243	209.8	9.6	36.1	80	67.0	60	0.48	22.1	19.8	17.2	1.2
	2	*143*	*22315*	*7959*	*641054*	*185.6*	*10.7*	*40.3*	*200*	*114.5*	*60*	*2.38*	*30.0*	*28.0*	*15.6*	*3.7*
	3	42	26719	3362	926737	347.7	9.8	97.5	100	77.0	60	0.49	21.9	20.1	18.6	0.9
	4	33	26203	3364	968367	214.9	9.2	44.2	80	76.7	60	0.38	23.4	21.9	19.8	0.8
	5	63	21573	5795	1775235	20.3	12.5	2.8	160	66.3	60	0.56	25.6	18.9	12.9	1.9
FT7	1	33	19636	9894	120080	20.8	12.3	3.1	100	80.2	80	0.10	21.0	18.0	13.6	1.4
	2	52	19598	13166	141825	20.6	11.7	3.2	80	80.0	80	0.00	20.8	17.9	13.3	1.6
	3	*449*	*23184*	*23303*	*610937*	*266.5*	*9.6*	*6.4*	*180*	*156.4*	*80*	*1.47*	*26.7*	*19.3*	*11.3*	*2.5*
	4	151	26021	14759	954565	228.1	9.1	10.2	100	80.3	80	0.11	23.3	20.7	14.1	1.6
	5	98	25902	13250	1485674	21.3	10.7	2.6	80	80.0	80	0.00	23.0	21.0	17.8	1.2
	6	368	22434	11536	1737874	21.1	12.6	2.8	120	85.6	80	0.49	21.9	19.8	15.7	1.5
FT8	1	170	19592	5880	220255	20.5	13.9	2.3	80	80.0	80	0.00	27.4	26.0	23.2	0.9
	2	192	6875	8012	651461	324.3	10.4	19.6	100	80.0	80	0.03	30.0	28.8	19.5	2.4
FT9	1	235	17763	8402	633370	20.5	11.6	2.7	80	80.0	80	0.00	21.7	17.9	13.1	1.6
	2	252	18779	10011	667415	21.0	11.5	2.6	80	80.0	80	0.00	27.6	20.5	14.5	3.0
	3	458	31508	14159	1102487	22.0	11.3	3.0	80	80.0	80	0.00	17.8	17.4	16.1	0.7
FT10	1	612	39422	14613	246774	22.8	12.5	3.7	100	89.3	80	0.50	20.4	17.7	14.6	1.5
	2	96	23110	3882	767183	20.4	12.8	2.3	80	80.0	80	0.00	27.9	20.4	14.1	2.3

As noted, the third ray is intermittent: it occurs approximately 2.5% of the time. In addition, an even rarer fourth ray is present in some PDPs, approximately 0.29% of the time. This is

illustrated in Figures 52 and 53 for bump indexed #2 in FT6 ($\Delta\tau_2 \cong 200$ ns), and in Figures 54 and 55 for bump indexed #3 in FT7 ($\Delta\tau_2 \cong 180$ ns). Although as noted, we are not able to identify with certainty the source of the third (and fourth) rays, for those shown for FTs 4, 6, and 7, the MPCs may possibly emanate from the same reflecting object since the shape of these flight tracks, the link distances, and excess delays of the MPCs are similar.

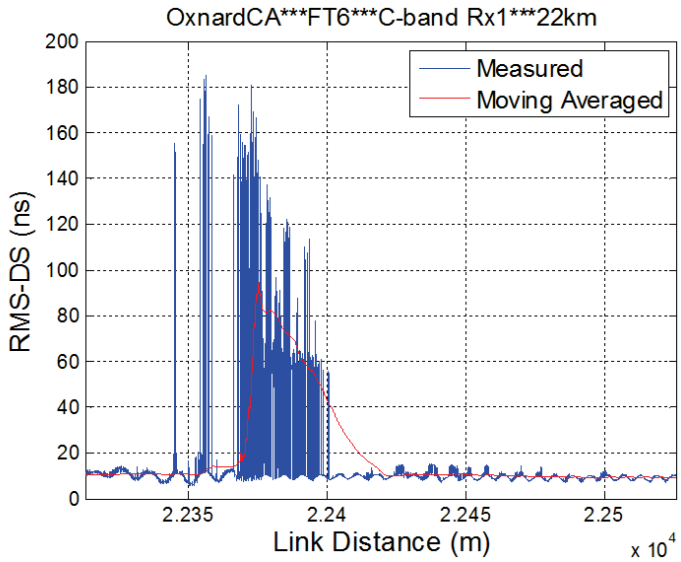

Figure 52. Measured C-band Rx1 RMS-DS vs. distance for small segment of FT6.

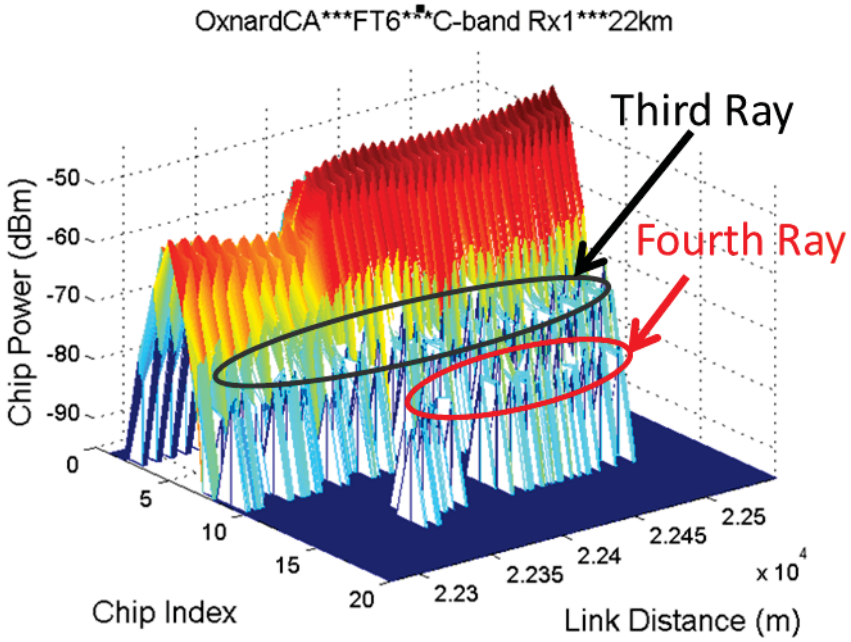

Figure 53. Sequence of PDPs for measured results of C-band Rx1, segment of FT6 of Fig. 52.

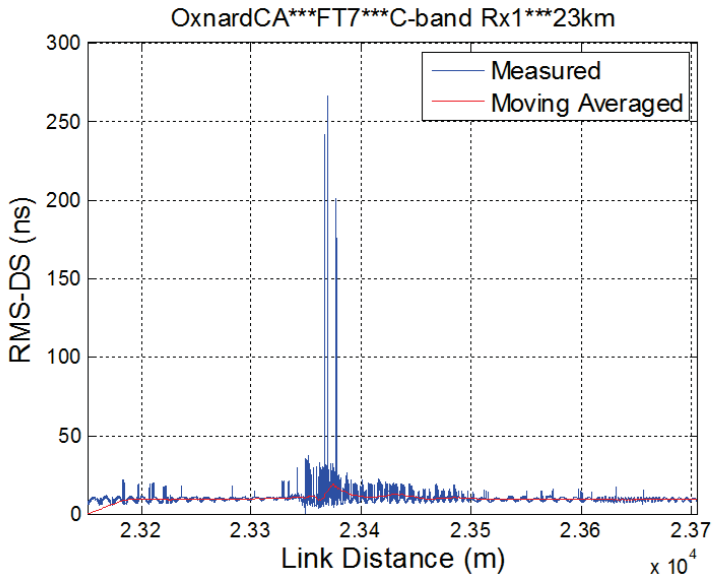

Figure 54. Measured C-band Rx1 RMS-DS vs. distance for small segment of FT7.

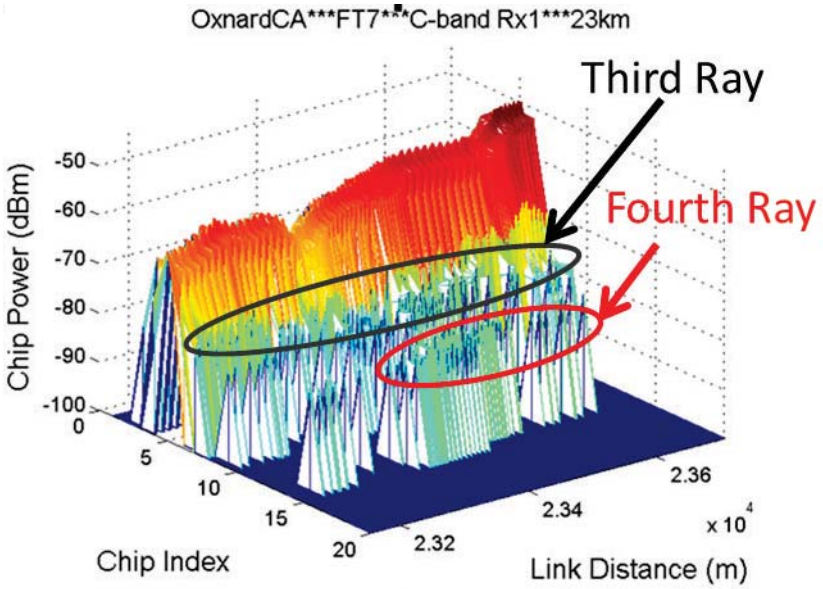

Figure 55. Sequence of PDPs for measured results of C-band Rx1, segment of FT7 of Fig. 54.

As noted several times, the measured path loss exhibited differences from that of the two-ray model at nearly all values of distance. Some of this is attributable to aircraft antenna gain variation, and to a lesser degree to fading caused by additional unresolvable MPCs. Sea surface roughness is also a secondary contributor to this. Despite the reasonably good agreement with the curved-earth two-ray model, it is of interest to consider methods to augment this model in order to obtain better agreement with measurements. To that end we show in Figures 56-59 histograms of path loss data for FTs 1, 2, 4 and 10. In a sense, these figures do not provide any additional information beyond that already contained in the corresponding plots of path loss vs. distance, provided in the previous section. Yet they are a new way to *view* this data.

The histograms show path loss for free-space, the flat-earth two-ray model, the curved-earth two-ray model, and that resulting from measurements. The width of the bins in all figures is 1 dB. The measured path loss distributions of the straight path FTs (FT1, 2 and 10) basically agree with

the two-ray theoretical distributions, but with means that differ by a few dB, and sometimes multiple modes. However, for the oval FT4, the measured and theoretical results are more distinct in shape. The maximum value of path loss may be of the most interest. The maximum values for the C-band receivers are no larger than those for the analytical results, whereas the maximum values in L-band are approximately 10 dB larger than the analytical results, explicitly for FT1 and 4.

It is not readily apparent how to augment the curved-earth two-ray model to yield better agreement with measured path loss (other than the impractical measurement of the aircraft antenna patterns with the aircraft present). One could add some relatively fast-varying "noise" to the model (implemented by making the amplitudes of the LOS component or surface reflection or both be "noisy"), but this is clearly ad hoc, and likely situation specific. Adding several dB to the curved-earth path loss values (akin to adding link margin) might also be done; this would be of most value for the L-band case where some of the path loss maxima are substantially larger than that predicted by theory. As additional work on this data, on airframe shadowing, and on data from other flight tests proceeds, we may return to the topic of augmenting the curved-earth two ray path loss model.

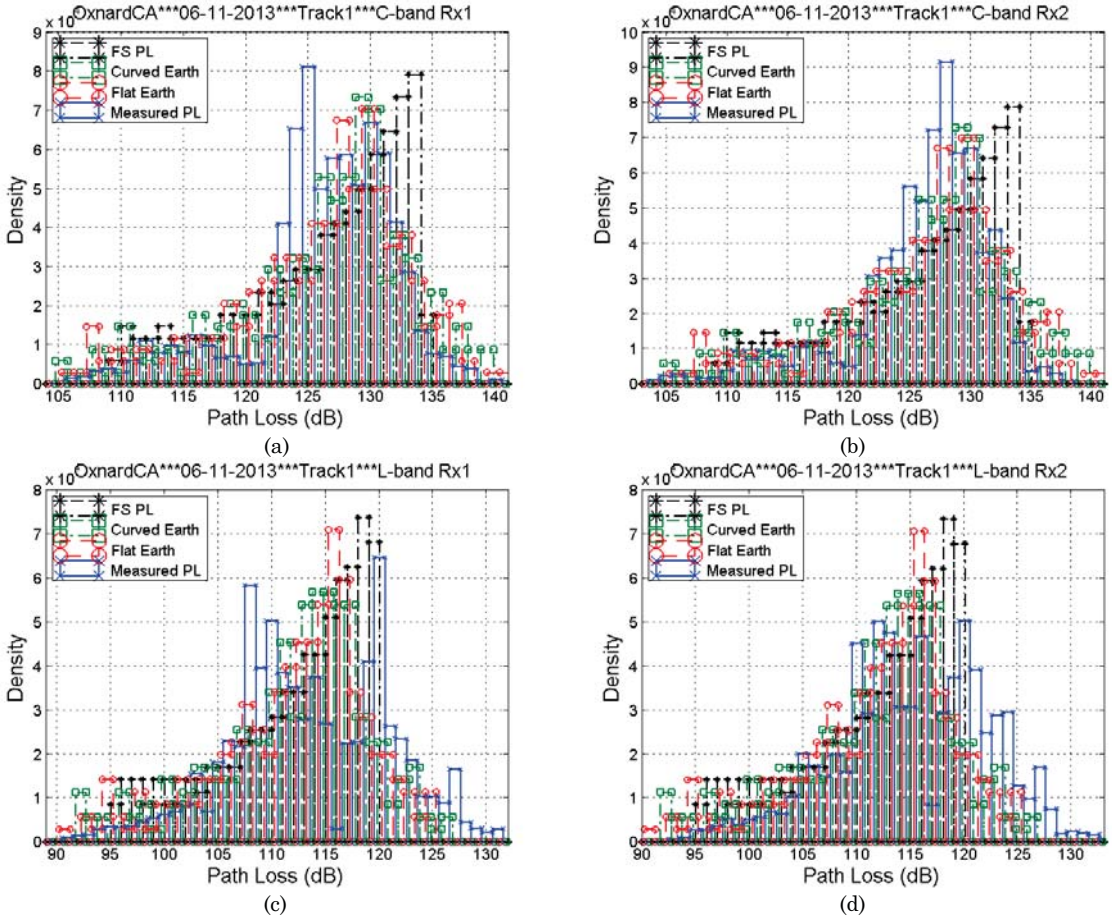

Figure 56. Distribution of path loss of FT1 (a) C-band Rx1; (b) C-band Rx2; (c) L-band Rx1; (d) L-band Rx2.

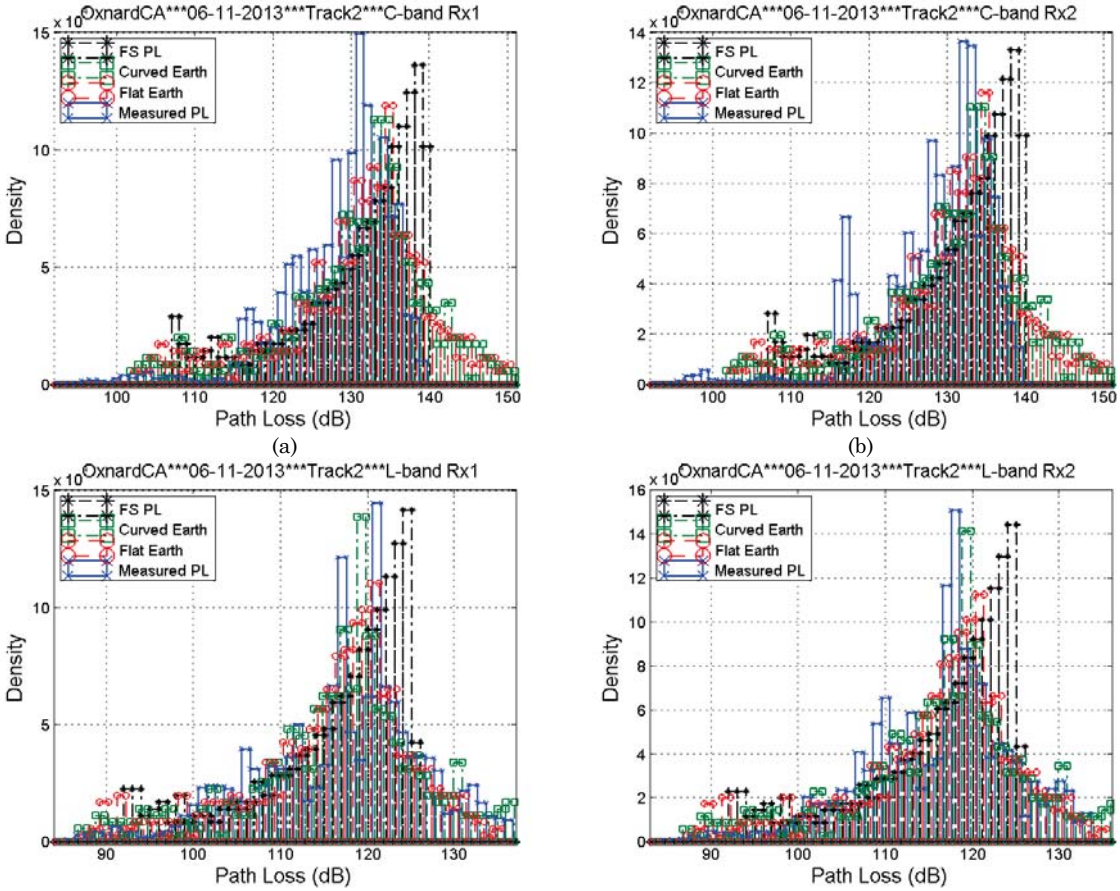

Figure 57. Distribution of path loss of FT2 (a) C-band Rx1; (b) C-band Rx2; (c) L-band Rx1; (d) L-band Rx2.

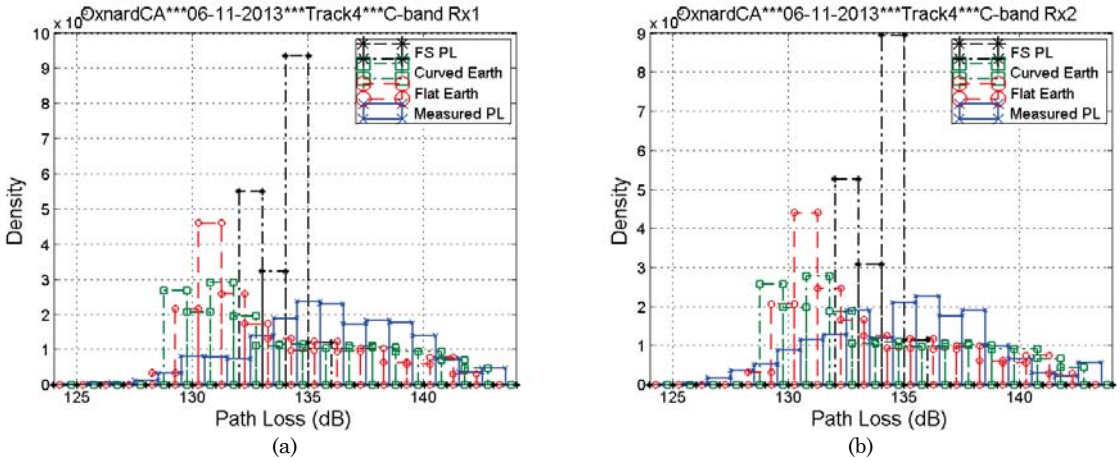

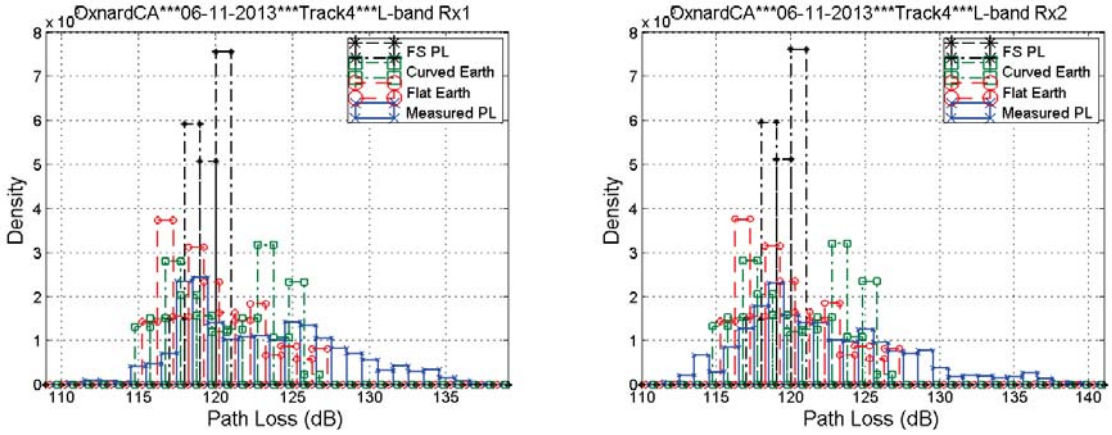

Figure 58. Distribution of path loss of FT4 (a) C-band Rx1; (b) C-band Rx2; (c) L-band Rx1; (d) L-band Rx2.

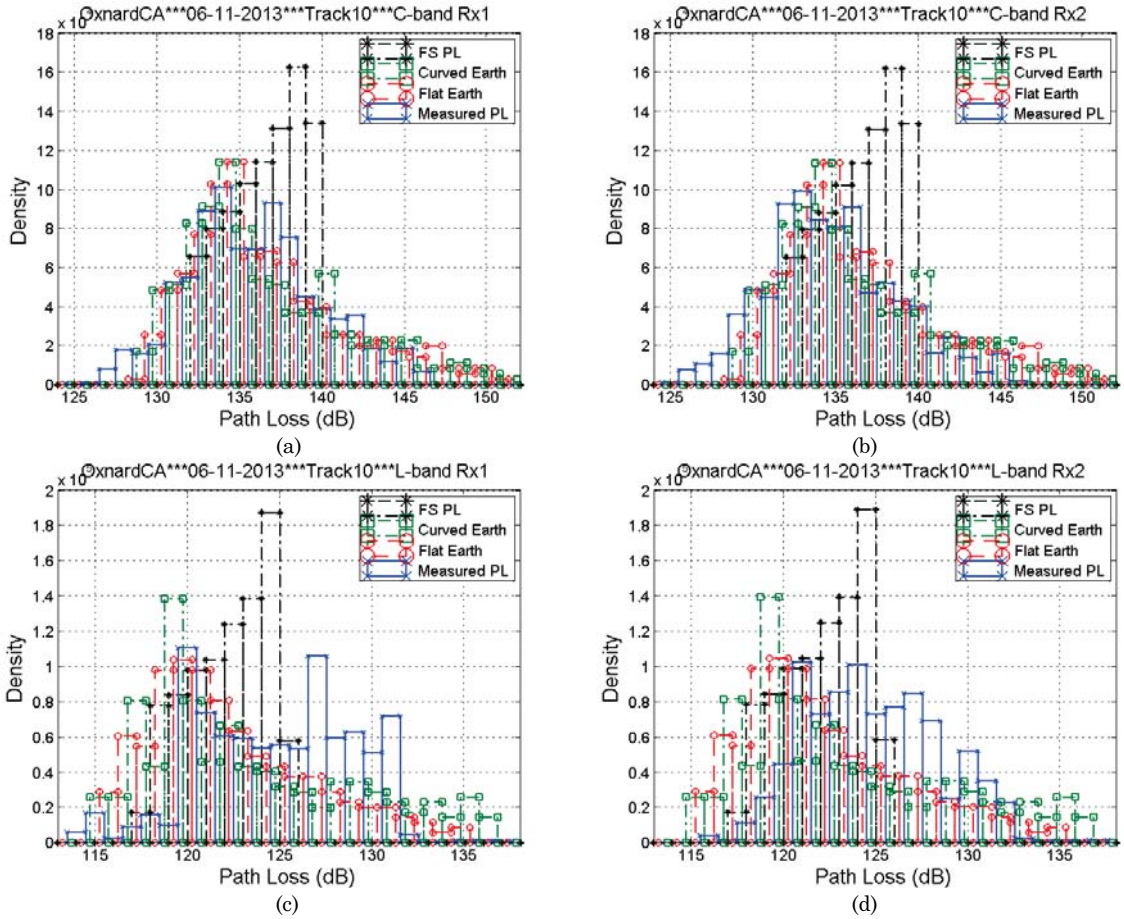

Figure 59. Distribution of path loss of FT10 (a) C-band Rx1; (b) C-band Rx2; (c) L-band Rx1; (d) L-band Rx2.

As a final comment on the path loss results, we show in Figure 60 a sequence of PDPs for FT10, for link distance approximately 20.2 km (cf. Figure 34). The LOS component clearly proceeds along the two-ray pattern and reaches a null near the center of the range of link distance values. During this null, additional components due to noise rapidly exceed the threshold and get through to the receiver output, in essence drastically reducing the signal to noise ratio during the null. Although this two-ray behavior is as expected, it is worth commenting on the consequences of this effect for UAS communications. With the longer L-band wavelength, the sea (and earth) surface are

relatively smoother than at C-band. This has the effect of making the surface reflection stronger, and when its relative phase is nearly opposite of that of the LOS component, the two components nearly cancel, yielding very large path loss values. This is clear in the path loss plot of Figure 34, wherein the two-ray cancellation yields path loss values more than 20 dB larger than the free-space value. Even larger values of attenuation are possible for smoother surface conditions. For link distances on the order of 20 km this additional path loss may not sever the communication link, but such large and rapid attenuations will require a substantial amount of link margin.

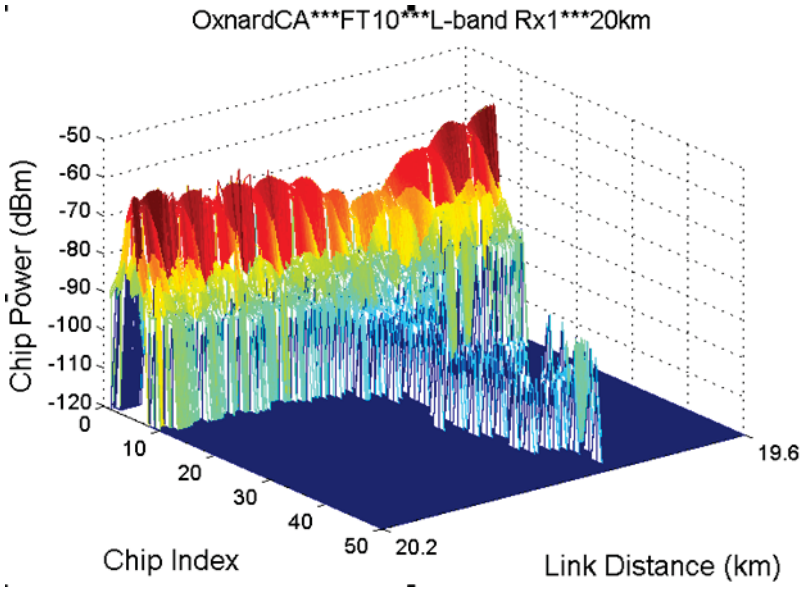

Figure 60. Sequence of PDPs for FT10, illustrating two-ray effects on the LOS component.

5. Literature Review Update

This section provides an update to the ongoing project literature review. Beyond the usual technical literature, some references in the popular press were also obtained. In [24], the authors discuss the applications of UAS and how public perception of the use of such "drones" is generally negative when these aircraft can be used for surveillance. The article [25] similarly cites negative public perception. It describe the US military's "not reassuring" safety record to date, and describes both cutting edge research (micro-UAS) as well as the current use of UAS in police and public safety arenas. This article also briefly describes the FAA's current policies, and potential "new laws" that would address the "safe integration" of UAS into the US airspace.

The authors of [26] describe their work on computer simulations of UAS in an air-to-air ad hoc network. Their study may be somewhat impractical, in that they assume a 20 MHz channel bandwidth at several frequencies from 2-5 GHz, but given those assumptions, the link analysis is reasonable. They use a spread spectrum signal (wideband code-division multiple-access (WCDMA), one of the 3rd generation cellular standards), but do not conduct a rigorous analysis of the multi-user interference present in such systems. Their network model may be of some interest in future, similar studies. The same authors present another study in [27] using some of the same system conditions (CDMA, 20 MHz bandwidth, etc.); here they do account for multi-user interference, but assume a rather large complexity for the receivers.

In [28] the authors provide a survey of the L-band digital aeronautical communication systems (LDACS). A brief history and some rationale for the two schemes (LDACS-1 and LDACS-2) are provided, followed by a review of the system characteristics. In contrast to prior such reviews, little actual technical evaluation is present in this paper.

Reference [29] addresses air-to-air networking with directional antennas and provides a description of a proposed MAC protocol. They assume some ideal conditions, such as perfect knowledge of neighboring aircraft, and fully steerable beams, then evaluate their network performance in computer simulations (using OpNet). Their results are highly questionable since their model for the air-to-air channel is unrealistic except for very unusual cases: specifically they include a model for signal shadowing, and Ricean fading, but do not specify the key parameters of shadowing standard deviation or correlation time, or Ricean K-factor. Such shadowing, if from surface obstacles, would only occur for a collection of *very* low-flying UAS. If the shadowing is meant to be due to airframes, the model is purely conjectural. They apparently use IEEE 802.11b transmissions, but the simulation model employs only a simplistic rendition of the physical layer.

The work in [30] is an interesting study with empirical results. The authors simulate a UAS using a dirigible, and conducted measurements with a GS near the edge of a forest environment. The GS antenna height is low (~1.5m), and the elevation angles were approximately 5 and 7 degrees. With multiple (two, dual-polarized) antennas at the GS, they quantified antenna diversity gains for various combining methods at a frequency of 2 GHz, and link distance approximately 4 km. Results show combining performance similar to that attained in terrestrial channels with Rayleigh fading, but actually slightly worse (this interesting effect is not further analyzed). A perhaps surprising result is that when their Rx was placed in an open field, diversity gains were still achieved, illustrating that some small scale fading effects were present even in the open field of their experiment.

In [31] the authors describe their proposal for a new MAC scheme for air-to-air ad hoc networking. These authors also employ CDMA, and assume fairly sophisticated aircraft receivers that can not only cancel self-interference (co-site), but also assume knowledge of other parameters (spreading codes of other aircraft, channel gains, and delays). The protocol is moderately complex, but its biggest drawback appears to be that it requires centralized control—not common in ad hoc conditions.

Reference [32] describes a so-called stratospheric relay channel that employs a high-altitude dirigible that acts as a relay between a transmitter and receiver on the ground. The authors employ the currently-popular geometry-based stochastic channel model for their study, and hence the three-dimensional geometric analysis is complex, but also must resort to some simplifications (e.g., single-bounce scattering and a rich multipath environment around both ground terminals). Although largely an exercise in geometry, their model does provide some interesting analytical results for spatial correlation with 2 by 2 MIMO antennas for this relay setting.

Another very recent reference is [33], which describes MIMO results for a 4 by 8 (or 8 by 4) array. Measurements were made with a 5.1 GHz uplink, and 5.8 GHz downlink, with both bands employing 100 MHz channel bandwidths. The measurements used a small UAS mounted on top of a pole of height 400 feet; no actual flying was conducted, but the UAS attitude was varied over two of the three axes (pitch and yaw). Antenna array inter-element channels were measured, but this data was not reported. The authors then describe a MIMO transmission scheme (modified D-BLAST) that attains good performance by repetition of symbols across transmit antennas, combined by variable data rates, spread spectrum using Walsh codes, and powerful error correction using LDPC codes. Simulations of their (clearly complex) scheme over some measured channel responses show gains in SNR over the original D-BLAST scheme if all polarizations of the array elements are identical, whereas D-BLAST outperforms the new scheme if polarizations are "mixed" (alternate elements use horizontal, vertical, …).

An interesting use of aircraft—as relays for terrestrial node connectivity—is explored in [34]. Although not directly aimed at UAS, if UAS are deployed in vast numbers in the future, the article would pertain to UAS as well. The authors make a reasonable case for the argument that over many landmasses (continental Europe and North America in particular), the spatial density of aircraft aloft is large enough to provide line-of-sight coverage to large populations for a large fraction of time. Based upon this observation, and actual data on aircraft aloft, they analyze coverage probabilities for various "cell" sizes, and show that for moderate sized cells (e.g., radius ~55 km, elevation angle $\geq 10^{o}$),

coverage probabilities are larger than 0.6 for over half the day. The authors also propose a slotted ALOHA medium access scheme for the uplink, and analyze its performance.

In [35] the authors[2] describe their first-hand experience with electronic signaling disruption of UAS, and review the vulnerabilities of GPS, ADS-B, and potential CNPC links in the presence of jamming or spoofing. The susceptibility of existing UAS to disruption is identified as a very serious problem with no easy solution. The authors also mention the challenging policy issues that complicate safe UAS deployment. The primary message is that if measures are not taken to secure UAS communication, navigation, and surveillance links, these links will almost surely be intentionally compromised at some time.

Reference [36] addresses measurements and models for a low-elevation angle UAS channel in urban areas. Elevation angles range from approximately 1-5º, and a dirigible was used as the UAS at flight altitudes from 100-170 m. Link distances were 1-6 km. This paper provides narrowband measurement and modeling results, and does not attempt to address wideband channel characteristics such as RMS-DS. Measurements were made at 2 GHz with the receiver antenna height only 1.5 m above ground level, in urban Prague, Czech Republic. Data recorded was limited to pitch and roll angles below a magnitude of 10º. The authors modeled fading as overall Ricean in distribution, with the "direct" (often LOS or diffracted) signal component amplitude modeled as varying lognormally, and the diffuse component power modeled as lognormal as well. Correlation distances on the order of 2 m (~ 13λ) were found to hold for a Gaussian spatial autocorrelation model. The two components (direct and diffuse) were found to be mildly correlated, with correlation ranging from 0.3 to 0.56, and larger correlations found at larger link distances. The resulting narrowband amplitude fading model is based upon the well-known Loo model [37], with an additional lognormal variation to the diffuse component. When the diffuse and direct components are modeled as independent, the agreement with measured data was good.

6. Summary and Conclusion

In this report we described measurement results for the over-sea AG channel, taken in June 2013 with the GS located near the beach in Oxnard, CA, and the aircraft flying over the Pacific Ocean. The measurements consisted of simultaneous power delay profiles in both L-band and C-band, received by two separate antennas in each band. From the power delay profiles we have computed propagation path loss, quantified channel dispersion via root-mean square delay spread, and also computed correlation coefficients among the strongest received signal component on all four antennas. All these results will contribute to the development of accurate models for the over-sea AG channel. In addition, some unanticipated but useful results for the over-harbor channel were obtained, and these will be employed for developing a specific AG channel model for this environment. The report also described related work for the over-sea AG channel, and discussed the planned structure and characteristics of the final over-sea AG channel model. An update to the ongoing project literature review was also included. A detailed investigation of the noise characteristics observed in the flight tests is presented in two appendices.

Overall propagation path loss is fairly well modeled by the curved-earth two-ray model. Despite its increased complexity in comparison to the flat-earth approximation—accurate for shorter link distances—the computational complexity of the curved-earth model is in no way prohibitive for currently available general purpose computers. Disagreements between this model and measured results are attributable in part to aircraft antenna gain variation, and to a much lesser degree to occasional airframe reflections or shadowing, and to unresolvable multipath components. The channel dispersion in the over-sea case is also well represented by the curved-earth two-ray model plus an additional intermittent "third ray," and even rarer "fourth ray." Such a third ray was also found in independent over-sea measurement campaigns reported in the literature (e.g., [16]).

[2] D. W. Matolak had the pleasure of meeting and conversing with the second author of [35], when both were invited speakers at the IEEE New Technologies Industry Seminar (NTIS 2013), at Boeing Corp., Everett, WA, on 22 August 2013.

Statistics for this third and fourth ray are being collected, from which we will devise a complete statistical model for their relative frequency of occurrence, duration, and relative delay and amplitude. This will essentially complete the single-input/single-output over-sea AG channel model development. For our multi-antenna measurements we have observed that in straight flight paths away from or toward the GS, signals on the two C-band aircraft antennas are highly correlated, but for oval-shaped paths in which the relative orientation of the two antennas changes, correlation varies widely with generally small average values. Thus C-band antenna diversity may provide some diversity gains. For the L-band results, correlation between the aircraft antennas was small for all flight path shapes, with slightly larger values at larger link distances. Part of the reason for this low correlation is the inherent variation in the L-band channel sounder's response; although this variation may not be easily removed, it is a task on which we will continue to work, and which may result in higher values of correlation between the L-band antennas for straight flight paths. The largest diversity gains will clearly be obtained *between* the two-bands, as the correlation between the C-band and L-band signals was found to be essentially zero.

Future work includes analysis of measured data for AG channel flight tests conducted in different environments, which include hilly terrain, desert, urban, and suburban settings. Results for the over-fresh-water AG channel will be investigated next, along with development of stochastic models for all the "over-water" settings: the over-sea, over-harbor, and over-fresh-water cases.

References

[1] D. W. Matolak, R. Sun, "AG Channel Measurements & Modeling: Initial Analysis & Flight Test Planning," (Report #2) NASA Grant #NNX12AD53G, 8 June 2012.
[2] D. W. Matolak, "AG Channel Measurements & Modeling: Year One Results," NASA Grant #NNX12AR56G, 26 July 2013
[3] D. W. Matolak, R. Sun, "AG Channel Measurements & Modeling: BVS Channel Sounder Performance: Measurement Stability," (Report #5) NASA Grant #NNX12AR56G, 19 April 2013.
[4] D. W. Matolak, R. Sun, "AG Channel Measurements & Modeling: Initial Channel Sounder Laboratory & Flight Tests—Supplementary Report," (Report #4) NASA Grant #NNX12AR56G, 1 March 2013.
[5] D. W. Matolak, R. Sun, "AG Channel Measurements & Modeling: Initial Channel Sounder Laboratory & Flight Tests," (Report #3) NASA Grant # NNX12AR56G, 29 January 2013.
[6] National Geographic Data Center website, http://www.ngdc.noaa.gov/geomag-web/
[7] National Climate Data Center website, http://www.ncdc.noaa.gov/
[8] C. A. Levis, J. T. Johnson, F. L. Teixeira, *Radiowave Propagation: Physics and Applications*, John Wiley & Sons, Hoboken, NJ, 2010.
[9] H. V. Hitney, L. R. Hitney, "Frequency Diversity Effects of Evaporation Duct Propagation," *IEEE Trans. Antennas & Prop.*, vol. 38, no. 10, pp. 1694-1700, October 1990.
[10] H. V. Hitney, "Refractive Effects from VHF to EHF Part A: Propagation Mechanisms," *Advisory Group for Aerospace Research and Development (AGARD) Lecture Series*, 1994.
[11] H. V. Hitney, "Refractive Effects from VHF to EHF Part B: Propagation Models," *Advisory Group for Aerospace Research and Development (AGARD) Lecture Series*, 1994.
[12] H. V. Hitney, J. H. Richter, R. A. Pappert, K. D. Anderson, G. B. Baumgartner, "Tropospheric Radio Propagation Assessment," *Proceedings of the IEEE*, vol. 73, no. 2, pp. 265-283, February 1985.
[13] International Telecommunications Union (ITU), "The Radio Refractive Index: Its Formula and Refractivity Data," *ITU Recommendation ITU-R P.453-10*, February 2012.
[14] A. L. Martin, "VHF and Microwave Propagation Characteristics of Ducts," [Online] http://www.df5ai.net/ArticlesDL/VK3KAQDucts2007V3.5.pdf , 7 October 2013
[15] International Telecommunications Union (ITU), "Effects of Tropospheric Refraction on Radiowave Propagation," *ITU Recommendation ITU-R P.834-6*, January 2007.
[16] Y. S. Meng, Y. H. Lee, "Measurements and Characterization of Air-to-Ground Channel Over Sea Surface at C-Band with Low Airborne Altitudes," *IEEE Trans. Vehicular Tech.*, vol. 60, no. 4, pp. 1943-1948, May 2011.
[17] Y. H. Lee, Y. S. Meng, "Empirical Modeling of Ducting Effects on a Mobile Microwave Link Over a Sea Surface," *Radioengineering*, vol. 21, no. 4, pp. 1054-1059, December 2012.
[18] R. Vaughan, J. B. Anderson, *Channels, Propagation and Antennas for Mobile Communications*, IET Press, UK, 2003.
[19] D. W. Matolak, "AG Channel Measurements & Modeling: Initial Report on Flight Test Planning and Narrowband Measurements," (Report #1) NASA Grant # NNX12AD53G, 20 March 2012.
[20] J. G. Proakis, *Digital Communications*, 4th ed., McGraw-Hill, New York, NY, 2001.
[21] J. Karedal, F. Tufvesson, N. Czink, A. Paier, C. Dumard, T. Zemen, C. F. Mecklenbrauker, A. F. Molisch, "A Geometry-Based Stochastic MIMO Model for Vehicle-to-Vehicle Communications," *IEEE Trans. Wireless Comm.*, vol. 8, no. 7, pp. 3646-3657, July 2009.
[22] J. Maurer, T. Fugen, T. Schafer, W. Wiesbeck, "A New Inter-Vehicle Communications (IVC) Channel Model," *Proc. IEEE Veh. Tech. Conf.*, vol. 1, pp. 9-13, September 2004.
[23] D. W. Matolak, "Radio Channel Modeling for Vehicle-to-Vehicle/Road Communications," Chapter 2 in *Wireless Technologies for Intelligent Transportation Systems*, M-T Zhou, Y. Zhang, L. T. Yang, editors, Nova Science Publishers, March 2010.
[24] Editors of Scientific American, "The Spies Above Your Backyard," *Scientific American*, pp. 12, April 2013.
[25] J. Horgan, "The Drones Come Home," *National Geographic*, pp. 122-133, March 2013.

[26] F. Besse, F. Garcia, A. Pirovano, "Wireless Ad Hoc Networks Access for Aeronautical Communications," *Proc. 28th AIAA Int. Communications Satellite Systems Conf.*, Anaheim, CA, 30 August-2 September 2010.
[27] F. Besse, A. Pirovano, F. Garcia, J. Radzik, "Interference Estimation in an Aeronautical Ad Hoc Network," *Proc. 30th DASC*, Seattle, WA, 16-20 October 2011.
[28] N. Neji, R. deLacerda, A. Azoulay, T. Letertre, O. Outtier, "Survey on the Future Aeronautical Communication System and Its Development for Continental Communications," *IEEE Trans. Vehicular Tech*., vol. 62, no. 1, pp. 182-191, January 2013.
[29] A. I. Alshbatat, L. Dong, "Performance Analysis of Mobile Ad Hoc Unmanned Aerial Vehicle Communication Networks with Directional Antennas," *International Journal of Aerospace Engineering*, vol. 2010, Article ID 874586, 2010.
[30] M. Simunek, P. Pechac, F. P. Fontan, "Feasibility of UAV Link Space Diversity in Wooded Areas," *International Journal of Antennas and Propagation*, vol. 2013, Article ID 890629, 2013.
[31] Y. Cai, F. R. Yu, J. Li, Y. Zhou, L. Lamont, "Medium Access Control for Unmanned Aerial Vehicle (UAV) Ad-Hoc Networks with Full-Duplex Radios and Multipacket Reception Capability," *IEEE Trans. Vehicular Tech*., vol. 62, no. 1, pp. 390-394, January 2013.
[32] E. T. Michailidis, P. Theofilakos, A. G. Kanatas, "Three-Dimensional Modeling and Simulation of MIMO Mobile-to-Mobile via Stratospheric Relay Channels," *IEEE Trans. Vehicular Tech*., vol. 62, no. 5, pp. 2014-2030, June 2013.
[33] M. J. Gans, K. M. Borle, B. Chen, T. Freeland, D. McCarthy, "Enhancing Connectivity of Unmanned Vehicles Through MIMO Communications," *Proc. IEEE Fall Vehicular Tech. Conf.*, Las Vegas, NV, 2-5 September 2013.
[34] S. Plass, M. Berioli, R. Hermenier, G. Liva, A. Munari, "Machine-to-Machine Communications via Airliners," Trans. Emerging Telecommunications Tech., vol. 24, DOI:10.1002/ett.2615, pp. 427-440, January 2013.
[35] K. Wesson, T. Humphreys, "Hacking Drones," *Scientific American*, pp. 54-59, November 2013.
[36] M. Simunek, F. P. Fontan, P. Pechac, "The UAV Low Elevation Angle Propagation Channel in Urban Areas: Statistical Analysis and Time-Series Generator," *IEEE Trans. Antennas & Prop*., vol. 61, no. 7, pp. 3850-3858, July 2013.
[37] C. Loo, A Statistical Model for a Land Mobile Satellite Link," *IEEE Trans. Veh. Tech*., vol. VT-34, no. 3, pp. 122-127, August 1985.

Appendix A: Results from Additional Flight Tracks

This appendix contains path loss, delay spread, and correlation results for the remaining flight tracks not described in the main body of the report. Most of the results are presented without discussion because of their similarity to those for FT1, FT2, FT4 and FT10. A few observations on interesting or atypical results are noted. In Table A.1 we list the shape and range of distances for these FTs.

Table A1. FT shapes and distances for remaining FTs.

FT#	FT Shape	Approximate Distance (km)	Comments
3	Straight, toward GS	18-50	—
5	Oval	18-27	max pitch angle 5.5°
6	Oval	19-27.5	—
7	Oval	16-28	min roll angle -27°
8	Straight, toward GS	1-26	—
9	Straight, away from GS	1-45	max pitch angle 6.5°
11	Oval	16-26.5	max pitch angle 7.1°
12	Oval	16-27	max pitch angle 7.1°

A.1 Flight Track 3

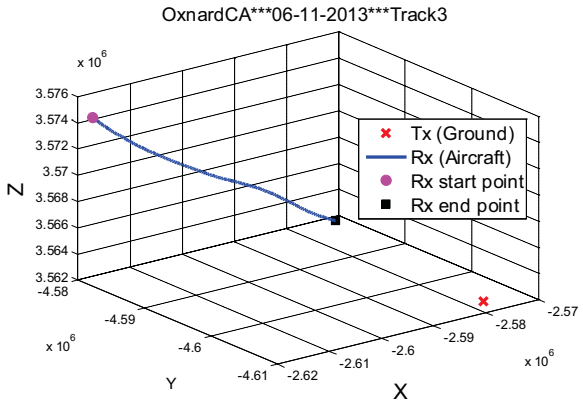

(a)

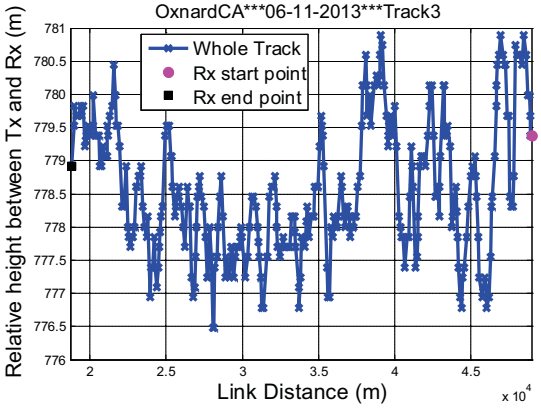

(b)

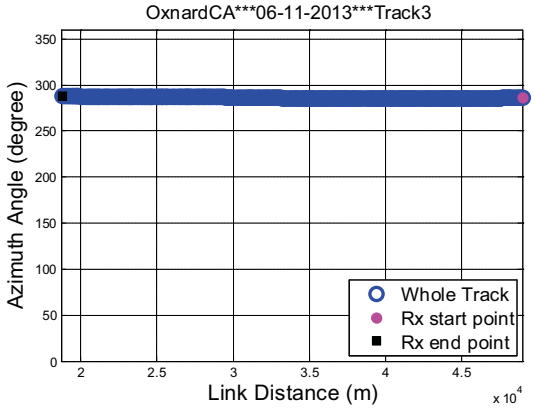

(c)

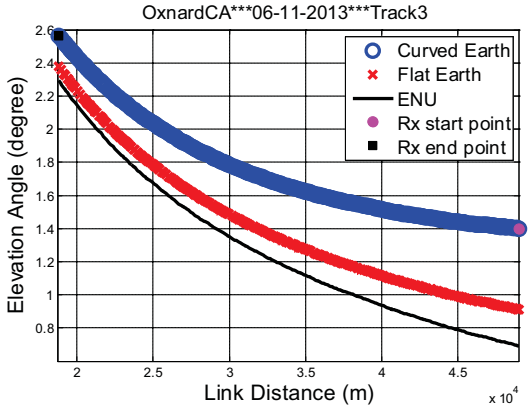

(d)

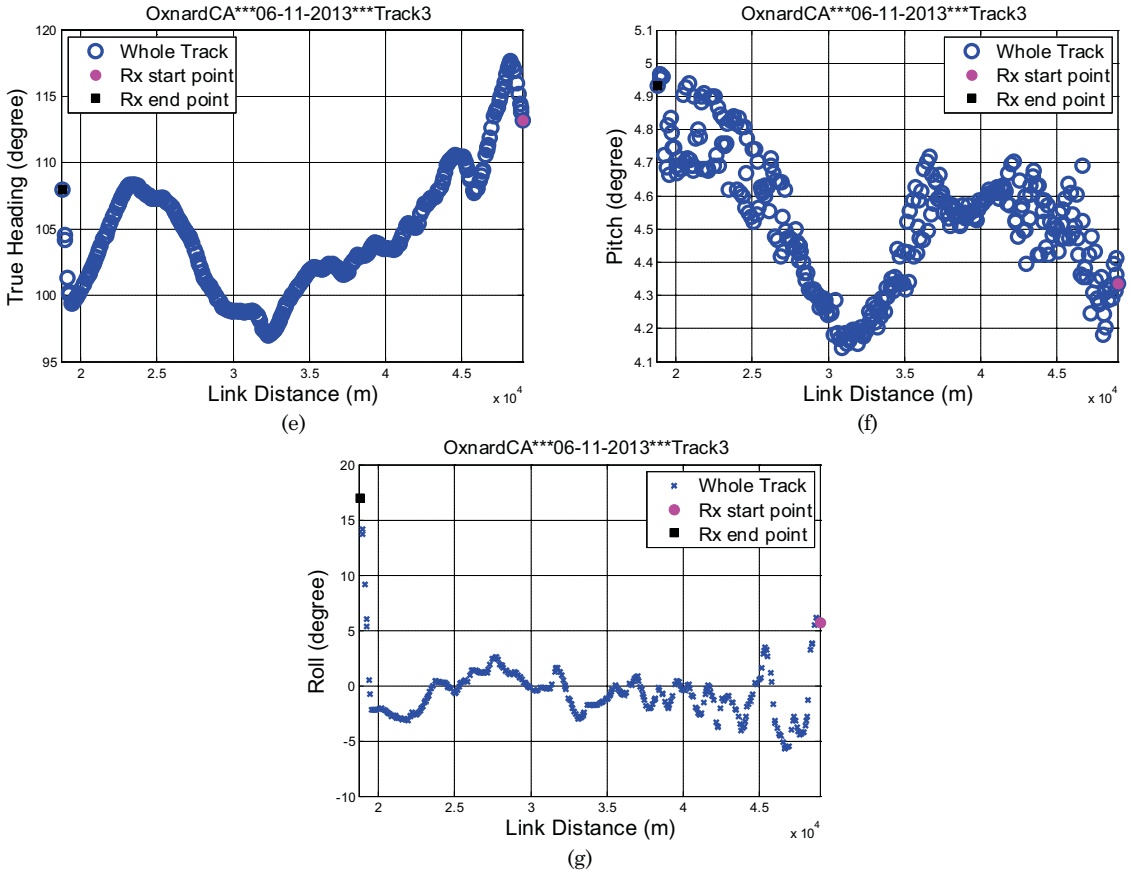

Figure A1. Geometric traces for FT3: (a) flight track in ECEF coordinates; (b) altitude difference between aircraft and ground station; (c) azimuth angle; (d) elevation angle; (e) heading of AC; (f) pitch angle of AC; (g) roll angle of AC.

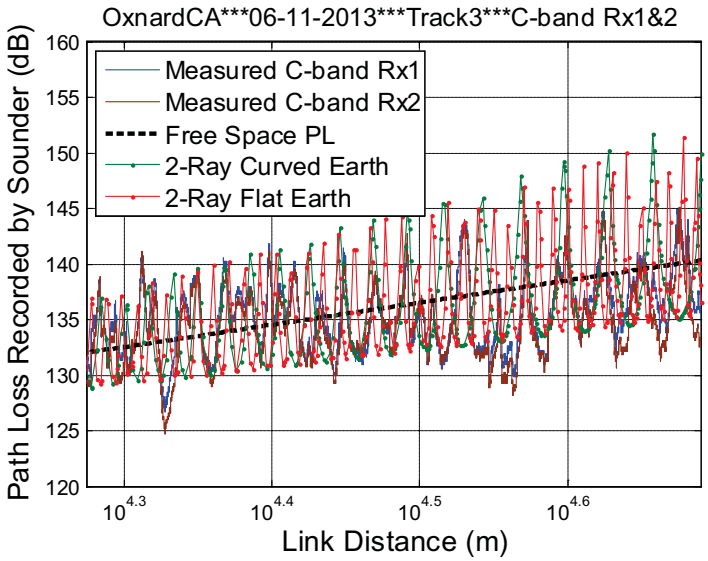

Figure A2. Measured path loss vs. distance for C-band Rx1 & 2, FT3.

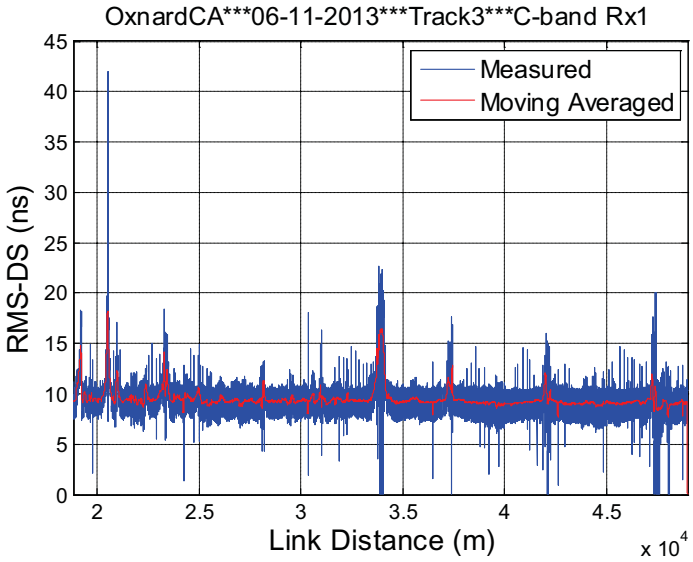

Figure A3. RMS-DS vs. distance for C-band Rx1, FT3.

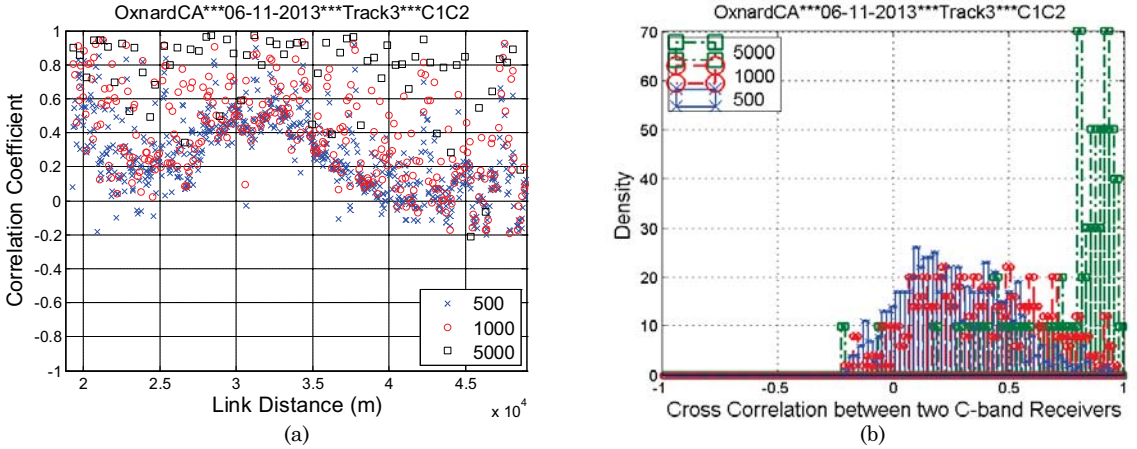

(a) (b)

Figure A4. Measured amplitude correlation coefficient between C-band Rx1 and 2 for FT3, for three different vector lengths: (a) correlation coefficient; (b) distributions of correlation coefficient.

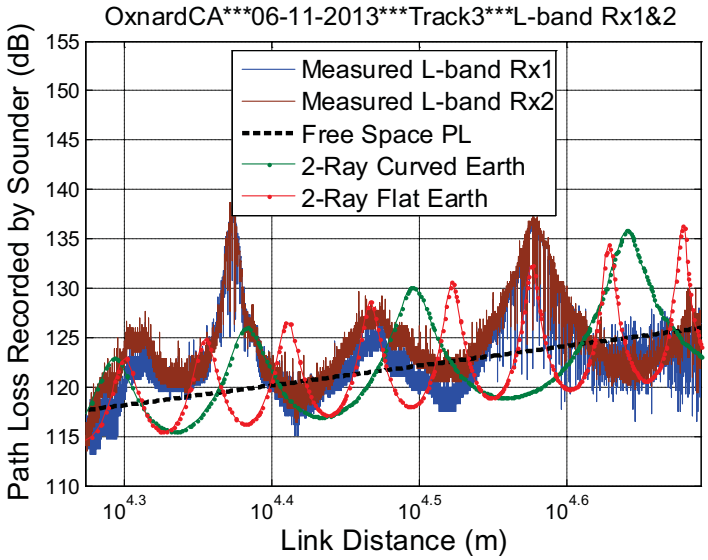

Figure A5. Path loss vs. distance for L-band Rx1 & 2 for FT3.

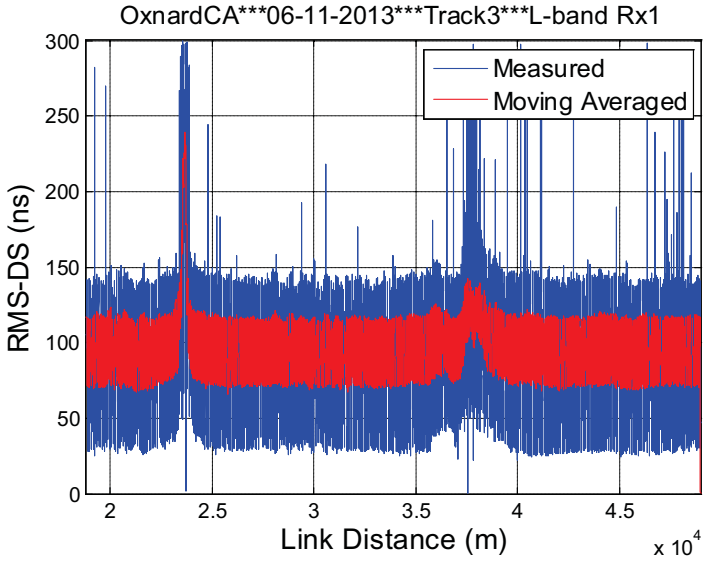

Figure A6. Measured RMS-DS vs. distance for L-band Rx1, FT3.

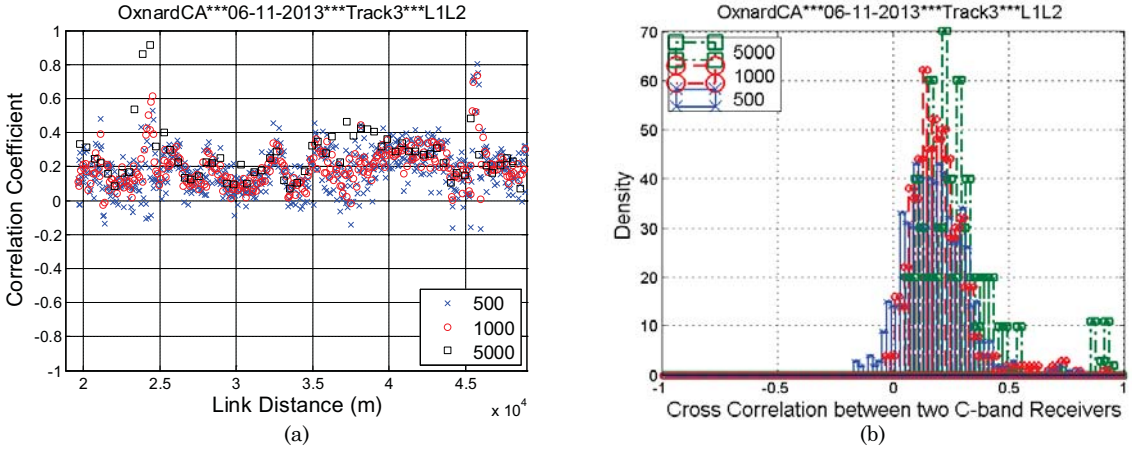

(a) (b)

Figure A7. Measured amplitude correlation coefficient between L-band Rx1 and 2 for FT3, for three different vector lengths: (a) correlation coefficient; (b) distributions of correlation coefficient.

Table A2. Statistics of Cross Correlation Coefficients for Oxnard, Flight Track 3.

	C1C2			L1L2			C1L1	C1L2	C2L1	C2L2
Vector Length	500	1000	5000	500	1000	5000	1000	1000	1000	1000
Mean	0.27	0.39	0.75	0.18	0.20	0.28	0.00	0.00	0.00	0.00
Median	0.24	0.38	0.84	0.18	0.18	0.25	0.00	0.01	-0.01	-0.01
Max	0.93	0.96	0.97	0.80	0.80	0.91	0.34	0.33	0.28	0.37
Min	-0.20	-0.19	-0.21	-0.17	-0.03	0.07	-0.43	-0.45	-0.58	-0.43
Standard deviation	0.23	0.27	0.25	0.13	0.12	0.17	0.09	0.10	0.10	0.10

A.2 Flight Track 5

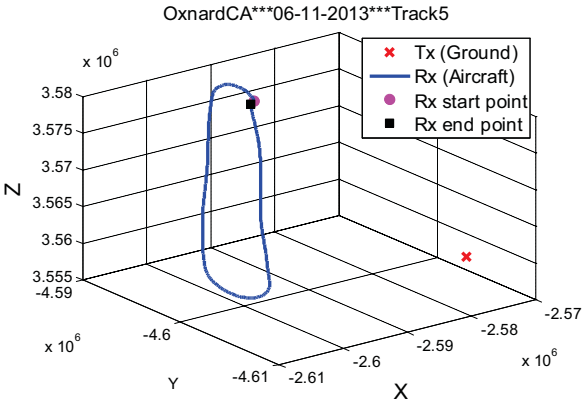

(a)

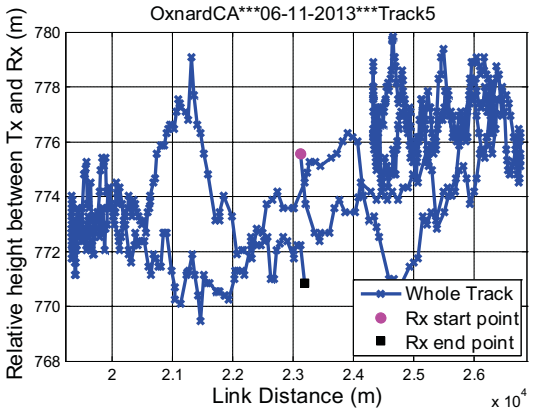

(b)

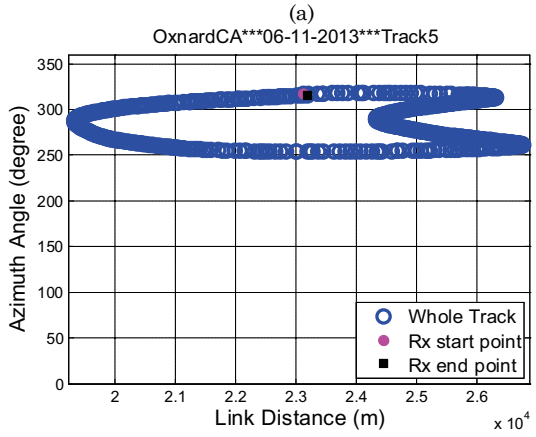

(c)

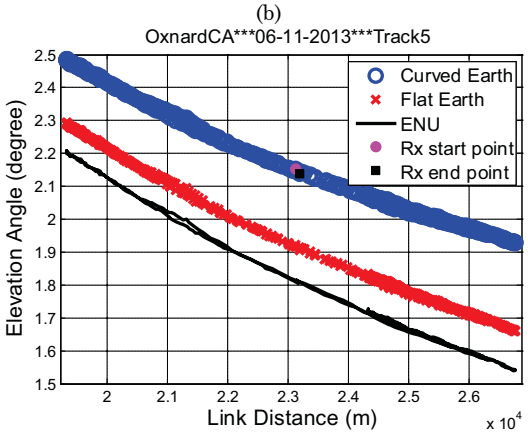

(d)

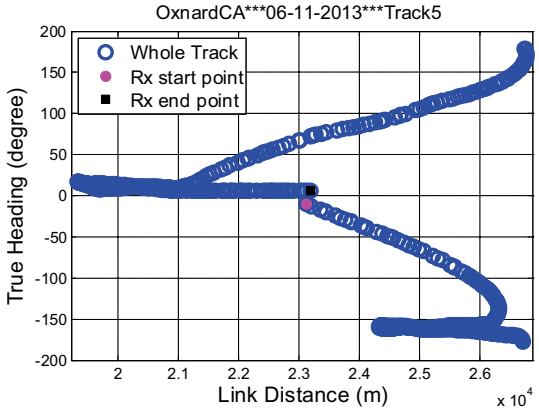

(e)

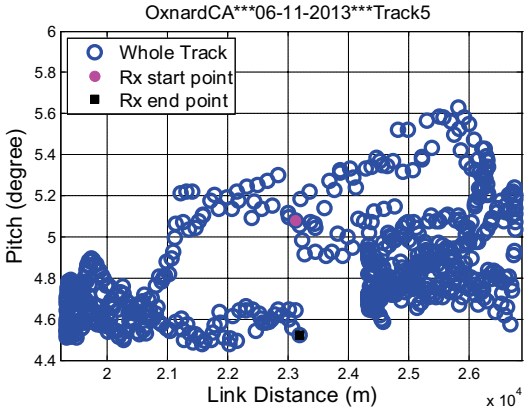

(f)

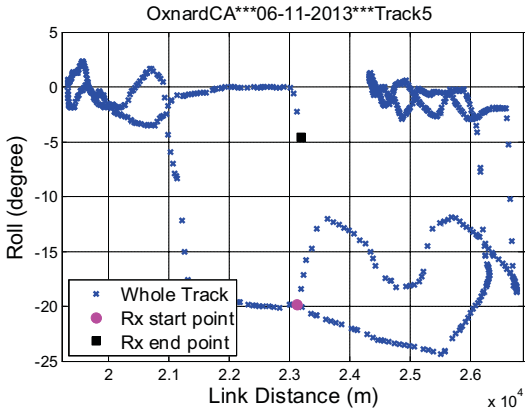

(g)

Figure A8. Geometric traces for FT5: (a) flight track in ECEF coordinates; (b) altitude difference between aircraft and ground station; (c) azimuth angle; (d) elevation angle; (e) heading of AC; (f) pitch angle of AC; (g) roll angle of AC.

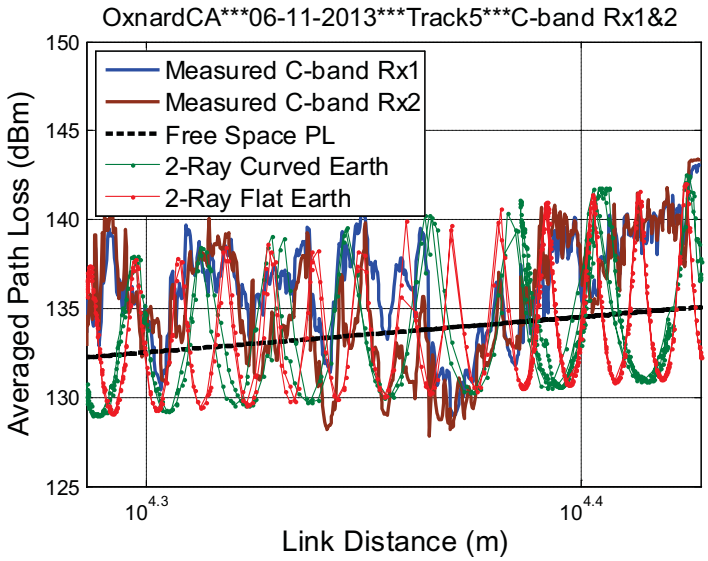

Figure A9. Measured path loss vs. distance for C-band Rx1 & 2, FT5.

In Figure A10 we show RMS-DS vs. distance for FT5, C-band Rx1. The very large "spikes" at link distances of approximately 22.4 km and 25.4 km are anomalous, and will be removed in future processing. These spikes are attributable to noise, which can be confirmed from the large path loss values at the corresponding distances in Figure A9.

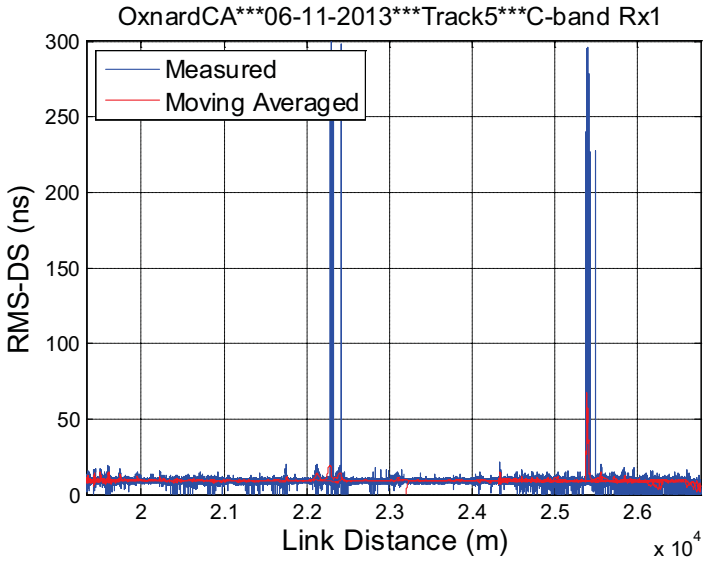

Figure A10. RMS-DS vs. distance for C-band Rx1, FT5.

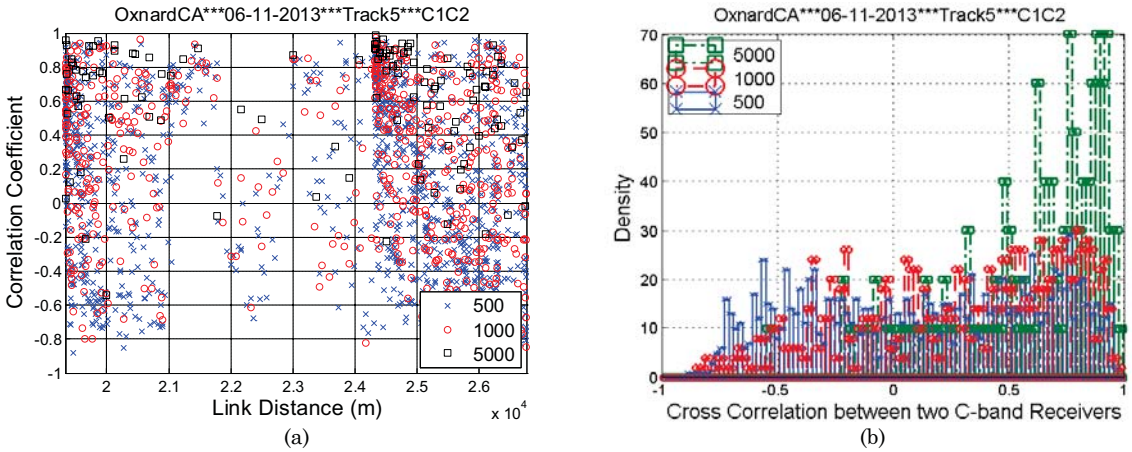

(a) (b)

Figure A11. Measured amplitude correlation coefficient between C-band Rx1 and 2 for FT5, for three different vector lengths: (a) correlation coefficient; (b) distributions of correlation coefficient.

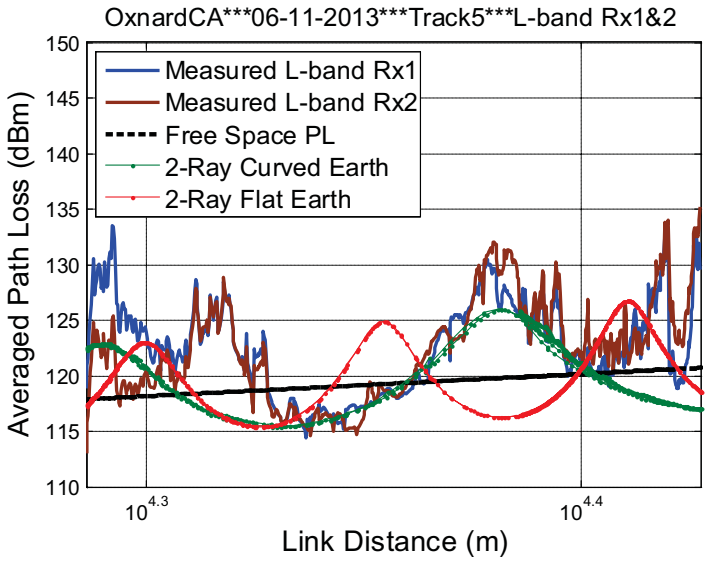

Figure A12. Path loss vs. distance for L-band Rx1 & 2 for FT5.

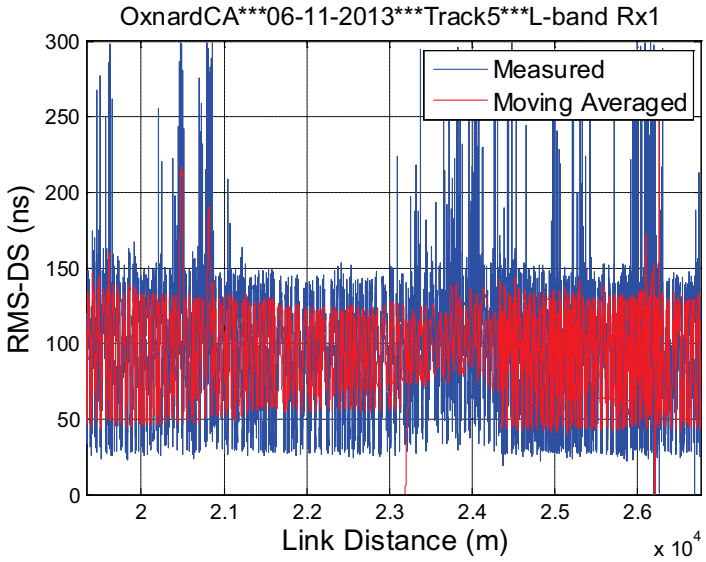

Figure A13. Measured RMS-DS vs. distance for L-band Rx1, FT5.

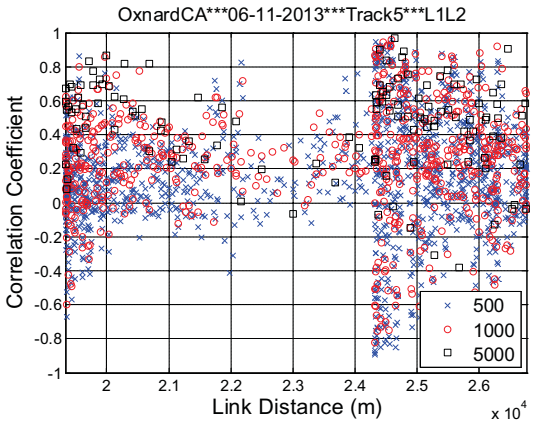

(a)

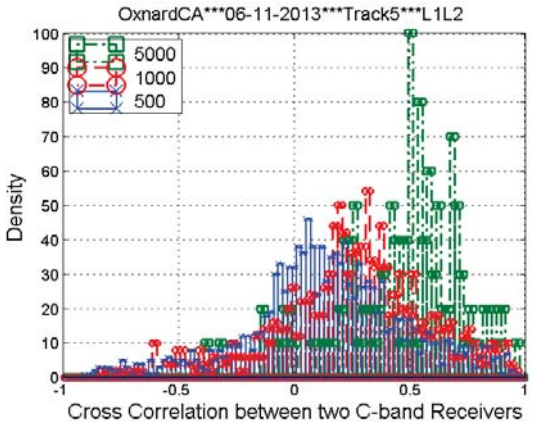

(b)

Figure A14. Measured amplitude correlation coefficient between L-band Rx1 and 2 for FT5, for three different vector lengths: (a) correlation coefficient; (b) distributions of correlation coefficient.

Table A3. Statistics of Cross Correlation Coefficients for Oxnard, Flight Track 5.

	C1C2			L1L2			C1L1	C1L2	C2L1	C2L2
Vector Length	500	1000	5000	500	1000	5000	1000	1000	1000	1000
Mean	0.14	0.28	0.61	0.14	0.25	0.47	0.00	0.01	-0.01	-0.01
Median	0.17	0.37	0.71	0.14	0.27	0.51	0.00	0.01	-0.01	0.00
Max	0.96	0.97	0.99	0.96	0.96	0.97	0.84	0.85	0.80	0.74
Min	-0.88	-0.85	-0.54	-0.90	-0.82	-0.38	-0.90	-0.80	-0.85	-0.83
Standard deviation	0.50	0.46	0.32	0.34	0.32	0.26	0.27	0.27	0.27	0.28

A.3 Flight Track 6

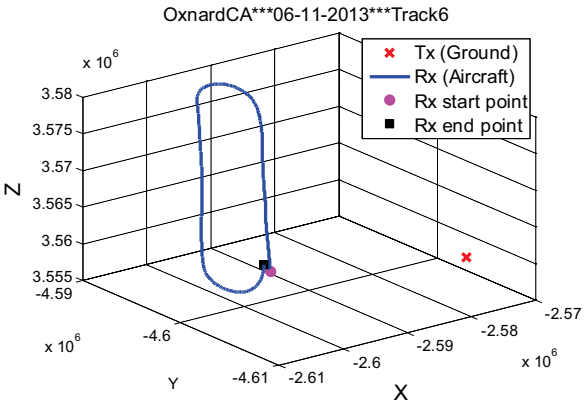

(a)

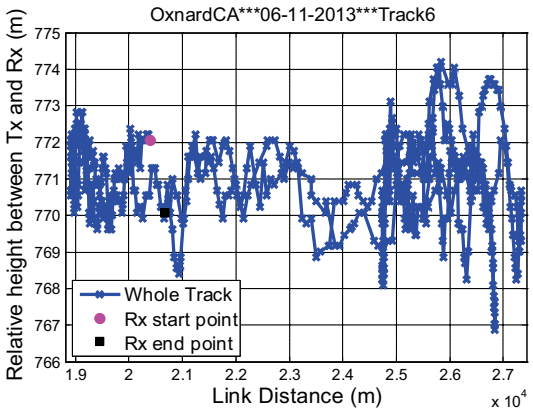

(b)

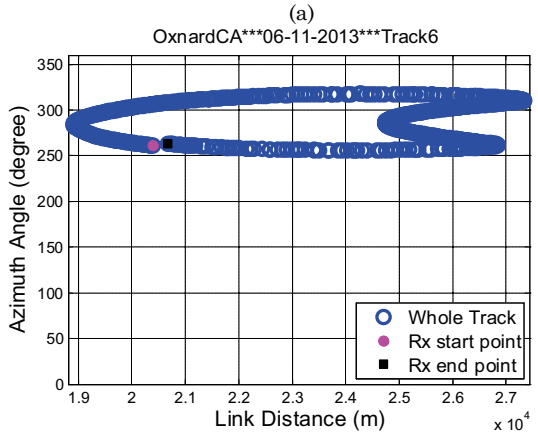

(c)

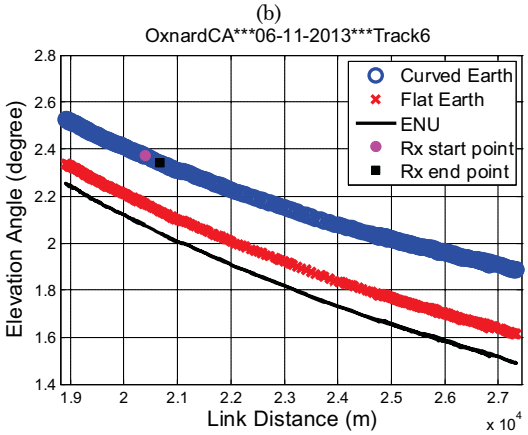

(d)

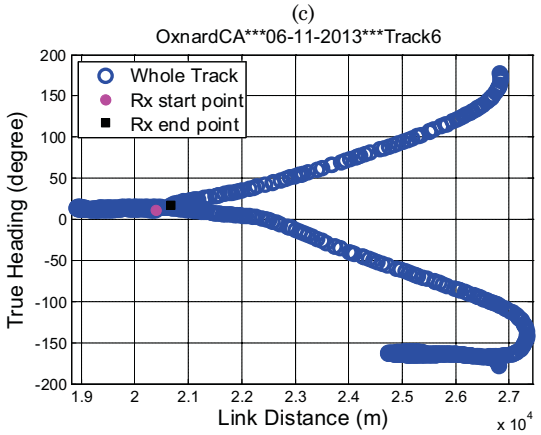

(e)

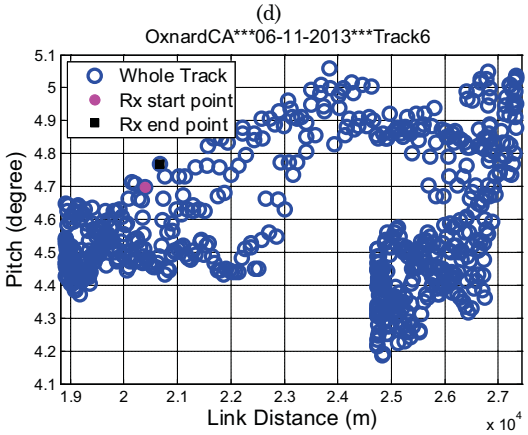

(f)

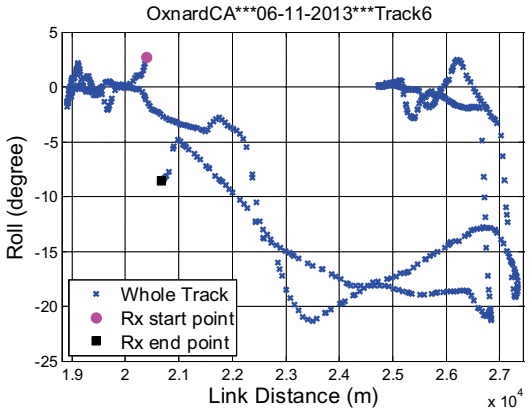

(g)

Figure A15. Geometric traces for FT6: (a) flight track in ECEF coordinates; (b) altitude difference between aircraft and ground station; (c) azimuth angle; (d) elevation angle; (e) heading of AC; (f) pitch angle of AC; (g) roll angle of AC.

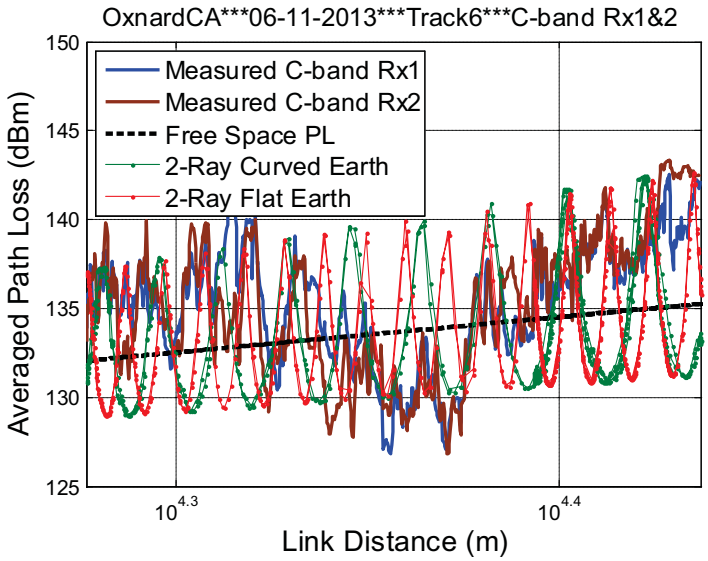

Figure A16. Measured path loss vs. distance for C-band Rx1 & 2, FT6.

Figure A17 also shows some anomalously large RMS-DS values for the C-band Rx1, again due to large path loss values. Subsequent processing will remove these to more accurately reflect the actual RMS-DS statistics.

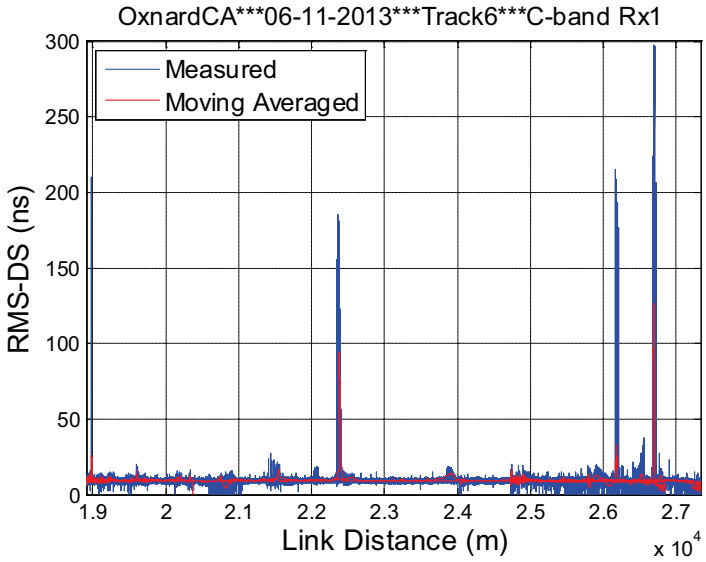

Figure A17. RMS-DS vs. distance for C-band Rx1, FT6.

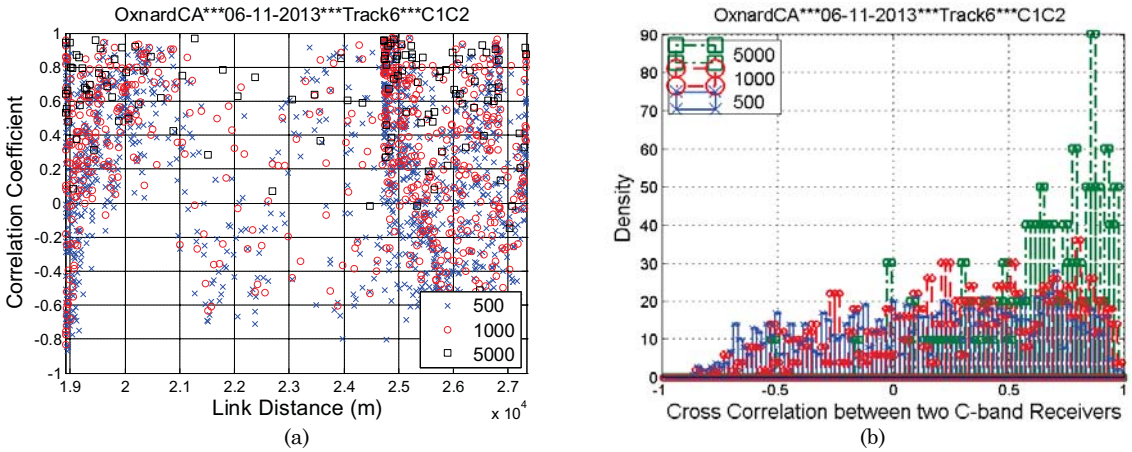

(a) (b)

Figure A18. Measured amplitude correlation coefficient between C-band Rx1 and 2 for FT6, for three different vector lengths: (a) correlation coefficient; (b) distributions of correlation coefficient.

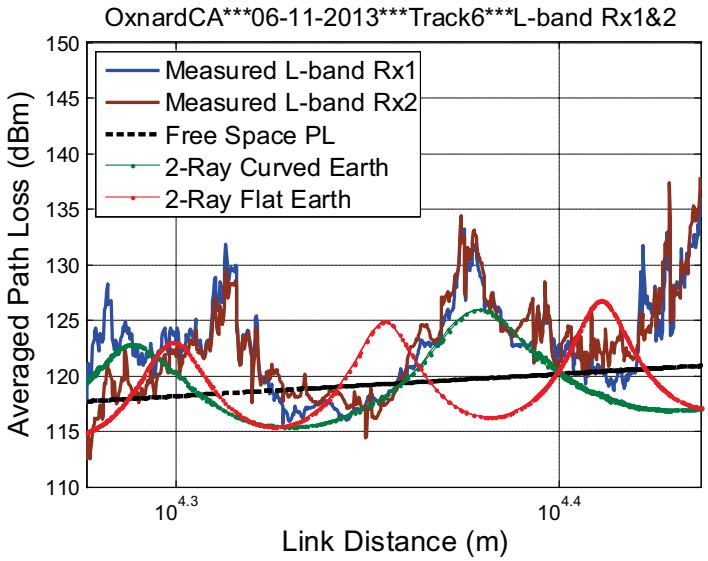

Figure A19. Path loss vs. distance for L-band Rx1 & 2 for FT6.

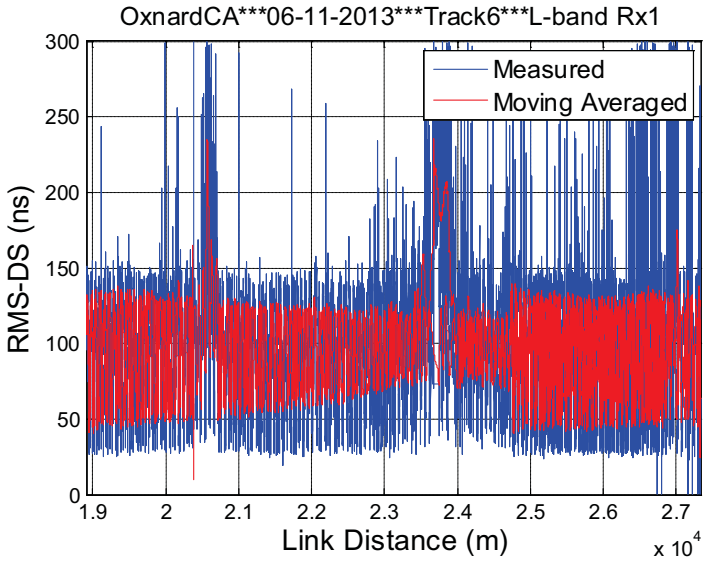

Figure A20. Measured RMS-DS vs. distance for L-band Rx1, FT6.

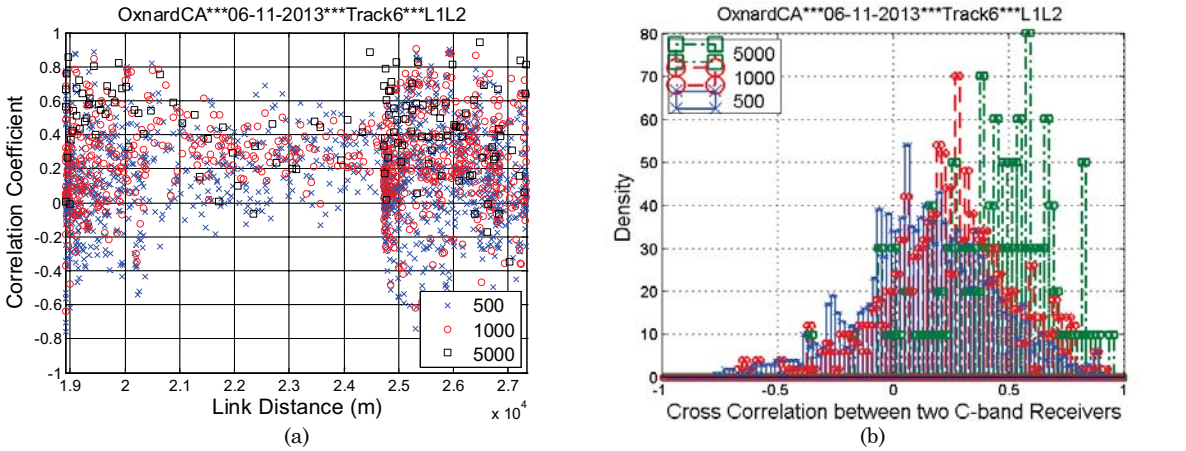

(a) (b)

Figure A21. Measured amplitude correlation coefficient between L-band Rx1 and 2 for FT6, for three different vector lengths: (a) correlation coefficient; (b) distributions of correlation coefficient.

Table A4. Statistics of Cross Correlation Coefficients for Oxnard, Flight Track 6.

	C1C2			L1L2			C1L1	C1L2	C2L1	C2L2
Vector Length	500	1000	5000	500	1000	5000	1000	1000	1000	1000
Mean	0.17	0.30	0.63	0.14	0.24	0.44	0.01	0.02	0.00	0.01
Median	0.22	0.36	0.68	0.14	0.24	0.47	0.01	0.01	0.00	0.01
Max	0.97	0.97	0.97	0.89	0.91	0.94	0.79	0.75	0.76	0.86
Min	-0.87	-0.83	-0.51	-0.76	-0.65	-0.35	-0.68	-0.72	-0.74	-0.84
Standard deviation	0.47	0.44	0.28	0.28	0.27	0.25	0.26	0.26	0.28	0.27

A.4 Flight Track 7

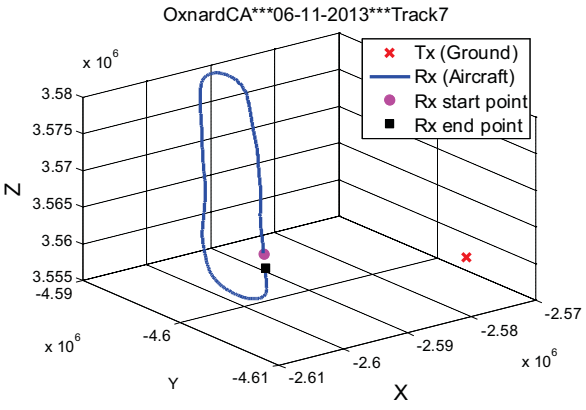

(a)

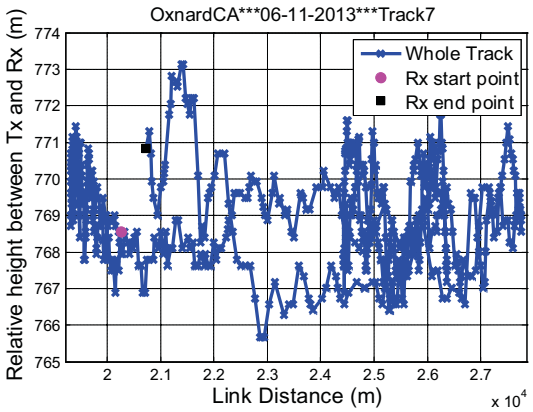

(b)

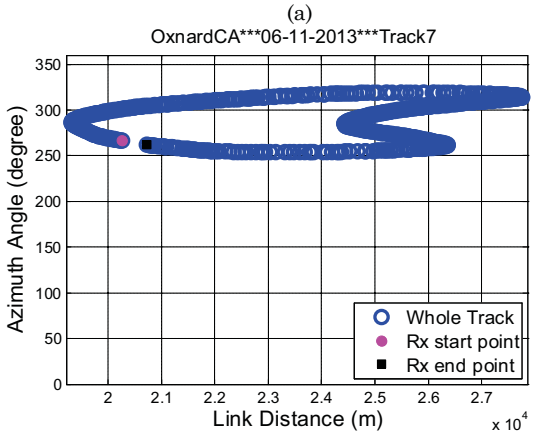

(c)

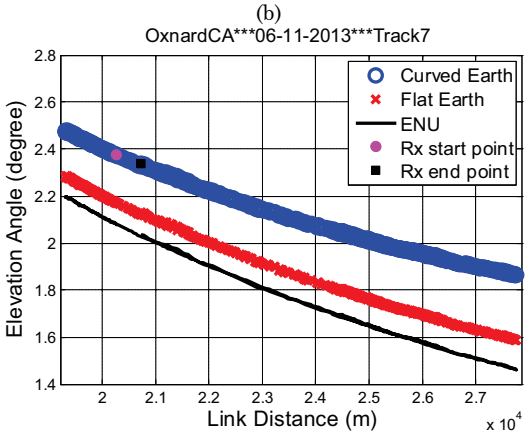

(d)

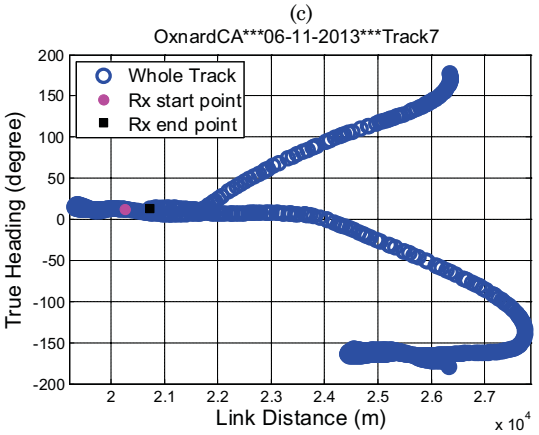

(e)

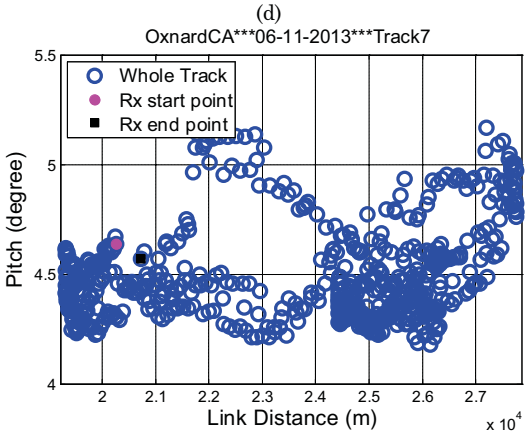

(f)

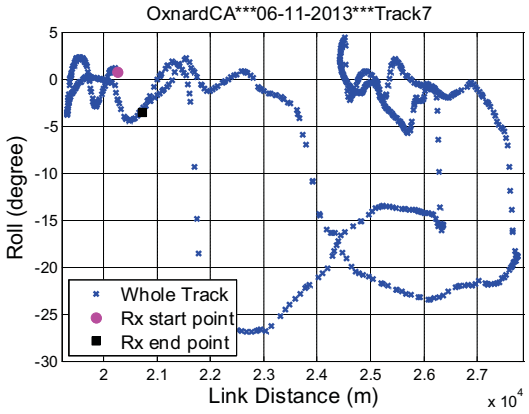

(g)

Figure A22. Geometric traces for FT7: (a) flight track in ECEF coordinates; (b) altitude difference between aircraft and ground station; (c) azimuth angle; (d) elevation angle; (e) heading of AC; (f) pitch angle of AC; (g) roll angle of AC.

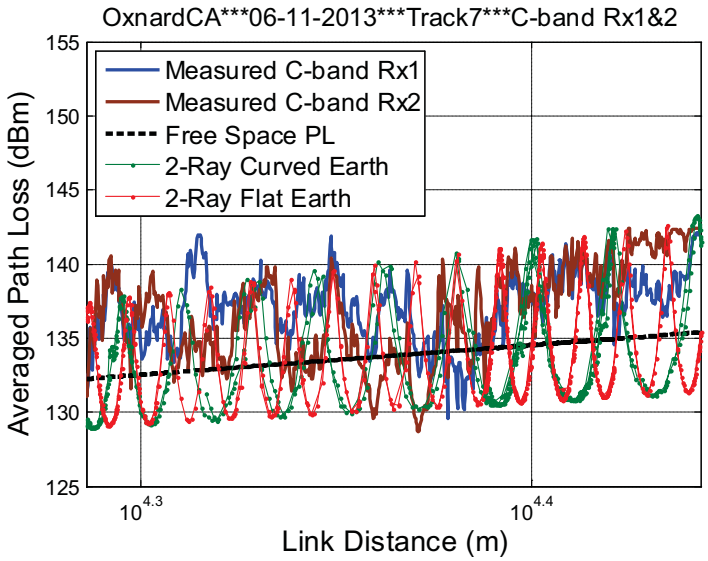

Figure A23. Measured path loss vs. distance for C-band Rx1 & 2, FT7.

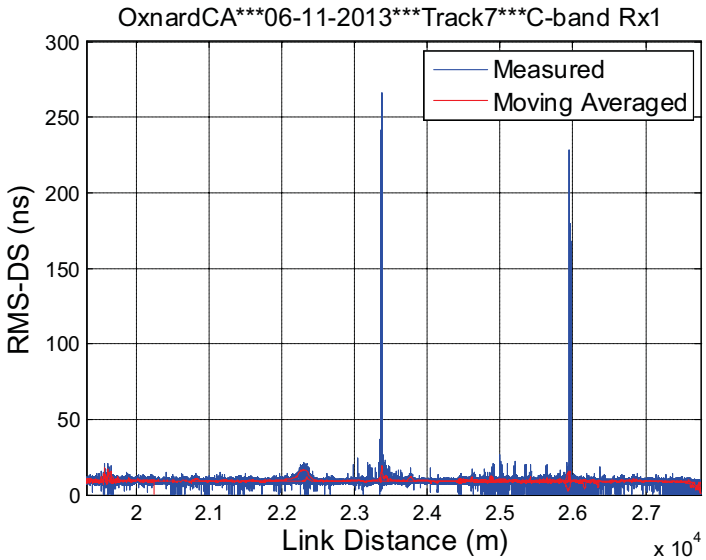

Figure A24. RMS-DS vs. distance for C-band Rx1, FT7.

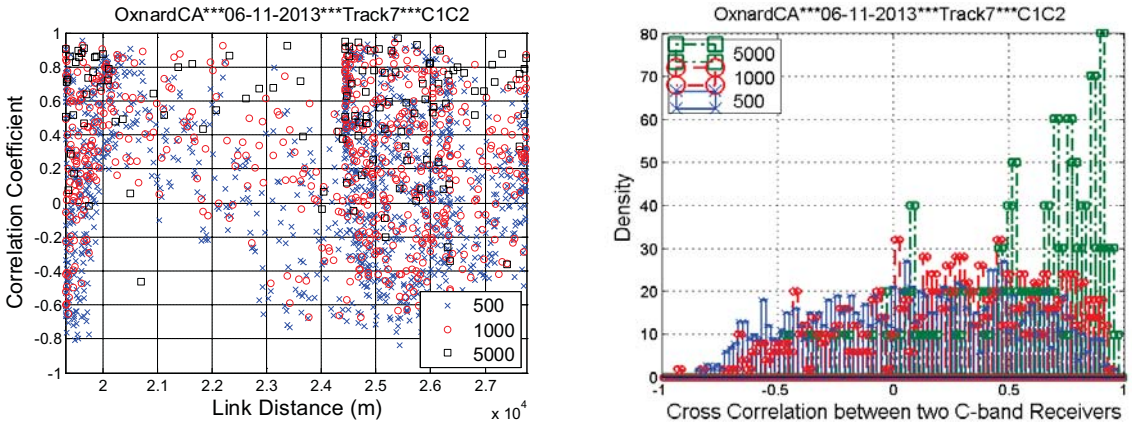

(a) (b)

Figure A25. Measured amplitude correlation coefficient between C-band Rx1 and 2 for FT7, for three different vector lengths: (a) correlation coefficient; (b) distributions of correlation coefficient.

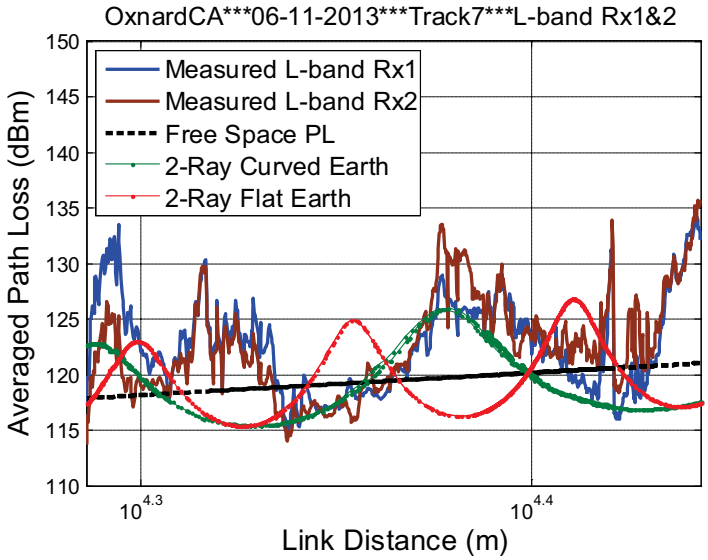

Figure A26. Path loss vs. distance for L-band Rx1 & 2 for FT7.

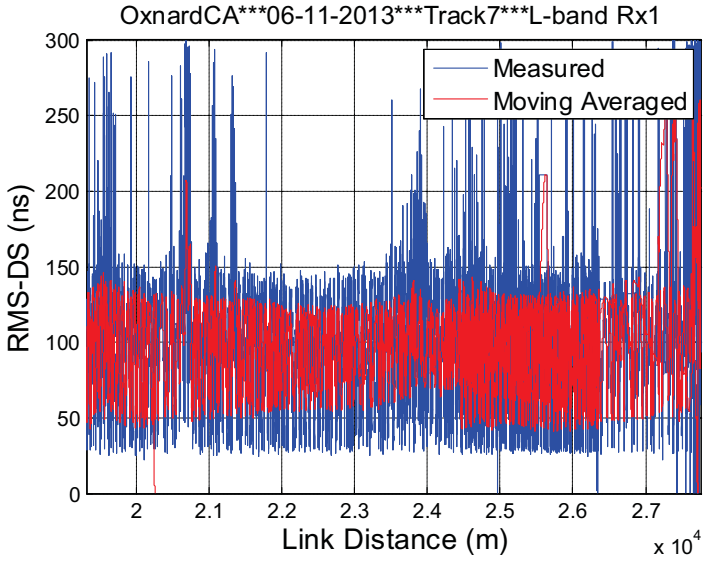

Figure A27. Measured RMS-DS vs. distance for L-band Rx1, FT7.

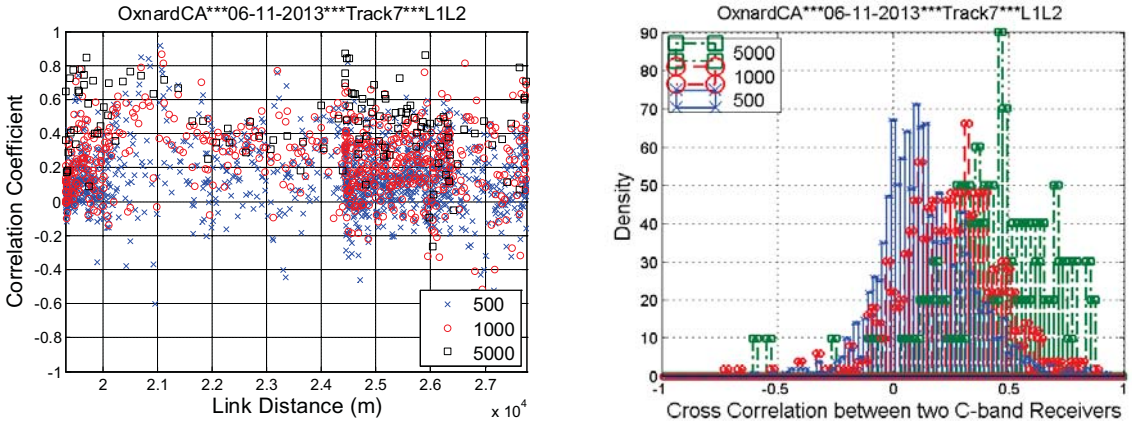

Figure A28. Measured amplitude correlation coefficient between L-band Rx1 and 2 for FT7, for three different vector lengths: (a) correlation coefficient; (b) distributions of correlation coefficient.

Table A5. Statistics of Cross Correlation Coefficients for Oxnard, Flight Track 7.

	C1C2			L1L2			C1L1	C1L2	C2L1	C2L2
Vector Length	500	1000	5000	500	1000	5000	1000	1000	1000	1000
Mean	0.10	0.24	0.55	0.14	0.24	0.45	-0.01	0.01	0.01	0.00
Median	0.12	0.28	0.64	0.12	0.25	0.47	0.00	0.01	0.00	0.00
Max	0.96	0.95	0.97	0.91	0.87	0.87	0.89	0.78	0.81	0.71
Min	-0.85	-0.92	-0.46	-0.60	-0.71	-0.59	-0.68	-0.72	-0.66	-0.70
Standard deviation	0.44	0.42	0.33	0.19	0.21	0.25	0.25	0.25	0.27	0.26

A.5 Flight Track 8

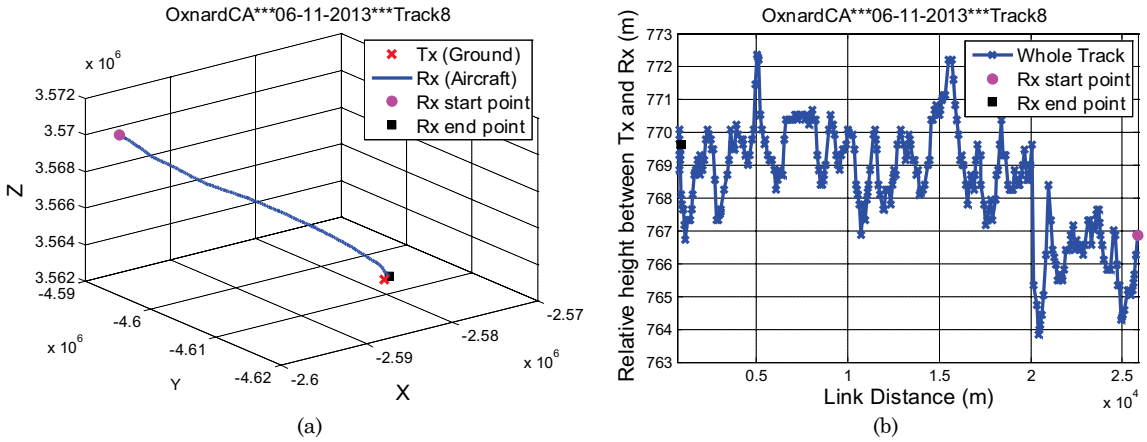

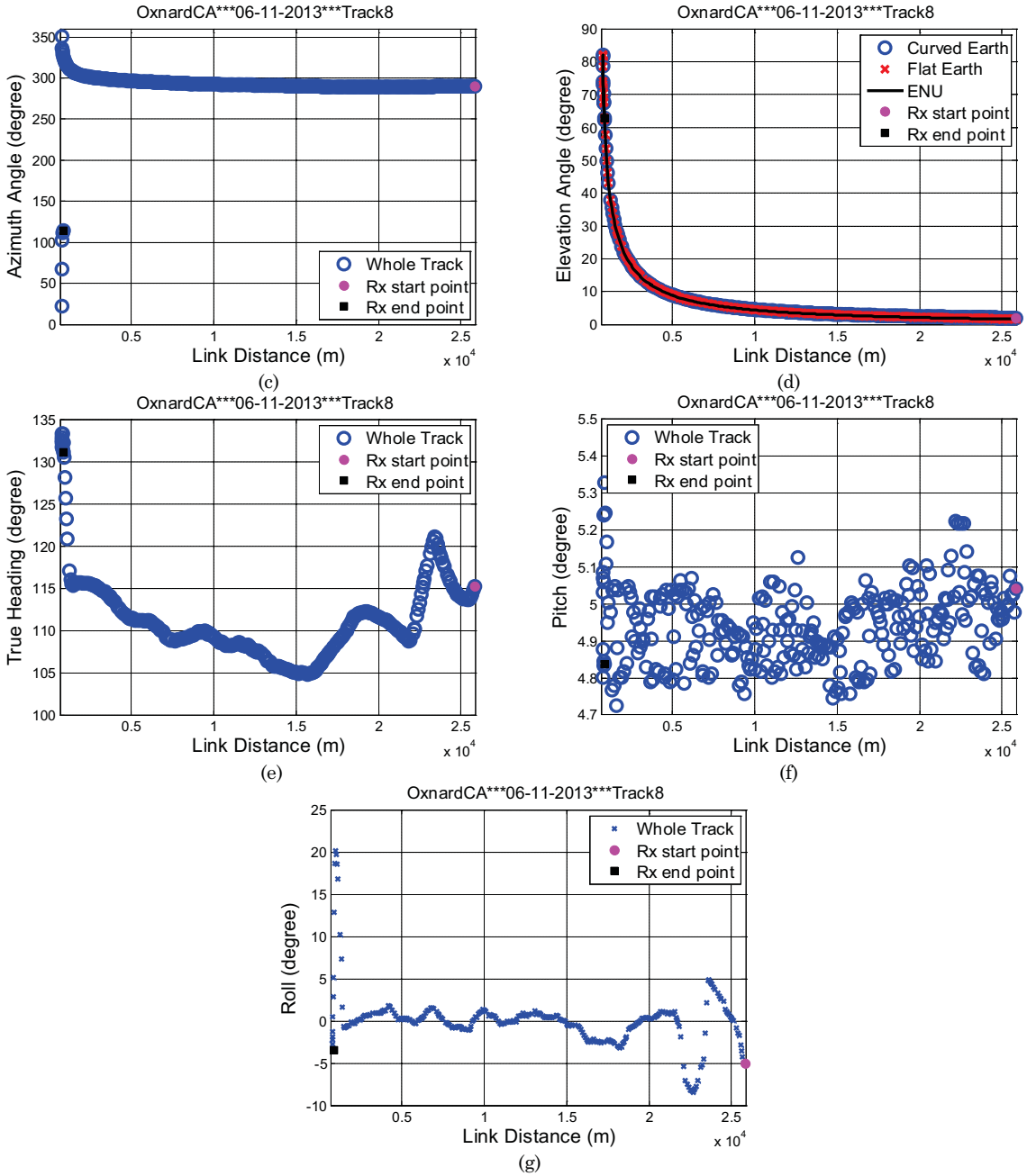

Figure A29. Geometric traces for FT8: (a) flight track in ECEF coordinates; (b) altitude difference between aircraft and ground station; (c) azimuth angle; (d) elevation angle; (e) heading of AC; (f) pitch angle of AC; (g) roll angle of AC.

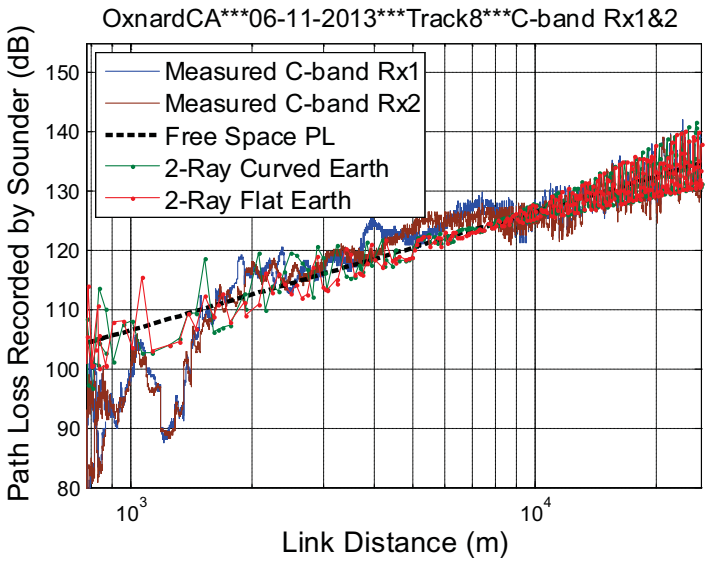

Figure A30. Measured path loss vs. distance for C-band Rx1 & 2, FT8.

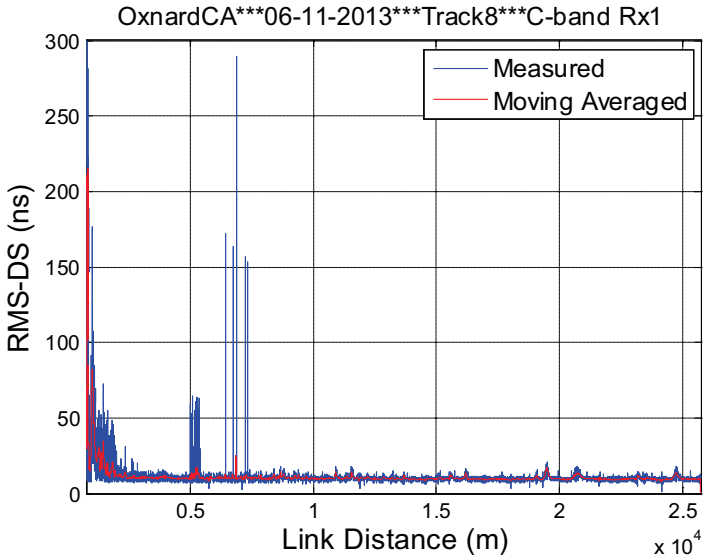

Figure A31. RMS-DS vs. distance for C-band Rx1, FT8.

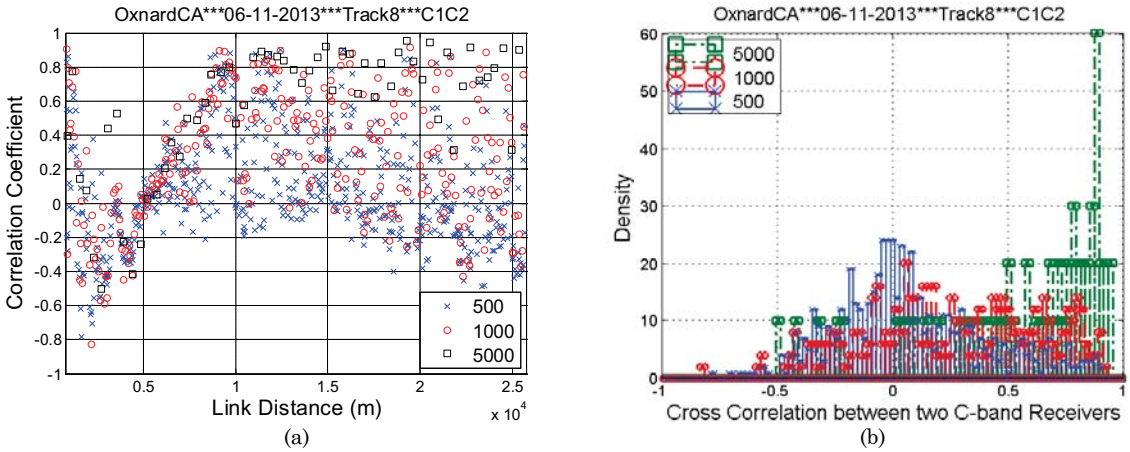

Figure A32. Measured amplitude correlation coefficient between C-band Rx1 and 2 for FT8, for three different vector lengths: (a) correlation coefficient; (b) distributions of correlation coefficient.

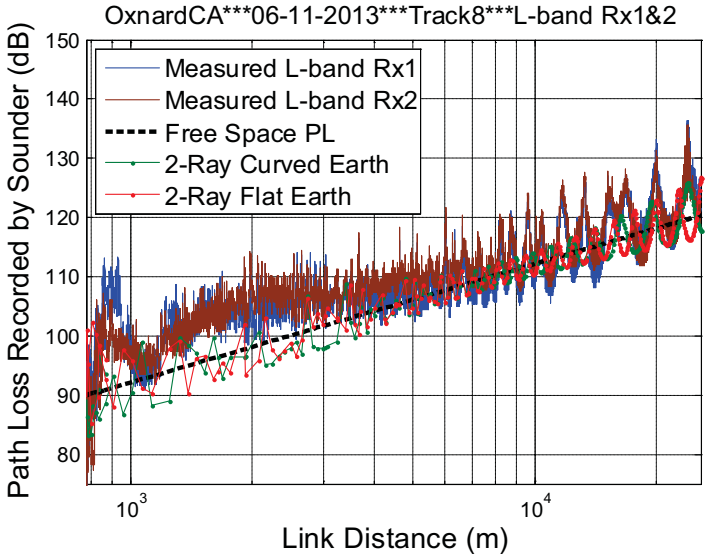

Figure A33. Path loss vs. distance for L-band Rx1 & 2 for FT8.

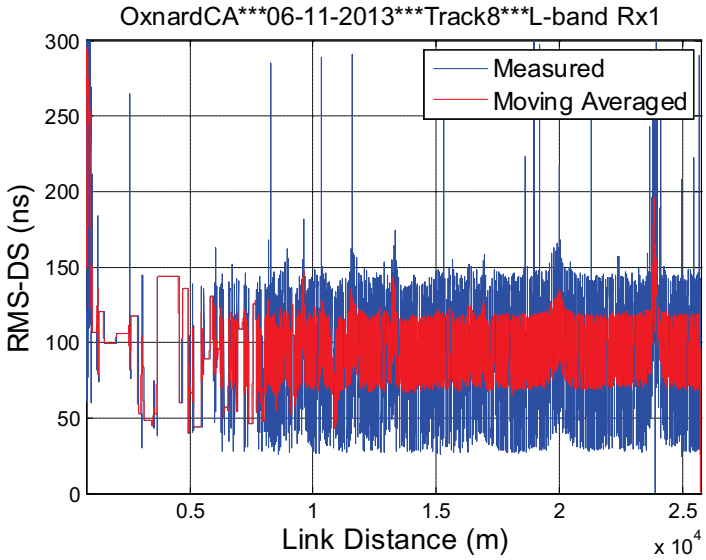

Figure A34. Measured RMS-DS vs. distance for L-band Rx1, FT8.

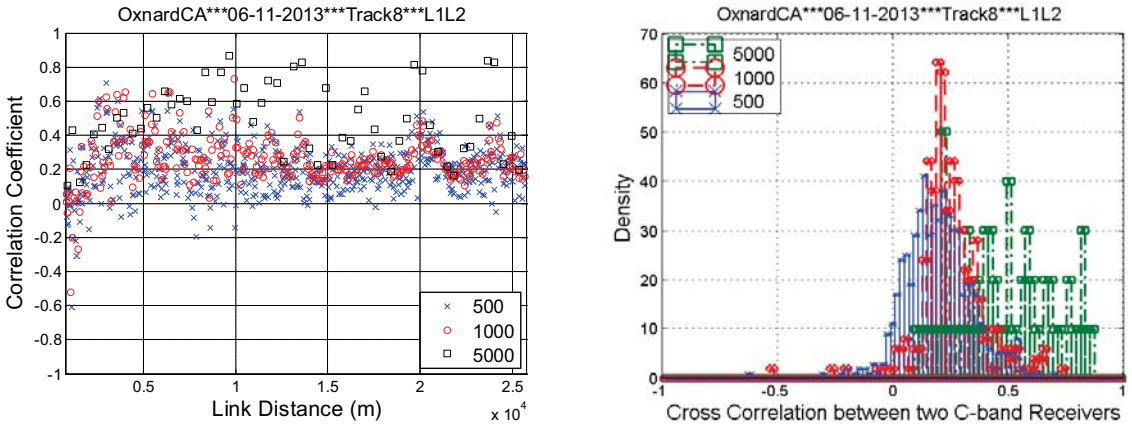

(a) (b)

Figure A35. Measured amplitude correlation coefficient between L-band Rx1 and 2 for FT8, for three different vector lengths: (a) correlation coefficient; (b) distributions of correlation coefficient.

Table A6. Statistics of Cross Correlation Coefficients for Oxnard, Flight Track 8.

	C1C2			L1L2			C1L1	C1L2	C2L1	C2L2
Vector Length	500	1000	5000	500	1000	5000	1000	1000	1000	1000
Mean	0.08	0.26	0.57	0.20	0.25	0.48	0.00	0.00	-0.01	-0.01
Median	0.03	0.27	0.71	0.19	0.23	0.47	0.00	0.01	-0.02	-0.01
Max	0.90	0.92	0.95	0.70	0.73	0.87	0.63	0.66	0.77	0.73
Min	-0.78	-0.83	-0.50	-0.61	-0.52	0.11	-0.64	-0.54	-0.43	-0.79
Standard deviation	0.32	0.37	0.37	0.14	0.14	0.21	0.21	0.18	0.18	0.21

A.6 Flight Track 9

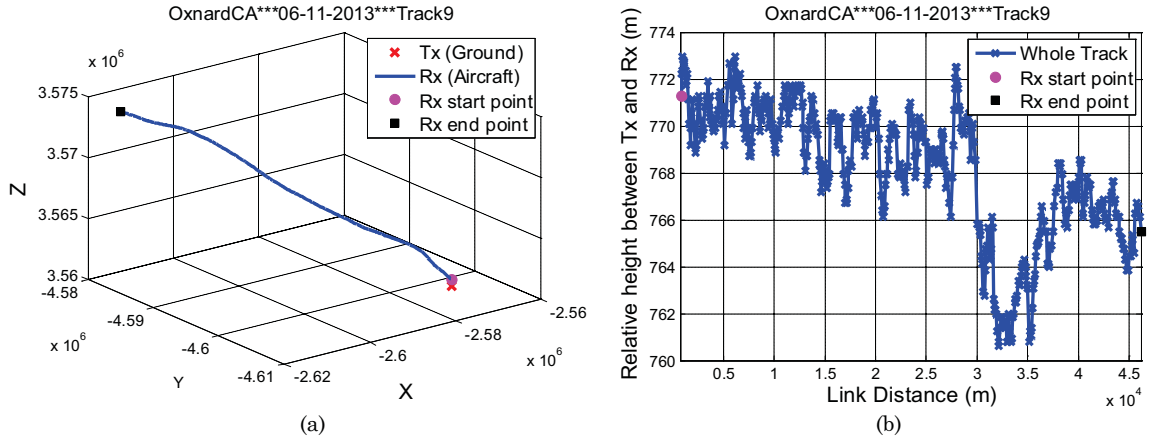

(a) (b)

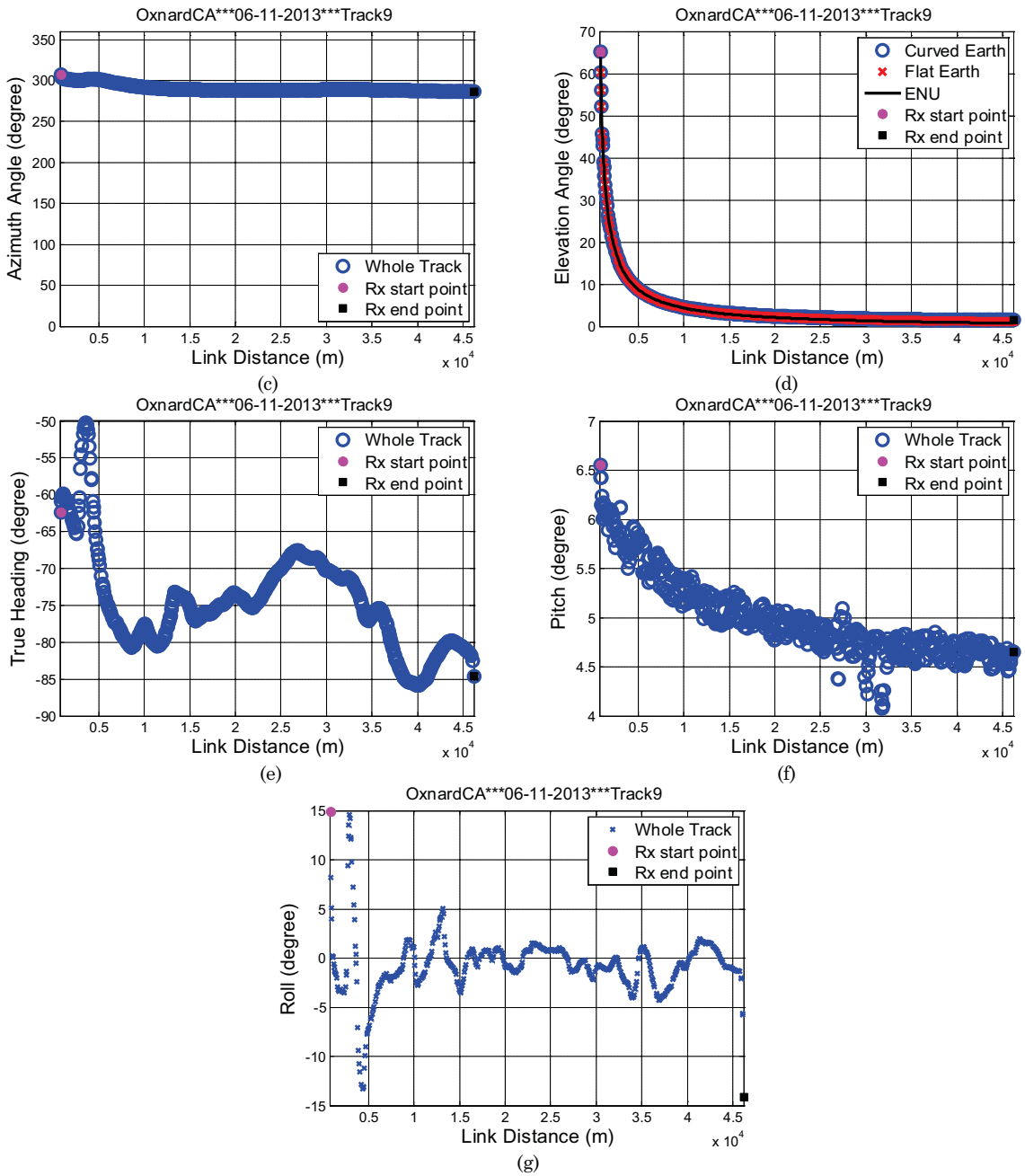

Figure A36. Geometric traces for FT9: (a) flight track in ECEF coordinates; (b) altitude difference between aircraft and ground station; (c) azimuth angle; (d) elevation angle; (e) heading of AC; (f) pitch angle of AC; (g) roll angle of AC.

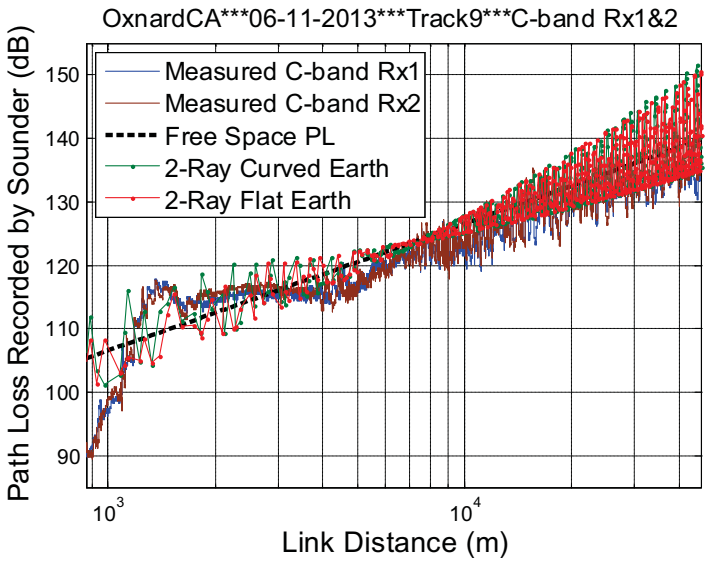

Figure A37. Measured path loss vs. distance for C-band Rx1 & 2, FT9.

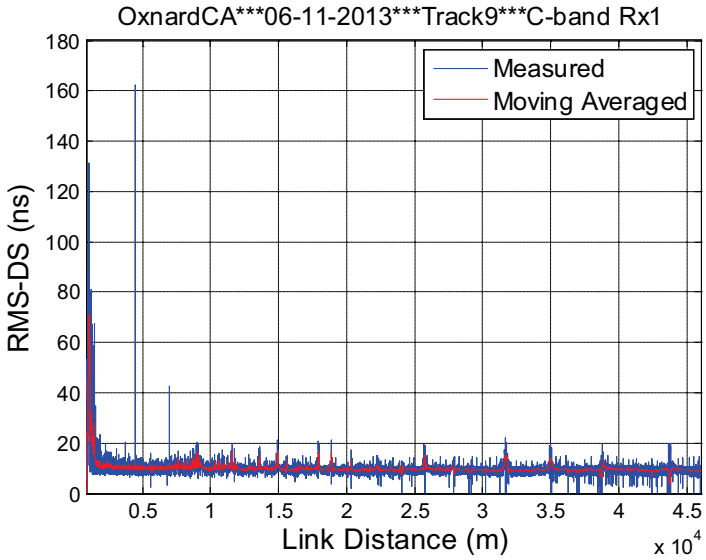

Figure A38. RMS-DS vs. distance for C-band Rx1, FT9.

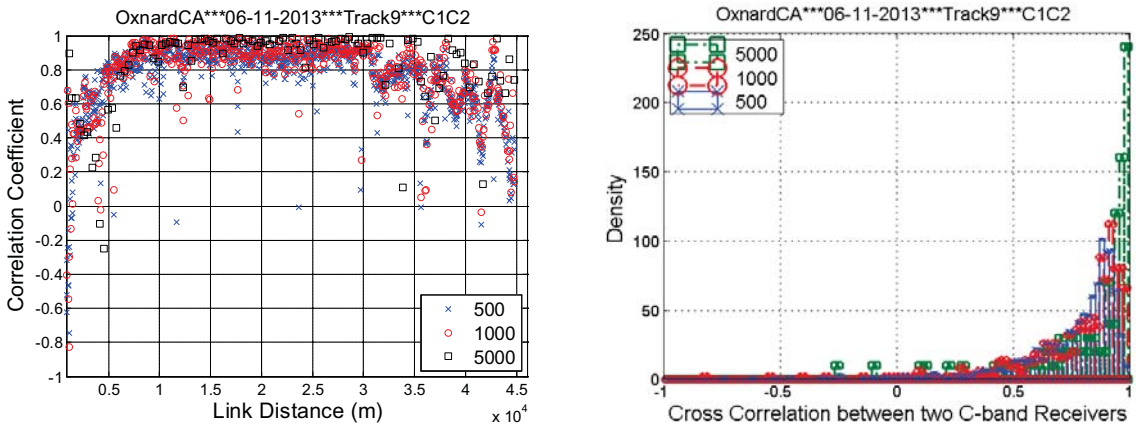

(a) (b)

Figure A39. Measured amplitude correlation coefficient between C-band Rx1 and 2 for FT9, for three different vector lengths: (a) correlation coefficient; (b) distributions of correlation coefficient.

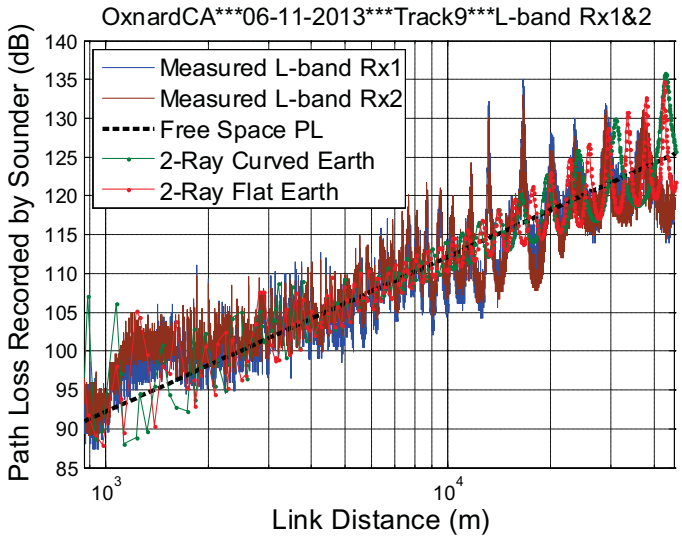

Figure A40. Path loss vs. distance for L-band Rx1 & 2 for FT9.

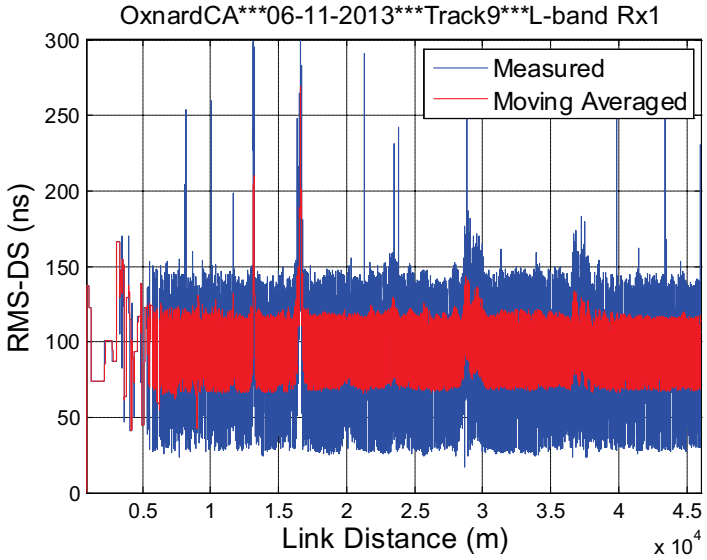

Figure A41. Measured RMS-DS vs. distance for L-band Rx1, FT9.

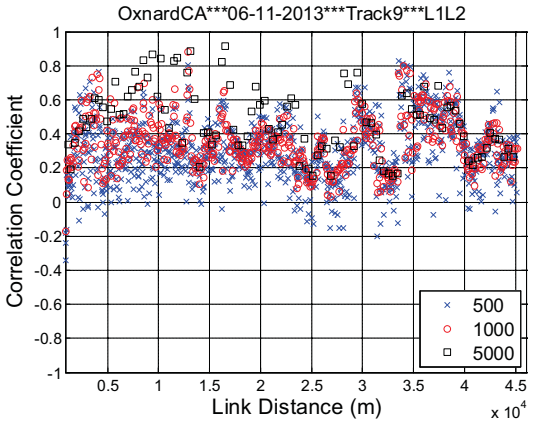

(a)

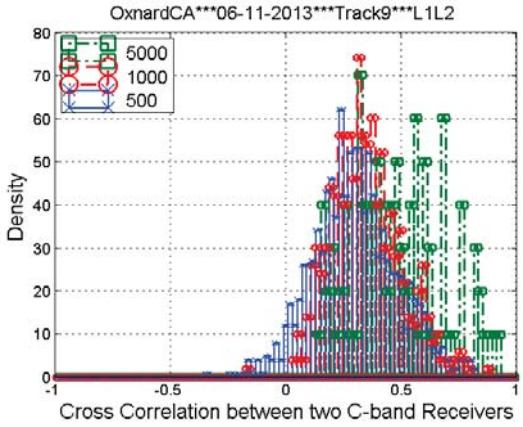

(b)

Figure A42. Measured amplitude correlation coefficient between L-band Rx1 and 2 for FT9, for three different vector lengths: (a) correlation coefficient; (b) distributions of correlation coefficient.

Table A7. Statistics of Cross Correlation Coefficients for Oxnard, Flight Track 9.

	C1C2			L1L2			C1L1	C1L2	C2L1	C2L2
Vector Length	500	1000	5000	500	1000	5000	1000	1000	1000	1000
Mean	0.75	0.77	0.82	0.30	0.35	0.48	0.00	0.00	0.01	0.01
Median	0.83	0.86	0.93	0.29	0.33	0.47	0.00	0.00	0.00	0.00
Max	0.98	0.99	0.99	0.83	0.88	0.92	0.82	0.85	0.76	0.75
Min	-0.74	-0.83	-0.25	-0.34	-0.17	0.15	-0.60	-0.65	-0.66	-0.55
Standard deviation	0.22	0.23	0.24	0.18	0.15	0.19	0.16	0.17	0.17	0.16

A.7 Flight Track 11

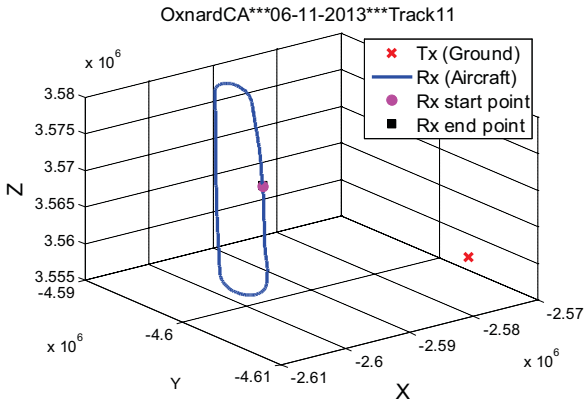

(a)

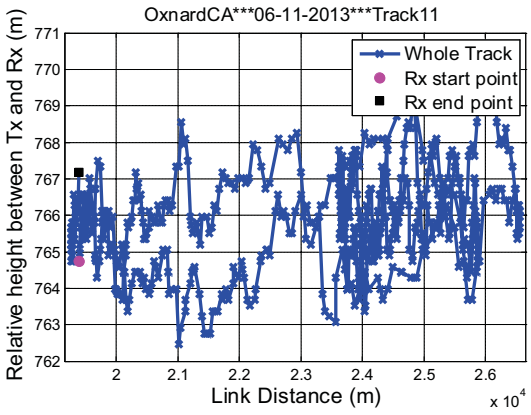

(b)

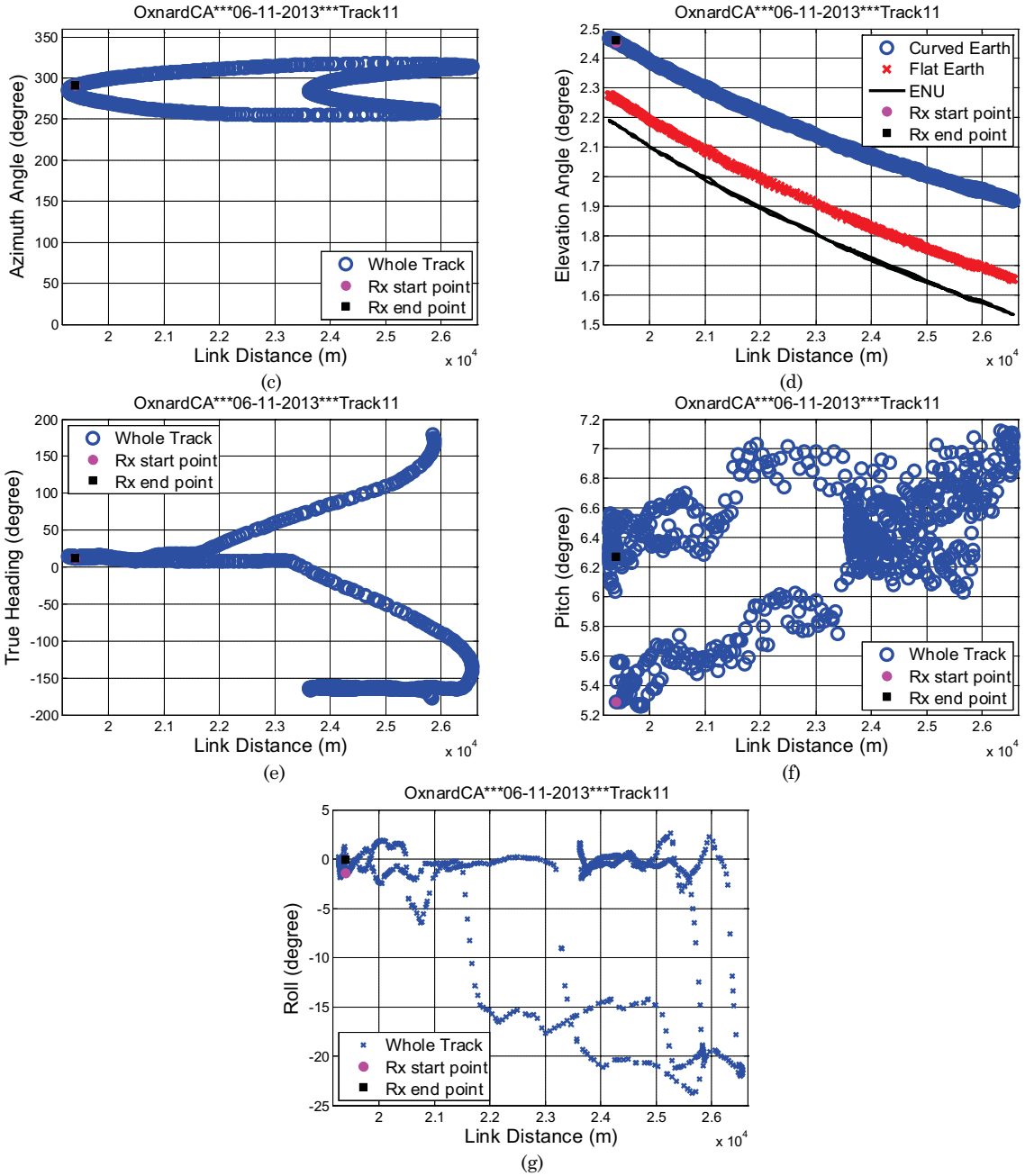

Figure A43. Geometric traces for FT11: (a) flight track in ECEF coordinates; (b) altitude difference between aircraft and ground station; (c) azimuth angle; (d) elevation angle; (e) heading of AC; (f) pitch angle of AC; (g) roll angle of AC.

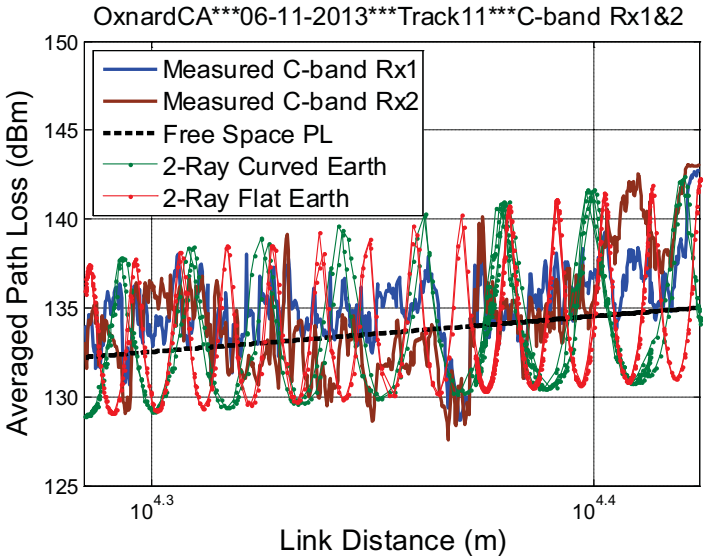

Figure A44. Measured path loss vs. distance for C-band Rx1 & 2, FT11.

Note that for the RMS-DS vs. link distance in Figure A45, a very large number of "spikes" appears. These spikes are almost certainly due to noise that has exceeded our noise thresholding algorithm's limit. We do know that in some flight tests, the aircraft electronic noise varies, hence this is our current hypothesis for the results of Figure A45 (although of course we do not have any explanation behind this noise variation, or its specific source). We will be re-processing this FT data after we analyze its noise statistics separately and devise a new value of noise threshold. (Similar comments pertain to FT12.)

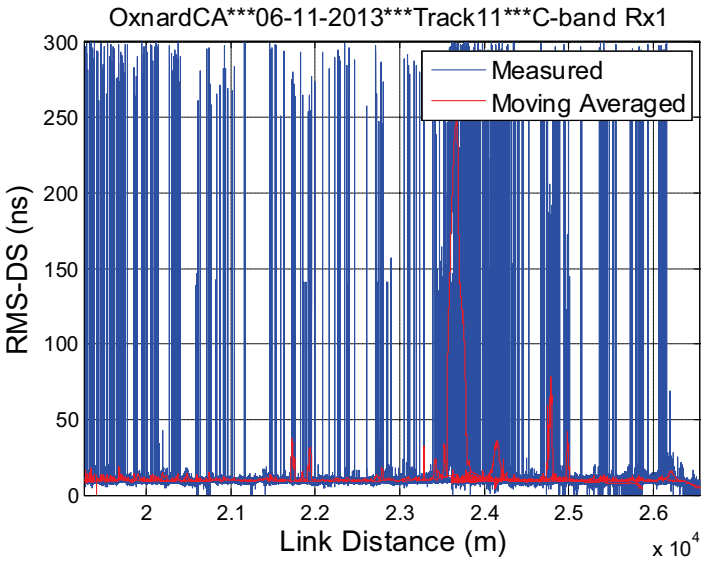

Figure A45. RMS-DS vs. distance for C-band Rx1, FT11.

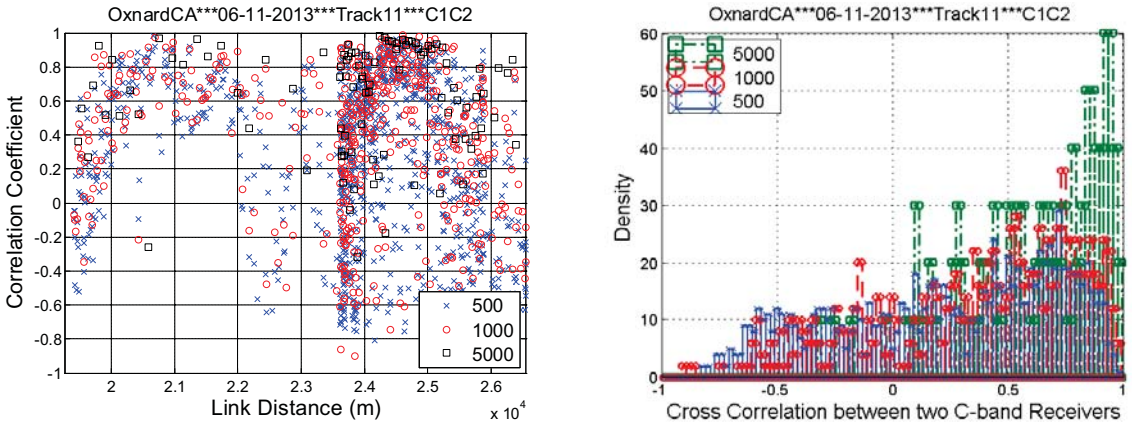

Figure A46. Measured amplitude correlation coefficient between C-band Rx1 and 2 for FT11, for three different vector lengths: (a) correlation coefficient; (b) distributions of correlation coefficient.

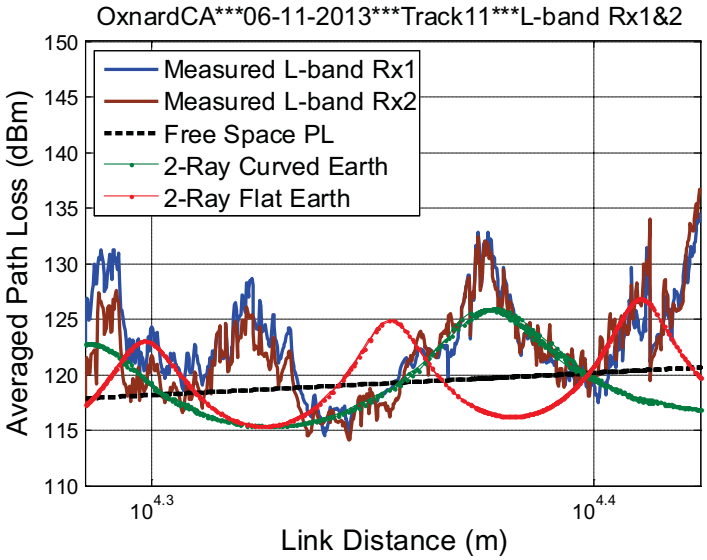

Figure A47. Path loss vs. distance for L-band Rx1 & 2 for FT11.

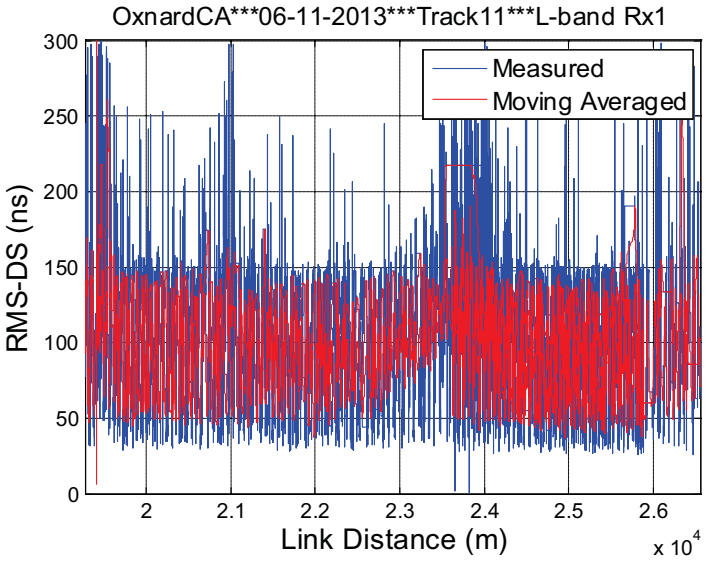

Figure A48. Measured RMS-DS vs. distance for L-band Rx1, FT11.

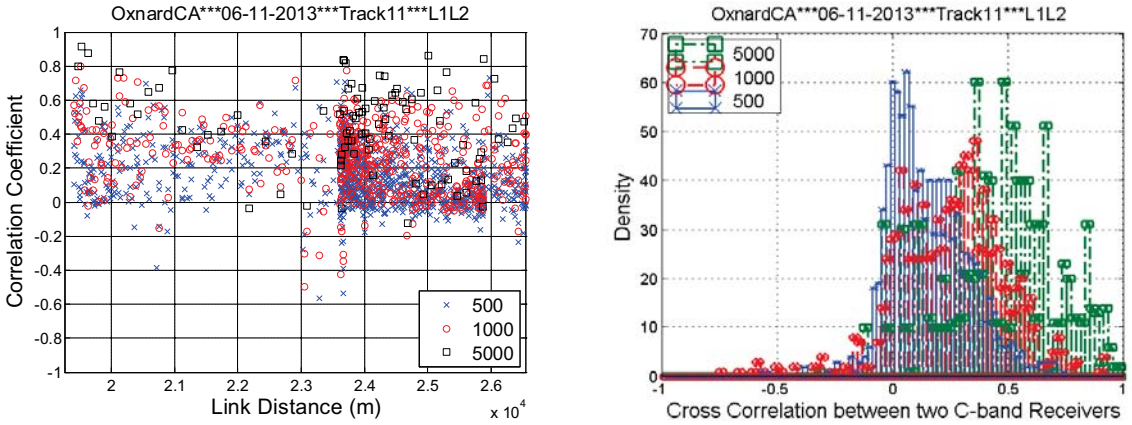

(a) (b)

Figure A49. Measured amplitude correlation coefficient between L-band Rx1 and 2 for FT11, for three different vector lengths: (a) correlation coefficient; (b) distributions of correlation coefficient.

Table A8. Statistics of Cross Correlation Coefficients for Oxnard, Flight Track 11.

	C1C2			L1L2			C1L1	C1L2	C2L1	C2L2
Vector Length	500	1000	5000	500	1000	5000	1000	1000	1000	1000
Mean	0.24	0.37	0.62	0.15	0.25	0.45	0.00	0.02	0.01	0.02
Median	0.31	0.46	0.70	0.12	0.27	0.47	0.02	0.03	0.02	0.04
Max	0.98	0.99	0.98	0.88	0.92	0.92	0.87	0.77	0.67	0.75
Min	-0.81	-0.90	-0.32	-0.81	-0.74	-0.12	-0.68	-0.73	-0.61	-0.64
Standard deviation	0.48	0.43	0.31	0.21	0.23	0.25	0.28	0.27	0.27	0.26

A.8 Flight Track 12

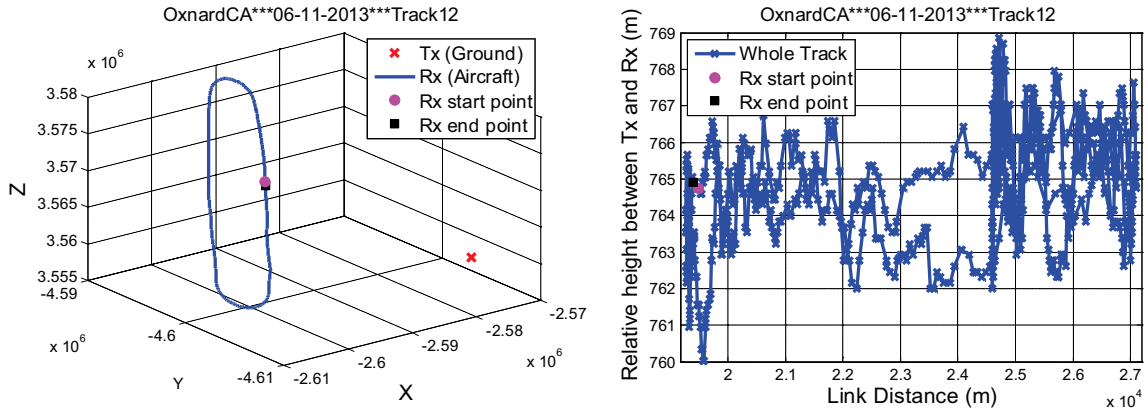

(a) (b)

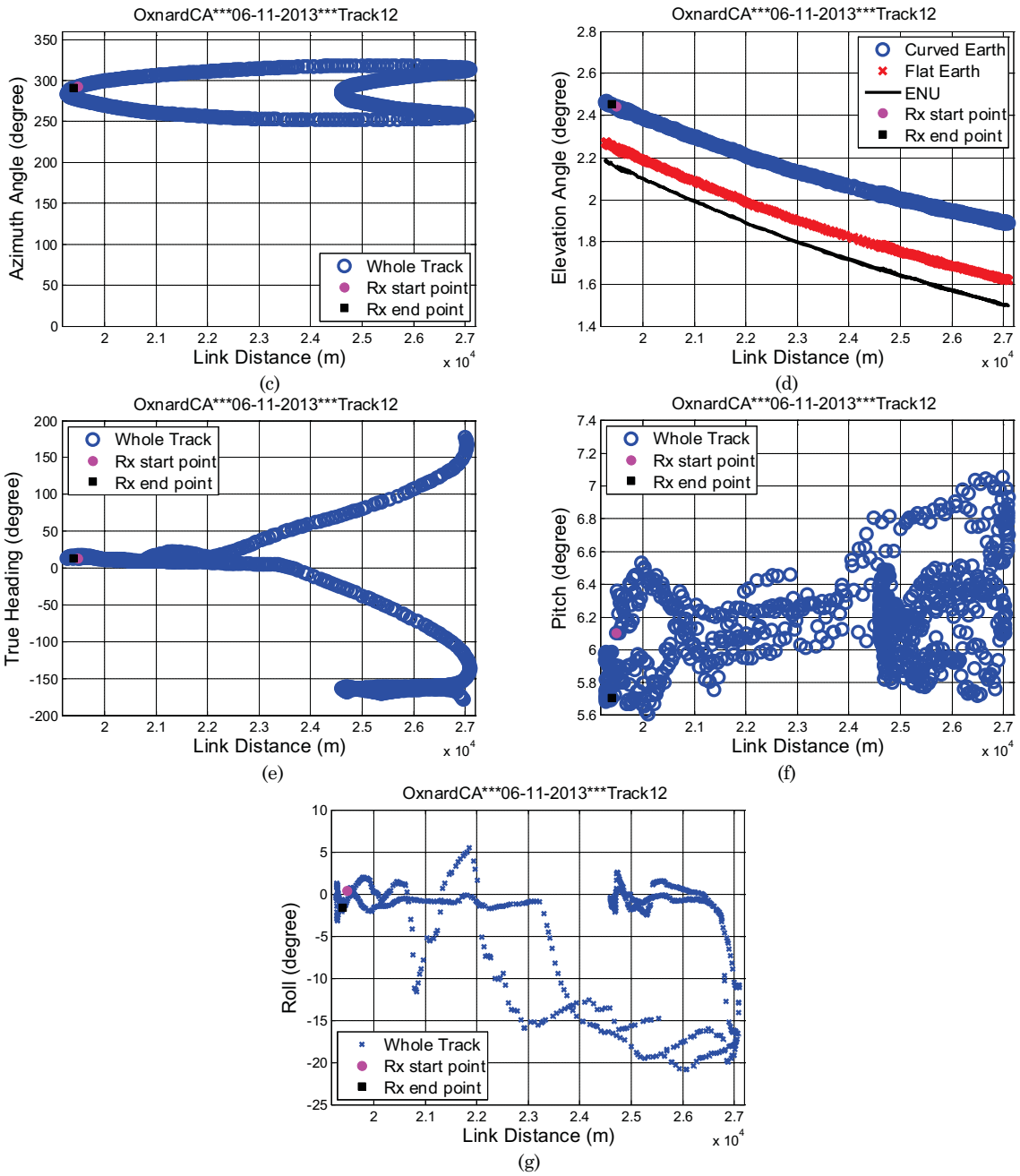

Figure A50. Geometric traces for FT12: (a) flight track in ECEF coordinates; (b) altitude difference between aircraft and ground station; (c) azimuth angle; (d) elevation angle; (e) heading of AC; (f) pitch angle of AC; (g) roll angle of AC.

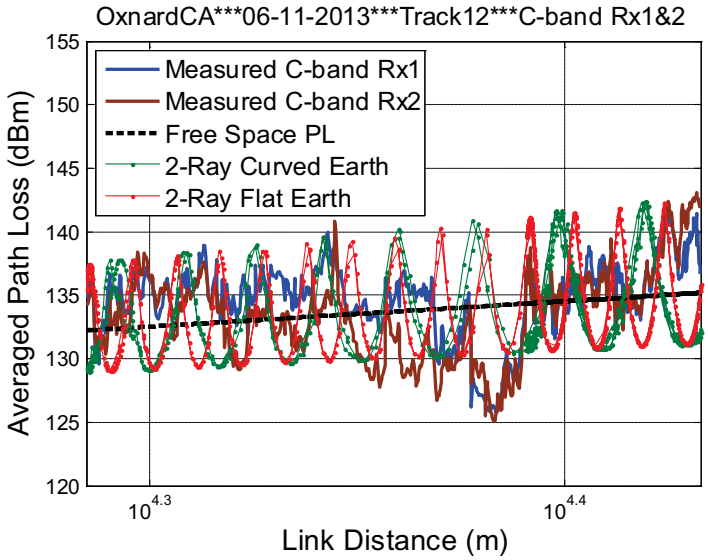

Figure A51. Measured path loss vs. distance for C-band Rx1 & 2, FT12.

As in FT11, Figure A52 shows anomalous large values of RMS-DS, which we believe is due to a temporary increase in aircraft electronic noise. The FT12 results will also be re-processed with their own noise threshold.

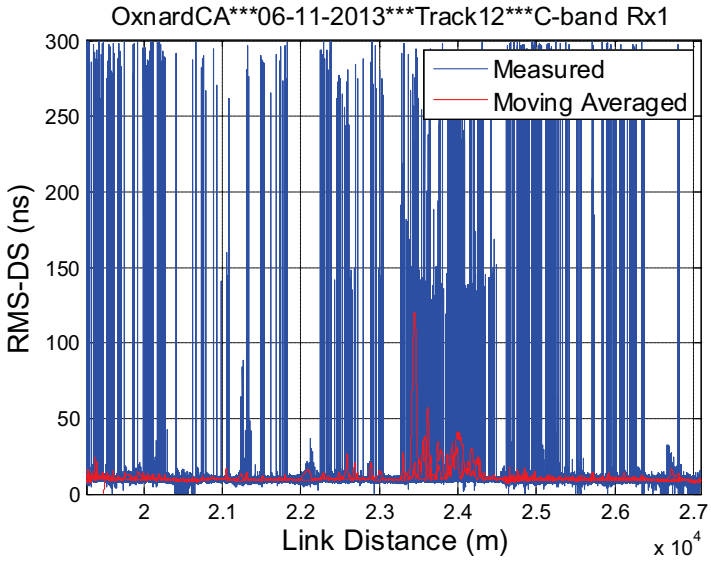

Figure A52. RMS-DS vs. distance for C-band Rx1, FT12.

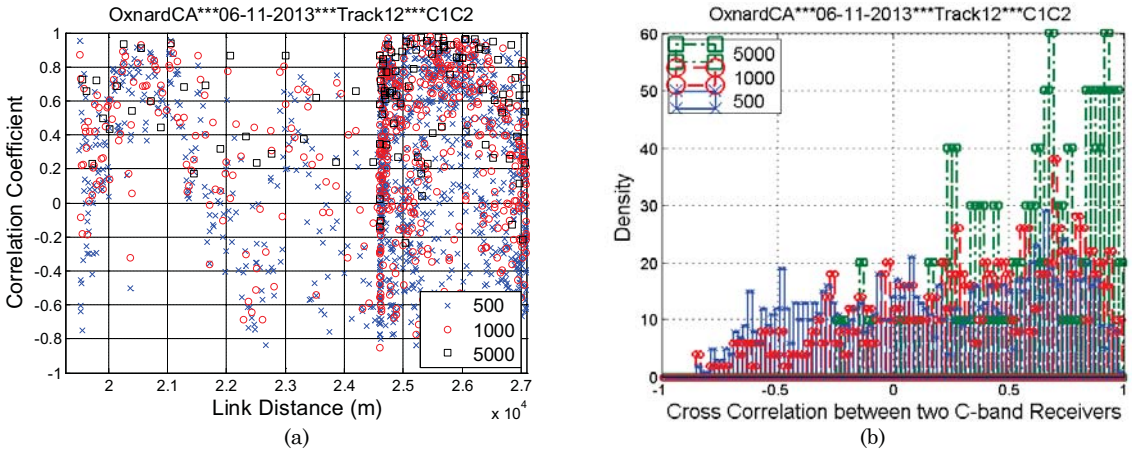

Figure A53. Measured amplitude correlation coefficient between C-band Rx1 and 2 for FT12, for three different vector lengths: (a) correlation coefficient; (b) distributions of correlation coefficient.

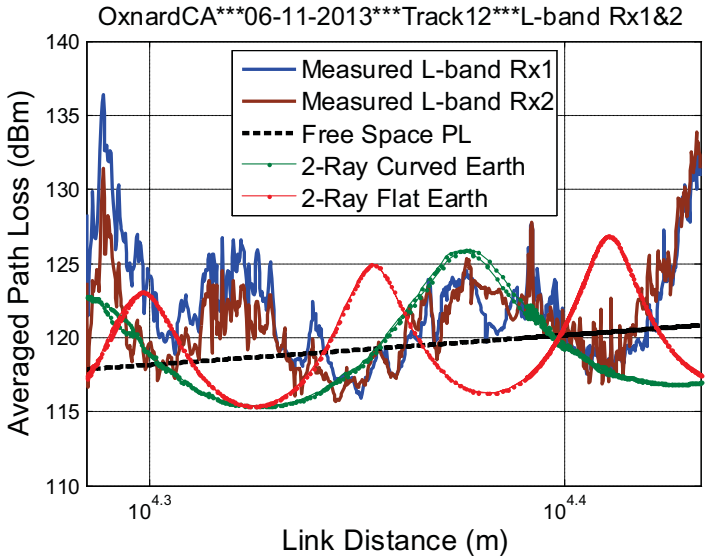

Figure A54. Path loss vs. distance for L-band Rx1 & 2 for FT12.

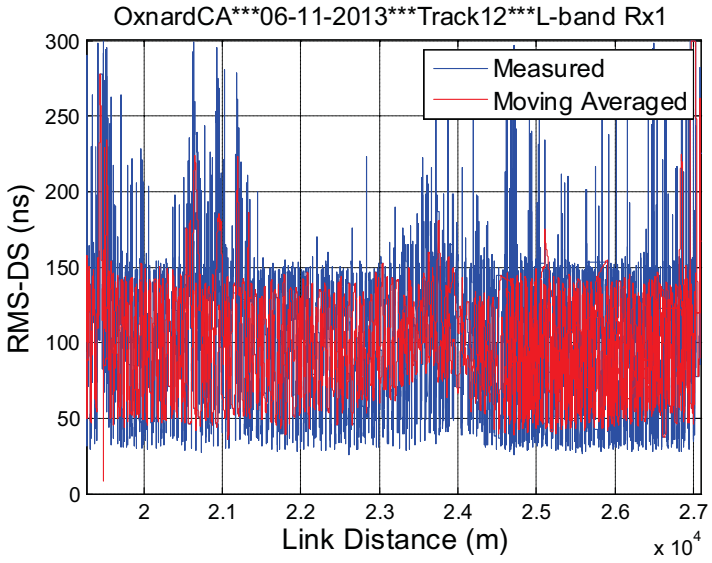

Figure A55. Measured RMS-DS vs. distance for L-band Rx1, FT12.

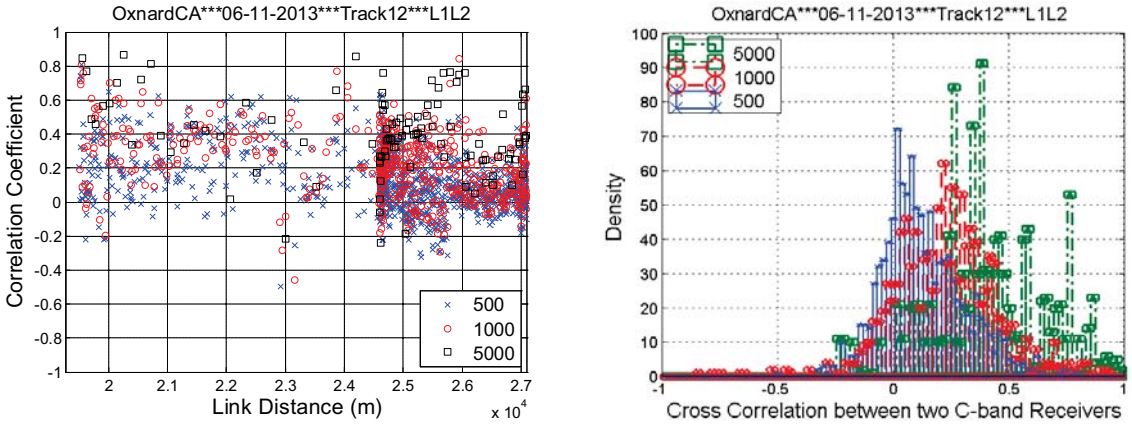

(a) (b)

Figure A56. Measured amplitude correlation coefficient between L-band Rx1 and 2 for FT12, for three different vector lengths: (a) correlation coefficient; (b) distributions of correlation coefficient.

Table A9. Statistics of Cross Correlation Coefficients for Oxnard, Flight Track 12.

	C1C2			L1L2			C1L1	C1L2	C2L1	C2L2
Vector Length	500	1000	5000	500	1000	5000	1000	1000	1000	1000
Mean	0.19	0.32	0.61	0.12	0.21	0.41	0.02	0.02	0.02	0.02
Median	0.21	0.39	0.67	0.10	0.22	0.39	0.02	0.02	0.02	0.02
Max	0.97	0.98	0.97	0.96	0.91	0.92	0.65	0.61	0.63	0.71
Min	-0.84	-0.85	-0.23	-0.84	-0.84	-0.24	-0.66	-0.53	-0.66	-0.70
Standard deviation	0.49	0.44	0.30	0.22	0.24	0.24	0.23	0.23	0.27	0.27

Appendix B: Noise Characterization

Here we address quantification of the sounder's noise. This was motivated by inspection of measured PDPs in which signal power was low, and noise components appeared larger than expected. For the noise characterization we use noise measured in several conditions:
1. in the laboratory, with the receivers terminated in matched loads;
2. in the aircraft on the ground, with all aircraft electronics turned on, with receivers terminated in matched loads; and
3. in the aircraft in flight, with all aircraft electronics turned on, and receivers connected to LNAs and antennas as in normal flight testing, with the aircraft at long range.
We also have some data for the conditions of case 3 but with both L-band and C-band transmitters turned off ("case 4"), and this may be analyzed in a future report.

The first case should provide a good characterization of the sounder's internal thermal noise. The second can show additional noise from the aircraft electronics, which enters the sounder through the Rx chassis. Both cases 1 and 2 force the receivers automatic gain control (AGC) to increase the sounder's internal noise to a level larger than when a signal is present, but these cases still allow for analysis of the noise distribution. The third case can show additional noise from aircraft electronics that enters the sounder both through the Rx chassis and/or through the antennas, LNAs, and cables to the Rx inputs, since in the relatively simple over-sea environment, it is easy to identify noise distinct from signal components. Case 4 results may be similar to those of cases 1 and 2 if the AGC acts to increase the sounder's noise; this may effectively "mask" the aircraft electronic noise.

B.1 Laboratory Measurements: Rx Inputs Terminated with Matched Loads

For this test, the receivers were in the NASA Glenn Research Center laboratory. We first provide some analytical results: the total in-band noise power is given by

$$P_{N,C} = -174 + 10log_{10}(50 \times 10^6) + NF_C \cong -97 \ + NF_C \ dBm \quad \text{(B.1)}$$
$$P_{N,L} = -174 + 10log_{10}(5 \times 10^6) + NF_L \cong -107 + NF_L \ dBm \quad \text{(B.2)}$$

where the first expression pertains to C-band, and the second to L-band. The terms NF_C and NF_L are the C- and L-band Rx noise figures, respectively. We do not have values for these noise figures yet, but the sounder manufacturer Berkeley Varitronics Systems is working on obtaining these values. In Table B.1 we provide statistics of measured thermal noise, in terms of the sample power values and chip power values. Note that for C-band, the sampling rate is 100 MHz and for L-band, the rate is 10 MHz; both sampling rates are twice the respective chip rates. Table B.2 provides cumulative noise statistics.

Table B.1. Measured Sounder Thermal Noise Statistics; in Laboratory, Rx terminated in matched loads.

	Receiver			
	C- Rx1	*C- Rx2*	*L- Rx1*	*L- Rx2*
Sample Power Mean (dBm)	-111.27	-109.40	-118.28	-119.55
Sample Power Median (dBm)	-112.86	-111.00	-119.95	-121.22
Sample Power Max (dBm)	-99.78	-97.06	-106.06	-107.48
Chip Power Mean (dBm)	-105.93	-104.10	-115.43	-116.43
Chip Power Median (dBm)	-107.52	-105.69	-117.11	-118.13
Chip Power Max (dBm)	-93.99	-92.49	-103.99	-103.79

Table B.2. Measured Sounder Cumulative Thermal Noise Statistics; in Laboratory, Rx terminated in matched loads.

	Receiver			
	C- Rx1	*C- Rx2*	*L- Rx1*	*L- Rx2*
Total Power Recorded (dBm)	-69.19	-69.31	-88.24	-88.50
Mean[Sum of Chip Powers] (dBm)	-75.83	-74.00	-85.33	-86.33
Median[Sum of Chip Powers] (dBm)	-75.83	-74.00	-85.33	-86.39
Max[Sum of Chip Powers] (dBm)	-75.41	-73.53	-84.97	-85.49

These statistics were obtained using 1000 PDPs for each receiver, thus more than 1 million chips were employed for the chip statistics. In Table B.1, for the C-band, the difference between the noise sample and noise chip power levels (mean & median) is approximately 5 dB, whereas for the L-band receivers, this difference is approximately 3 dB. The expected difference is 3 dB, thus for the C-band receivers, the chip noise power levels are slightly larger than expected. The means are approximately equal to the median values. The noise maxima are presented solely for completeness, as these maxima simply provide information on the range of power values.

The noise means, medians, and maxima in Table B.2 are essentially those for the total power in a PDP, obtained by summing all the chip power values. The statistics in this table were obtained by first computing the per-PDP values, then computing over the set of 1000 PDPs. The noise means and medians are approximately 30 dB above those of the chip power values in Table B.1; this is as expected, since we are summing the power over the 1023 chips in a PDP ($10log_{10}(1023)$~ 30 dB). The total power recorded by the sounder (denoted P_{tot} in prior reports [5]) is larger than the total chip mean value by approximately 5-6 dB for C-band, and 2-3 dB for L-band. This difference was reported as 4 dB for C-band in [5], so it appears that the scale factor that relates P_{tot} and the power levels as computed from the chip values is slightly different for each receiver, and may vary somewhat with time or signal input power. Our last comment on these results concerns the total noise average power (P_{tot} or the chip sum of Table B.2) and that computed by theory in equations (B.1) and (B.2): the chip sum values are 22-23 dB larger than that computed by theory as the noise power in the respective bandwidths. At least part of this is due to the unknown noise figures, but it is unlikely that the noise figures are this large. The primary reason is that with the Rx inputs terminated, the Rx automatic gain control (AGC) is amplifying the input to the A/D by the maximum amount. We next look at the noise distributions.

For C-band Rx1, in Figure B.1 (a) and (b) we plot histograms of the I and Q noise chips (linear scale). As expected, these closely follow a Gaussian (normal) distribution with zero mean. In part (c) of Figure B.1 we show the histogram of the amplitude $\sqrt{I^2 + Q^2}$, which as expected follows a Rayleigh distribution, and in (d) we show the histogram of the chip power $p_c=I^2+Q^2$ (watts), which (again as expected) follows the exponential distribution. The distributions for the chip and sample powers on a log scale appear in Figure B.1 (e) and (f), respectively. The chip power distribution is the distribution of the variable $P_c=10log_{10}(p_c/0.001)$, in dBm. This is not a common distribution, but it is straightforward to derive: the probability density function of p_c is the exponential,

$$f_p(x) = a\ exp(-ax), \text{ for } x \geq 0 \tag{B.3}$$

where "x" is the dummy variable of the probability density function, the mean is $1/a$, and the variance $1/a^2$. A transformation of random variables and some algebra yields

$$f_P(y) = a\ ln(10) 10^{\frac{y}{10}-4} exp\left(-a 10^{\frac{y}{10}-3}\right) \tag{B.4}$$

which is also in good agreement with measured results of Figure B.1 (e). Figures B.2-B.4 provide analogous results for the other three receivers, all of which show expected characteristics. Thus,

although we must be aware of the scale factors between power levels computed by summing chips in PDPs and the sounder's total power P_{tot}, for the case with the receiver inputs terminated in matched loads, the sounder's internal noise characteristics are as expected.

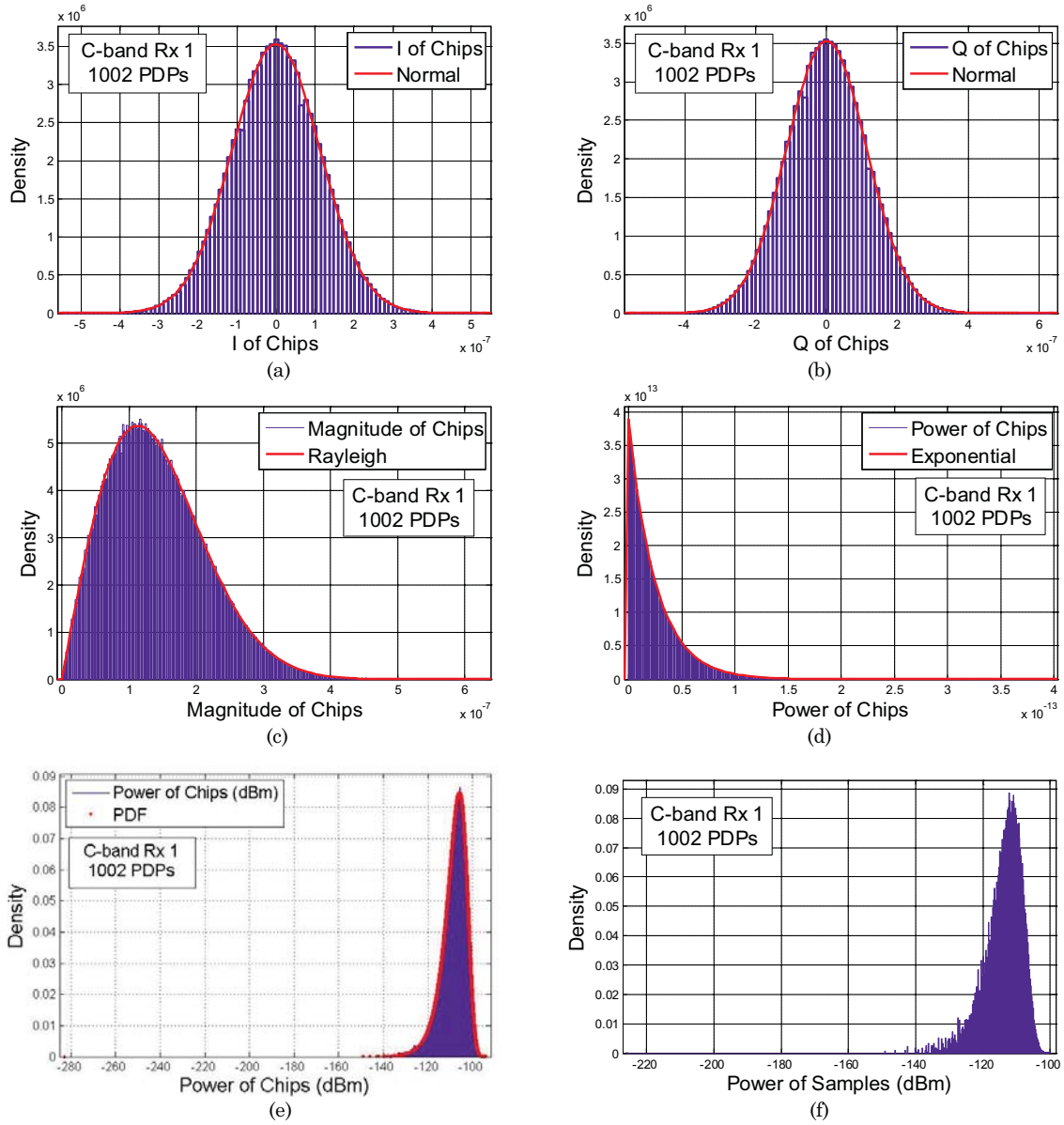

Figure B.1. Distributions of C-band Rx 1. (a) I component of chips; (b) Q component of chips; (c) chip magnitudes; (d) chip power in linear scale; (e) chip power in dBm; (f) sample power in dBm.

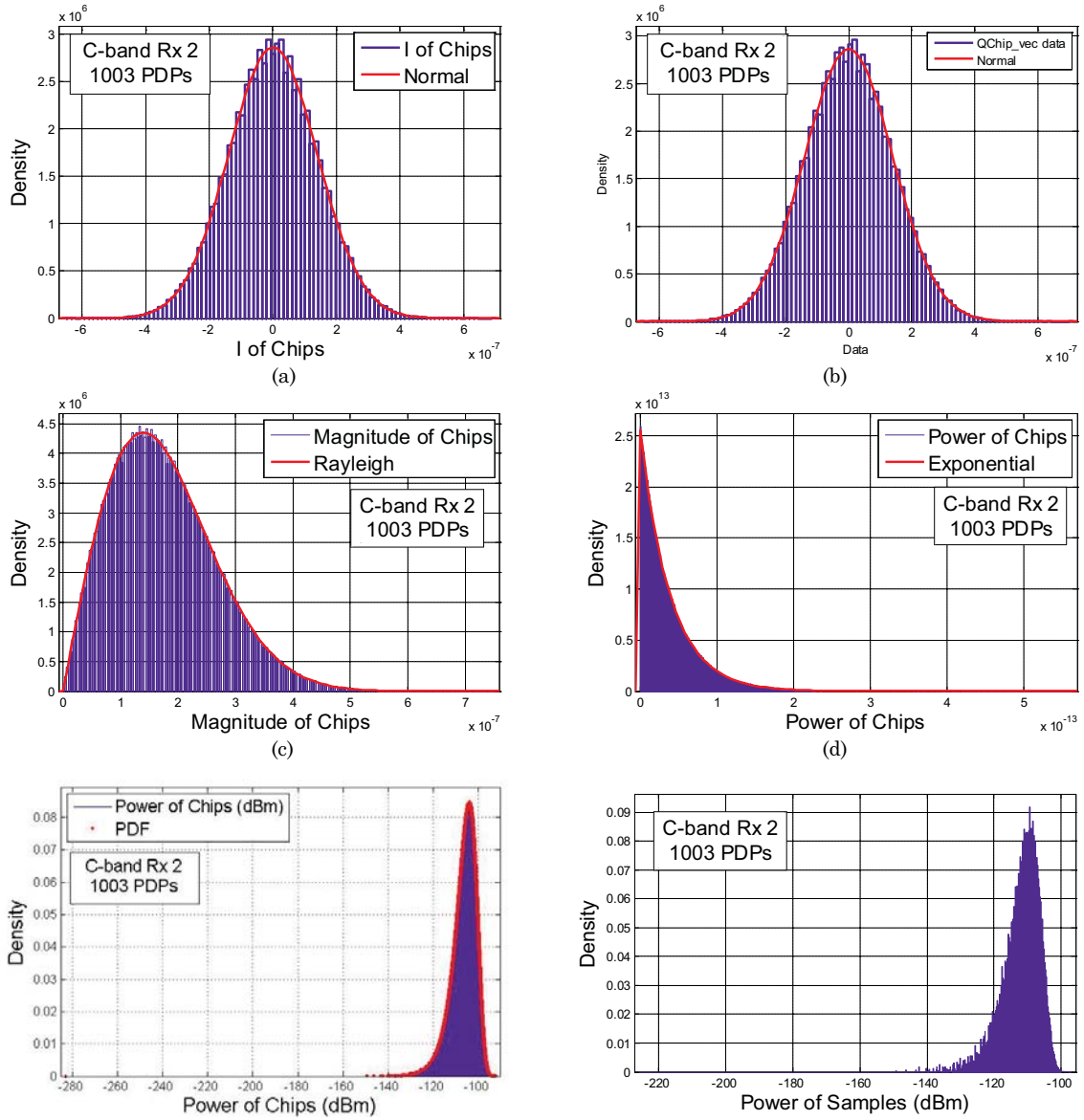

Figure B.2. Distributions of C-band Rx 2. (a) I component of chips; (b) Q component of chips; (c) chip magnitudes; (d) chip power in linear scale; (e) chip power in dBm; (f) sample power in dBm.

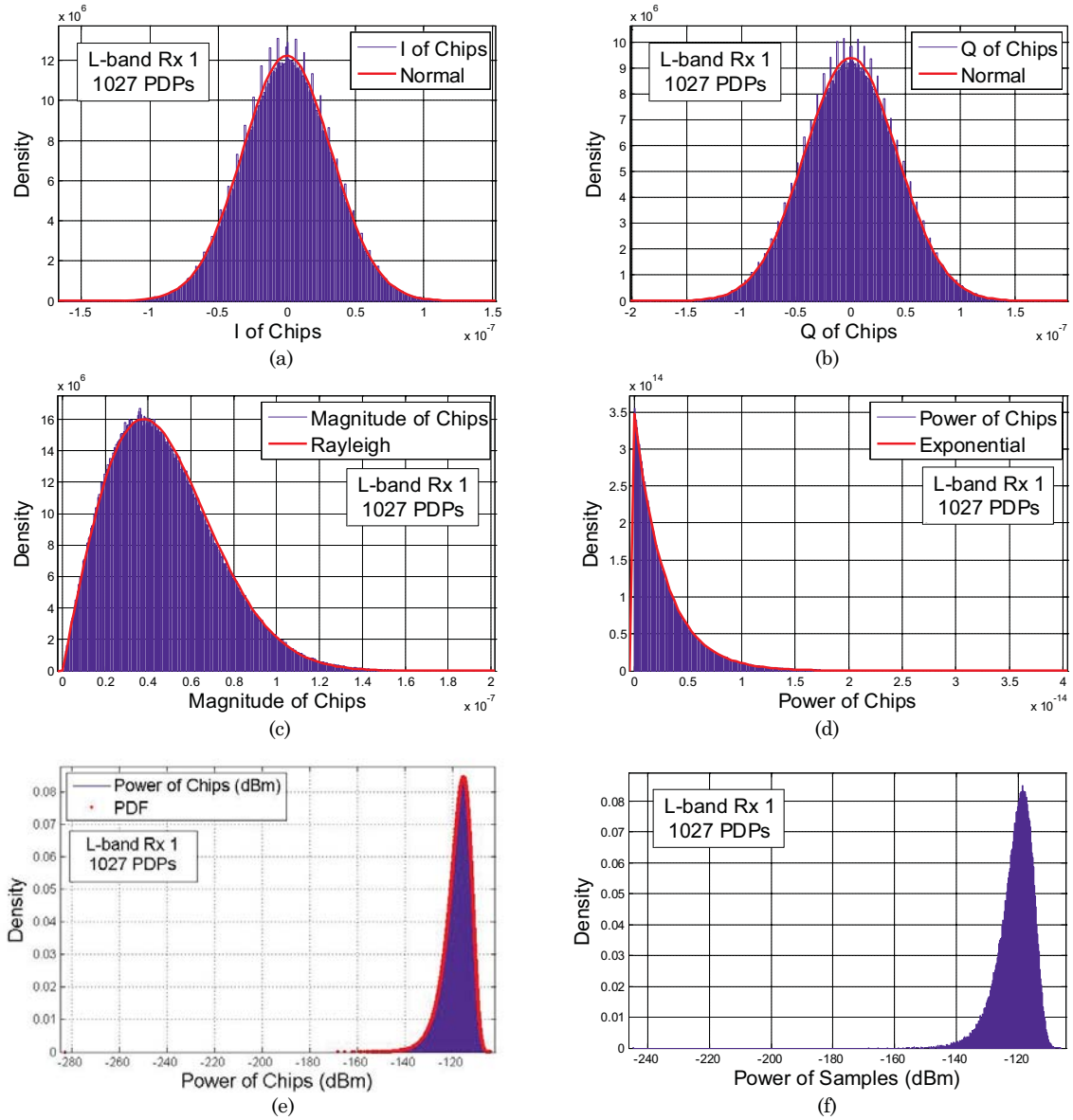

Figure B.3. Distributions of L-band Rx 1. (a) I component of chips; (b) Q component of chips; (c) chip magnitudes; (d) chip power in linear scale; (e) chip power in dBm; (f) sample power in dBm.

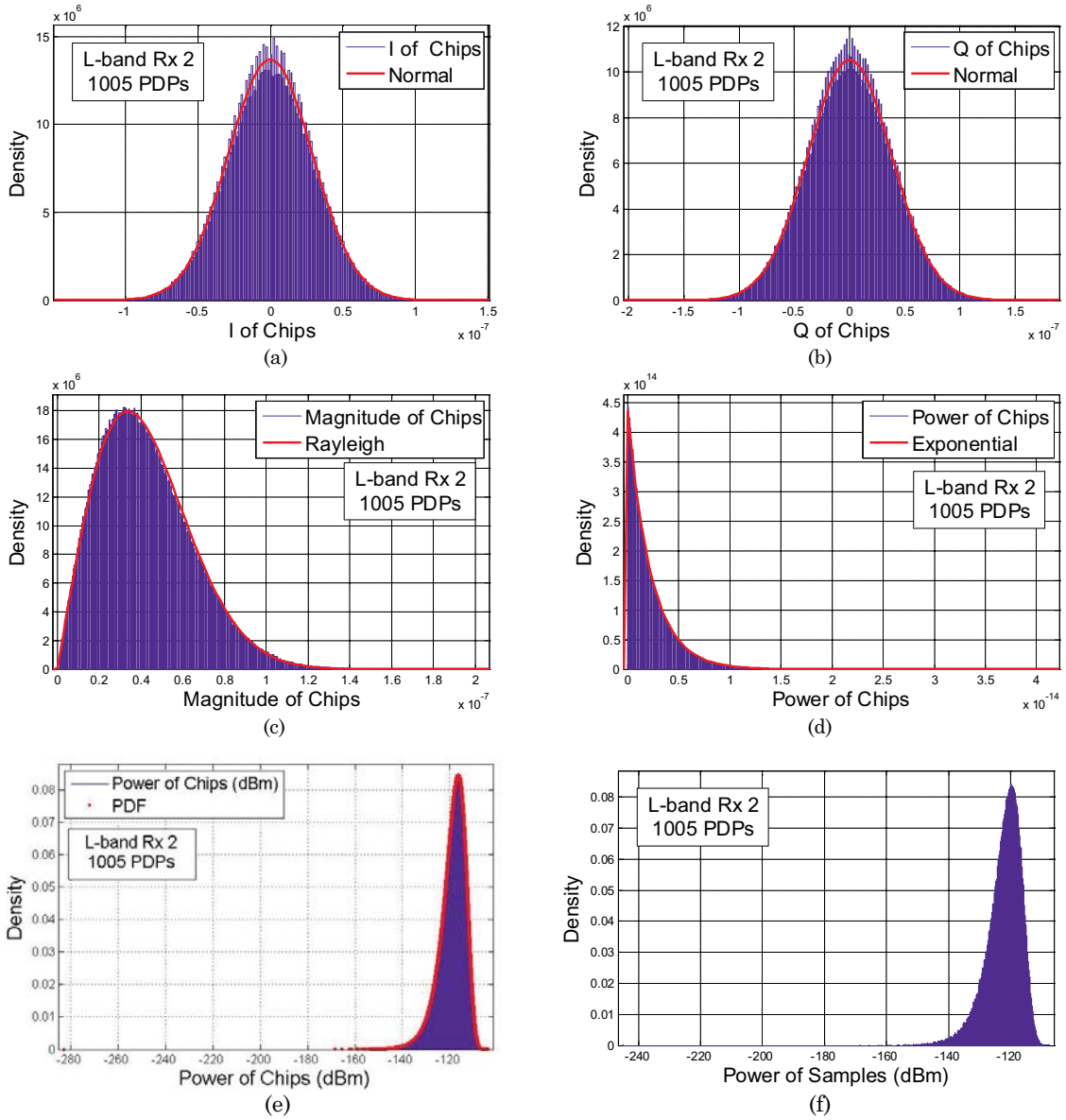

Figure B.4. Distributions of L-band Rx 2. (a) I component of chips; (b) Q component of chips; (c) chip magnitudes; (d) chip power in linear scale; (e) chip power in dBm; (f) sample power in dBm.

B.2: Flight Test: Aircraft on Ground, All Aircraft Electronics On, Rx's Terminated in Matched Loads

This data was taken with the aircraft on the airport surface at Glenn Research Center. Statistics analogous to those in Tables B.1 and B.2 are shown in Tables B.3 and B.4 for this case. From a comparison of the results for the two cases, it can be seen that the noise recorded by the sounder in this case is statistically identical to that measured in the laboratory. This result shows that any additional noise caused by the aircraft electronics is well below the level of the sounder's internal thermal noise when the aircraft noise must enter through the ambient environment and sounder Rx chassis. Again though, because of the behavior of the Rx AGC, this internal noise is

amplified beyond its "quiescent" level. Since we have no easy way to disable the AGC, we must rely on the other test cases for a complete characterization of any external noise.

Because of the similarity of results to case 1, we do not repeat histograms and curve fits to the histograms of the receiver noise distributions as in Figures B.1-B.4. We do though show plots of the noise chip phase histograms for all four receivers, in Figure B.5. The expected distribution is uniform, and this is well approximated by the C-band results; the L-band noise phases are slightly peaked at $\pm\pi/2$. This was also observed previously in laboratory results [5].

Table B.3. Measured Sounder Thermal Noise Statistics; in Aircraft on Ground, Rx terminated in matched loads.

	Receiver			
	C- Rx 1	*C- Rx 2*	*L- Rx 1*	*L- Rx 2*
Sample Power Mean (dBm)	-111.23	-109.45	-118.32	-119.32
Sample Power Median (dBm)	-112.81	-111.03	-119.99	-120.99
Sample Power Max (dBm)	-99.14	-97.32	-105.57	-106.27
Chip Power Mean (dBm)	-105.87	-104.15	-115.47	-116.13
Chip Power Median (dBm)	-107.46	-105.74	-117.16	-117.82
Chip Power Max (dBm)	-93.92	-92.34	-103.47	-103.08

Table B.4. Measured Sounder Cumulative Thermal Noise Statistics; in Aircraft on Ground, Rx terminated in matched loads.

	Receiver			
	C- Rx 1	*C- Rx 2*	*L- Rx 1*	*L- Rx 2*
Total Power Recorded (dBm)	-69.19	-69.31	-88.24	-88.50
Mean[Sum of Chip Powers] (dBm)	-75.77	-74.05	-85.37	-86.03
Median[Sum of Chip Powers] (dBm)	-75.77	-74.05	-85.37	-86.03
Max[Sum of Chip Powers] (dBm)	-75.24	-73.53	-84.92	-85.57

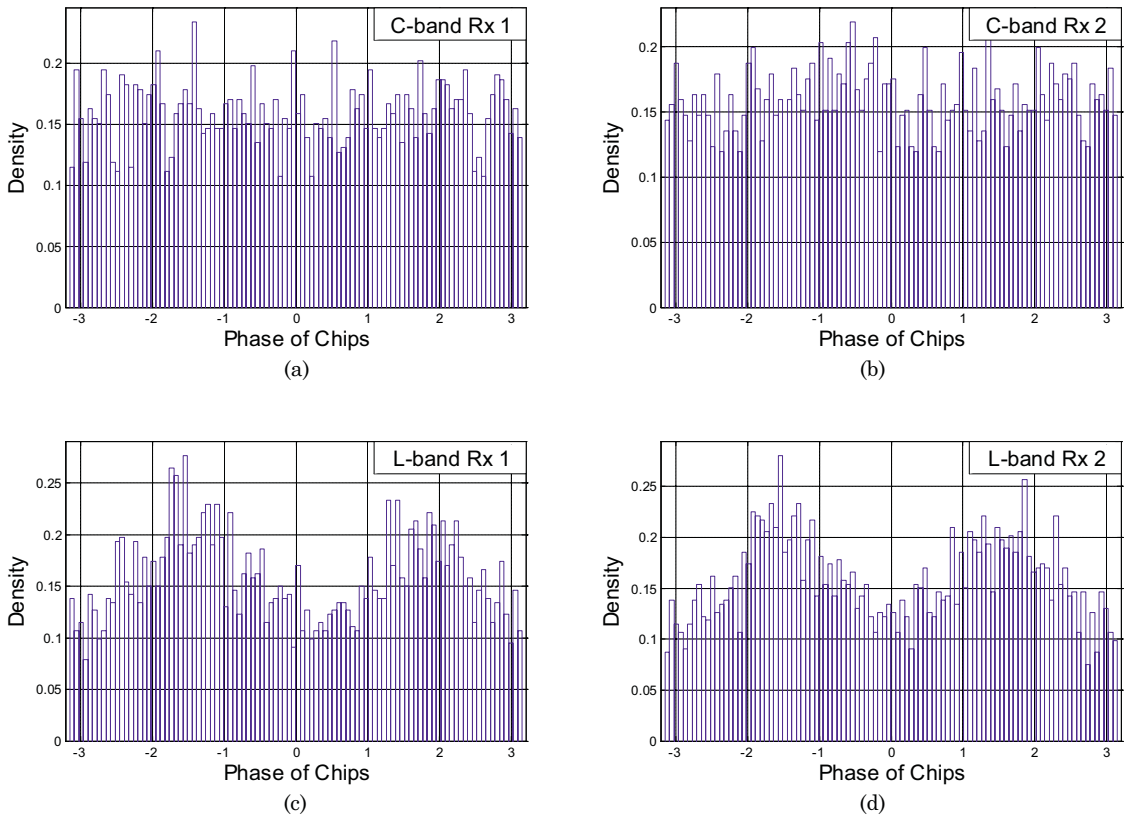

Figure B.5. Distributions of all four Rx noise chip phases: (a) C-band Rx1; (b) C-band Rx2; (c) L-band Rx1; (d) L-band Rx2. Aircraft on ground with all electronics on, Rx terminated in matched loads.

B.3 Flight Test: Aircraft in Flight, All Aircraft Electronics On, Rx's Connected to Antennas as in Normal Testing, All Tx's ON, Link Range Very Large

In this case the aircraft and channel sounder are operating in their normal, data collection mode, but the link distance was very large (~40 km). In this condition, the LOS component is present, but weak, and the primary sea-surface reflection is unresolvable, thus it is relatively easy to identify the LOS component, and any additional components are with very high probability noise components that exceed the 30 dB threshold. These results are primarily from the Oxnard flight test, flight track 2, in which the aircraft was flying directly away from the GS. We also include some results from a recent flight test in Cleveland. For these results, each PDP was circularly shifted so that the maximum chip (LOS component) is at chip index 5. Chips indexed 951 to 1023 were set to zero to remove the false MPC in C-band [3]. All chips from the 500th to the 949th chip are classified as noise, and are used to collect noise statistics. The excess delay of the 501st chip relative to the LOS component is 496 chips, corresponding to a link distance difference of 2976 meters. For the long-distance, over-sea environment, we expect no true MPCs at relative distance of ~ 3 km from the LOS, hence the samples we collect here are, with near certainty, all noise.

Figure B.6 shows the distributions of these noise samples for four different files, numbered 141-144. File 141 is at the closest distance (still >40 km) and subsequent files are at slightly larger distances. Each of these distributions shows *two* noise modes. The mode with larger probability mass, at the smaller mean value, is the sounder internal thermal noise, and it is most likely that the mode at the higher mean value is due to aircraft electronic noise. Note that as link distance increases (files 141 to 144), the sounder thermal noise mean value decreases slightly (~ 1 dB). This is most likely due to path loss increase. The mean of the aircraft electronic noise does not vary much with distance. Also important is that the internal thermal noise distribution is truncated: in flight

testing we employ a threshold of 30 dB below the maximum (typically LOS) component, and this threshold removes the weaker samples at the left of the distribution. One can observe this clearly in files 141-143, less so in file 144. The distribution of this internal thermal noise should be that of Figure B.1(e), but is altered by this thresholding truncation. Some additional plots, using much more data from a larger set of files, are shown in Figure B.7. These also clearly evince the bi-modal distribution, with the larger-mean aircraft electronic noise mode distribution fairly constant.

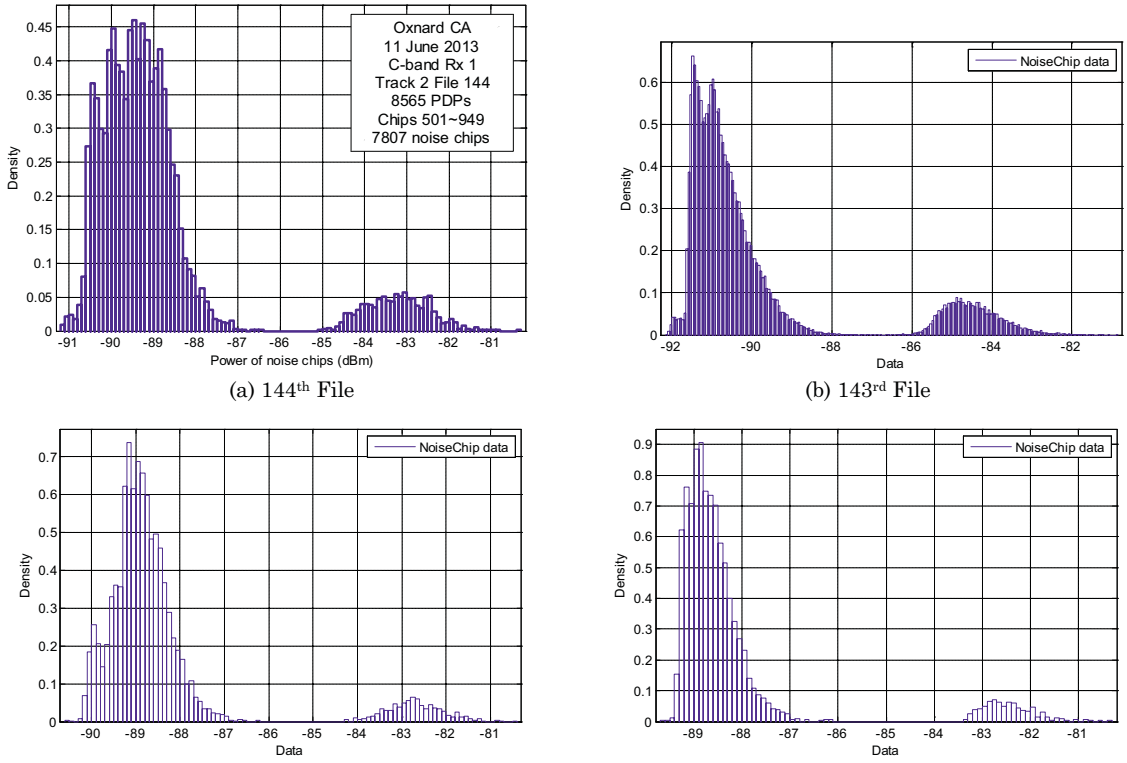

(a) 144th File

(b) 143rd File

(c) 142nd File

(d) 141st File

Figure B.6. Distributions of noise chips for C-band Rx1, four files of FT1: (a) file 144; (b) file 143; (c) file 142; (d) file 141.

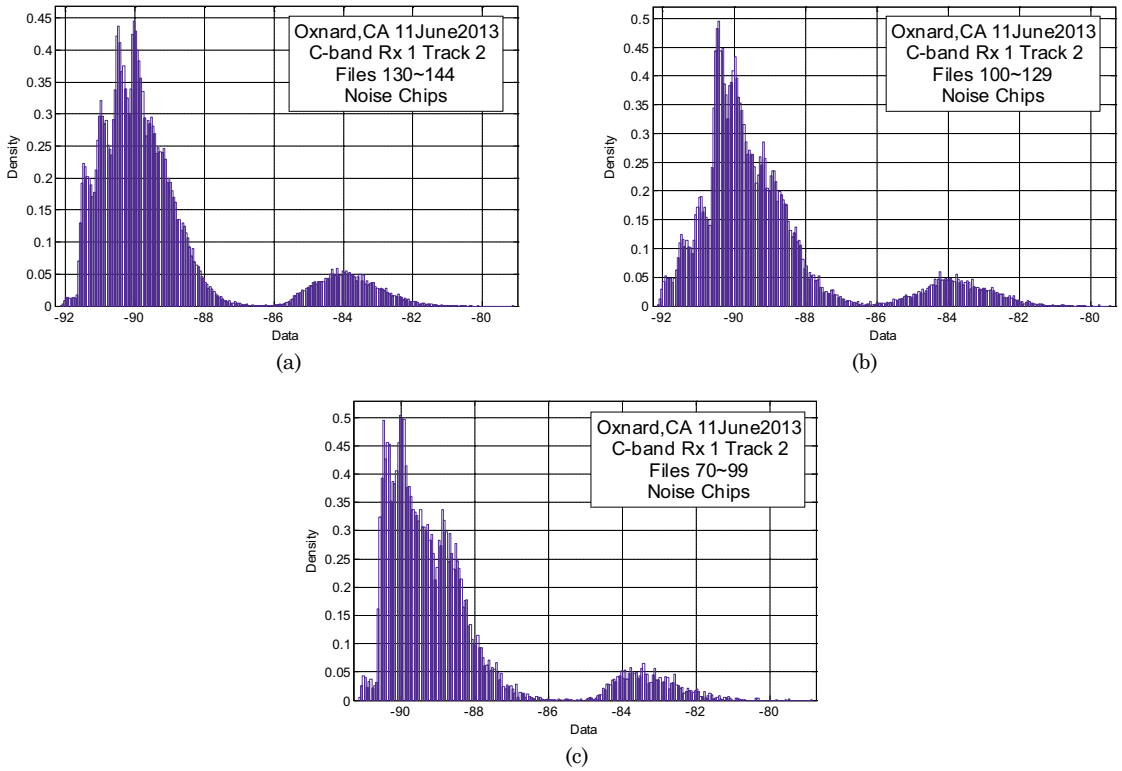

Figure B.7. Distributions of noise chips for C-band Rx1, collected over multiple files of FT1: (a) files 130-144; (b) files 100-129; (c) files 70-99.

As noted, our interest in the noise characteristics arose from observation of PDPs when the signal input power is low. In this condition, even if the signal is present, and a 30 dB threshold below this signal component is applied, the signal to noise ratio (SNR) is typically low enough to allow the larger noise samples to get through in the recorded PDPs. One way to remove these is to view the sequence of PDPs over time: if a sample is a true MPC, it will likely persist for some moderate duration; if the sample is noise, it will most likely appear isolated in a single PDP. The persistence duration of valid MPCs is not trivial to determine, as it depends upon velocity and the environment geometry. Nonetheless, since we are collecting PDPs at a rate of approximately 2 kHz, each PDP is separated in time from the next by approximately 0.5 ms—valid MPCs should persist for more than one PDP. We address this processing in Appendix C.

An alternative to the rather processing-intensive scanning of PDPs over time is the use of an additional threshold. Our quantification of the system noise (both sounder internal thermal, and the external aircraft electronic) can enable us to devise such a threshold with quantifiable performance. For this we need to construct an analytical model of the bi-modal distribution, or of the aircraft noise distribution. We do this also in Appendix C.

We provide a few more examples of measured noise distributions for this case. Figure B.8 shows results for all four receivers, in which noise data from a large number of files were aggregated. For the C-band results, it appears that multiple modes are present for the sounder's internal thermal noise, but we attribute this to path loss variation. A second-order cause of this may be AGC effects that scale the mean as the input signal power varies; note that the external aircraft electronic noise mode is still fairly constant. For the L-band results, the path loss of the two L-band receivers does not reach a value at which the SNR is low even at the largest distances of over 40 km. Hence the noise chips shown in Figures B.8 (c) and (d) are not attributable to a low received power that introduces noise within the 30 dB threshold as in the C-band receivers. A similar statement regarding the multiple internal noise modes can though be made for the L-band results, but with two

added comments: (1) it is not certain if the L-band receivers have *any* strong external noise mode, since if this mode exists, it is not clearly separate from the internal thermal noise mode(s); and (2) the L-band receivers have been shown to exhibit anomalous results in the form of PDPs with extremely large delay spreads. These PDPs have components nearly filling the entire delay range (over 200 microseconds), and hence the "noise components" in these PDPs are not actual noise, but rather produced by some unexplained issue within the L-band receivers. In any case, we can still proceed to devise a thresholding algorithm for the L-band data. Due to the unusual shape of the L-band distributions, this L-band thresholding algorithm will be based upon empirical probabilities derived from the data itself, and not based on an analytical modeling procedure.

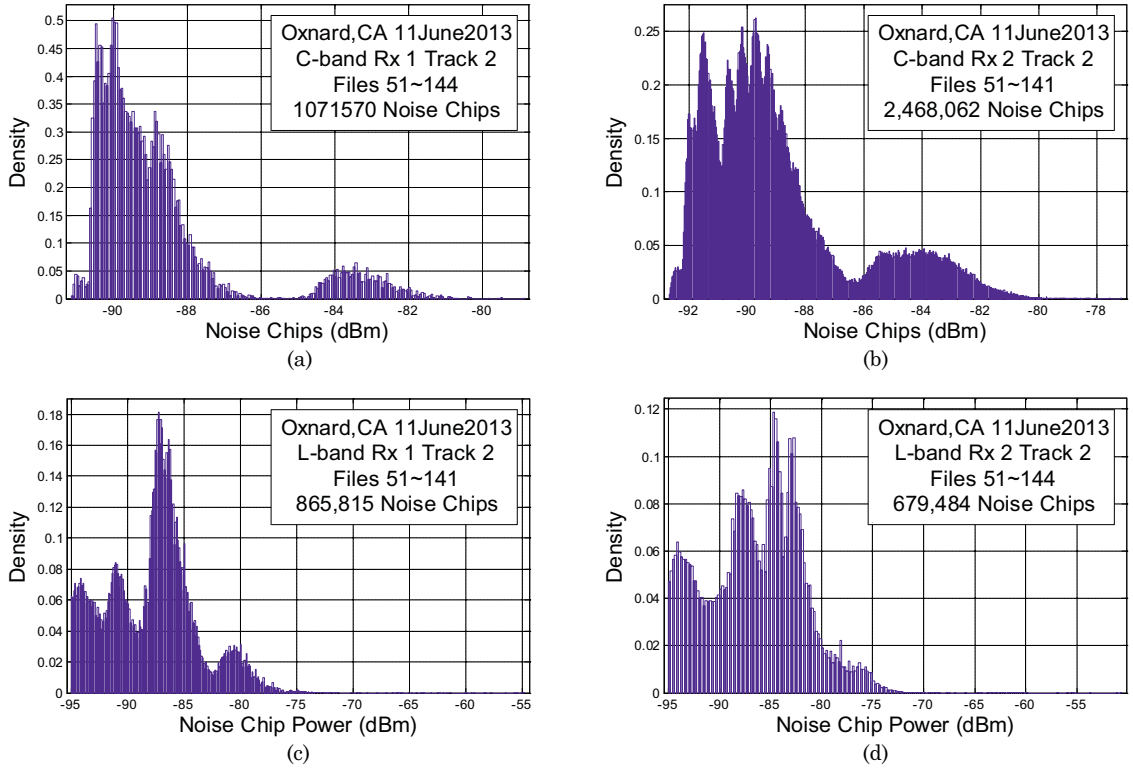

Figure B.8. Distributions of noise chip power in dBm, collected over a large number of files for all four Rxs in Oxnard tests: (a) C-band Rx 1; (b) C-band Rx 2; (c) L-band Rx 1; (d) L-band Rx 2.

We show one final result in this section, for flight test data taken in Cleveland in September 2013. Here again we use results for the aircraft at a fairly large range, where we have gathered noise chips at large delay values relative to the LOS component. Figure B.9 shows the results for C-band Rx1. The external aircraft electronics noise mode is evident, at approximately the same values as for the Oxnard data. Thus the aircraft electronics noise appears to be statistically stationary across these two different tests.

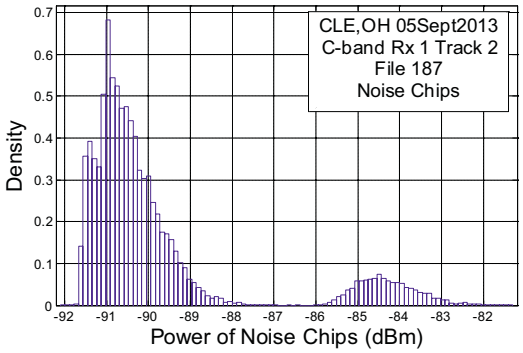

Figure B.9. Distribution of noise chip power in dBm for file 187 in Cleveland flight test (September 2013) for C-band Rx 1.

Appendix C: Noise Removal Algorithm

The noise removal algorithm has multiple parts, and includes the application of several thresholds. The removal algorithm is divided into four steps:

1. a 30 dB threshold is applied by the sounder; any chips with power 30 dB smaller than the strongest chip of a power delay profile (PDP) are removed;
2. a noise threshold N_T (dBm) is applied to the collected PDPs, using either an analytical method (constant threshold) or an empirical method (adaptive threshold); both of these thresholds rely on collection of data classified as noise, to estimate noise statistics. One way to do this is to use a "delay gate," in which we estimate the maximum delay for a valid MPC, and classify all chip values at larger delays as noise. This "maximum valid MPC delay" is environment dependent, and will likely change for other GS settings. For the over-sea data, this delay is relatively easy to determine;
3. a root-mean square delay spread (RMS-DS) threshold S_T (ns) is used to remove remaining PDPs after step 2 that have unrealistically large RMS-DS (these are attributable to large noise components that exceed the threshold). This thresholding step is also environment-specific, and in complicated environments, this thresholding step may be omitted;
4. when step 3 is used, the PDPs resulting after step 3 are classified into two subsets, one with small RMS-DS, and one with large RMS-DS. The "large RMS-DS" PDPs have delay spreads less than S_T, but appear as "spikes" in plots of RMS-DS vs. PDP index. These are easily identified, and fairly few in number. Once identified, the "large RMS-DS" PDPs are observed in the time domain, to assess the time duration that a potential MPC is present (its "lifetime" or "persistence"). As previously noted, actual MPCs will persist, whereas noise spikes will not. If step 3 is not used, we still perform MPC persistence checks for PDPs with larger values of delay spread.

Since step 1 is a sounder-internal operation, we only discuss steps 2 to 4 in this appendix.

Figure C.1 shows example PDPs for C-band Rx1. The left PDP is denoted "good" and the right PDP "bad," to indicate that the MPCs at chip indices approximately 330 and 920 are not true MPCs but are instead caused by noise spikes above the sounder's 30 dB threshold. These spikes are classified as noise since if they were true MPCs, their delays would correspond to excess path lengths of approximately 1.98 km and 5.52 km, respectively. For these PDPs, link distance was large (~45 km), and the geometry of the test environment does not support the hypothesis of large reflecting objects at such large relative distances. Figure C.2 shows analogous "good" and "bad" PDPs for L-band.

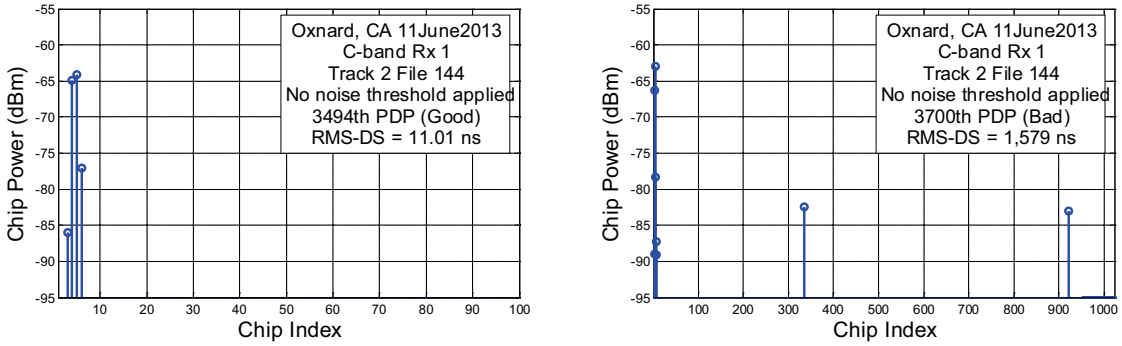

Figure C.1. Example "Good" and "Bad" PDPs in C-band.

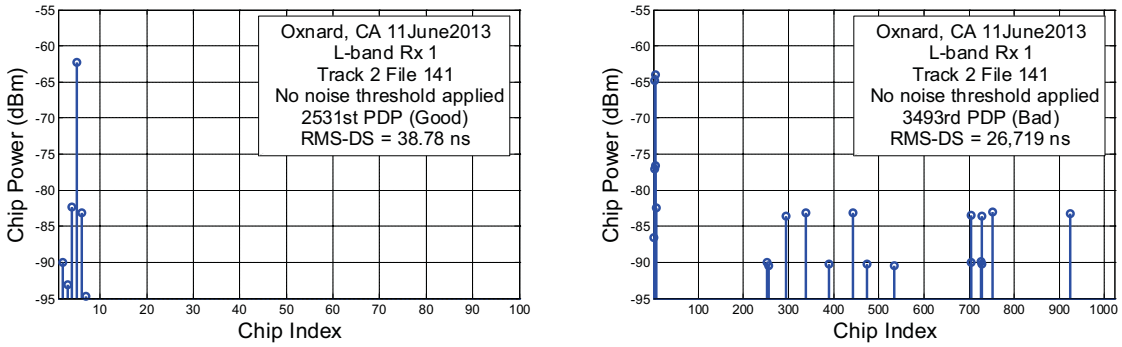

Figure C.2. Example "Good" and "Bad" PDPs in L-band.

For C-band analysis, we collect all the noise chips in a PDP and from sets of PDPs. These noise chips appear infrequently, and are introduced due to the relatively low signal-to-noise ratio (SNR); in this condition, the sounder's 30 dB threshold lies below some of the larger noise chip values. Even with the low SNR, typically only a few (and often zero) noise chips exist in a given PDP.

In the case of L-band, we remove the entire PDP from the data set if noise chips are found (again, at large and likely unrealistic values of delay). Noise chips exist in L-band PDPs even when the SNR is relatively large, but fortunately, only isolated PDPs have this problem. (The reason for this phenomenon is unclear, but as noted in prior observations, the L-band sounders also often produce PDPs with an unrealistically large number of MPCs and consequent unrealistically large RMS-DS).

C.1 C-band Analytical Threshold

The Oxnard data for large link distances is nearly ideal for developing our noise thresholding algorithm because Oxnard is one of the "cleanest" environments possible: the over-ocean setting has a minimal number of multipath reflections beyond that of the sea-surface reflection; as we have noted, the sea-surface reflection is unresolvable at long link distances, and other MPCs are intermittent.

Track 3 is a route that had the aircraft flying directly away from the GS with link distances of approximately 20 to 45 km. The aircraft altitude for this track was approximately 800 m.

Each PDP contains 1023 chips. The LOS component is rotated to the 5th chip (this is delay alignment). It is extremely likely that all chips with index larger than 500 (relative delay greater than 10 microseconds, or excess path length of ~3 km) are attributable to noise. We have strengthened confidence in this claim by observing that these noise chips appear in isolated PDPs—as noted, a true MPC would persist for at least several (likely tens to hundreds of) PDPs. We found no noise chip persistence beyond a single PDP. Since chips 951 to 1023 are removed due to the "false MPC" (described in prior reports, and due to some RF interaction between the aircraft bomb bay doors and the sounder), chips 501 to 950 were used to estimate the noise distributions.

As shown in Figure C.3, the distribution of the power of noise chips (in dBm) is bi-modal in shape (cf. Figures B.6-B.9). Since we want to set an upper noise threshold, the effect of the noise from the left mode (due to the sounder's internal noise) is expected to be minor, i.e., the probability of sounder internal noise exceeding our threshold will be negligible. Thus we consider only the right mode due to the aircraft electronic noise for our analysis. Histograms for the noise from this mode alone are shown in Figure C.4, where we have used a cutoff of -86.5 dBm as the lower limit of the aircraft noise mode.

For simplicity we model the aircraft noise as Gaussian (normal) in distribution, in dB units (hence this mode is strictly modeled as lognormal). As can be seen from Figure C.4, the Gaussian approximation is quite good for C-band Rx1, slightly less so for C-band Rx2, although the fit in the right part of the distribution for Rx2 is good. We could also have employed other distributions to fit

the aircraft noise (e.g., Weibull or gamma), but their complexity and the larger effort required for computing thresholds makes them less appealing than the Gaussian. In addition, the resulting agreement with empirical probability values we obtain with the Gaussian is very good. Hence seeking better fits would not yield substantial improvement to our thresholding algorithm performance. The Gaussian distribution we use has probability density function (pdf)

$$f_N(x) = \frac{1}{\sqrt{2\pi\sigma^2}} \exp[-\frac{(x-\mu)^2}{2\sigma^2}] \qquad \text{(C.1)}$$

where N denotes the noise random variable in dBm, μ is the mean in dBm, and σ the standard deviation in dB (x is the dummy variable of the pdf). To specify the distribution completely then requires that we obtain values for μ and σ. We have done this using the maximum-likelihood algorithm, which is conveniently implemented in Matlab's® distribution fitting tool. The analytical distributions are shown in Figure C.5, with the means and standard deviations listed in the text boxes.

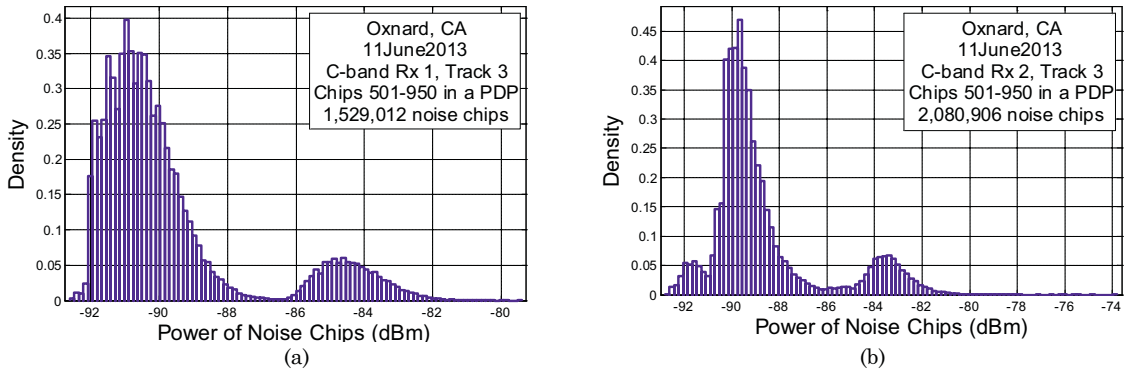

Figure C.3. Distribution of power of noise chips – all chips recorded by sounder for segment of FT3, for (a) C-band Rx 1; (b) C-band Rx 2.

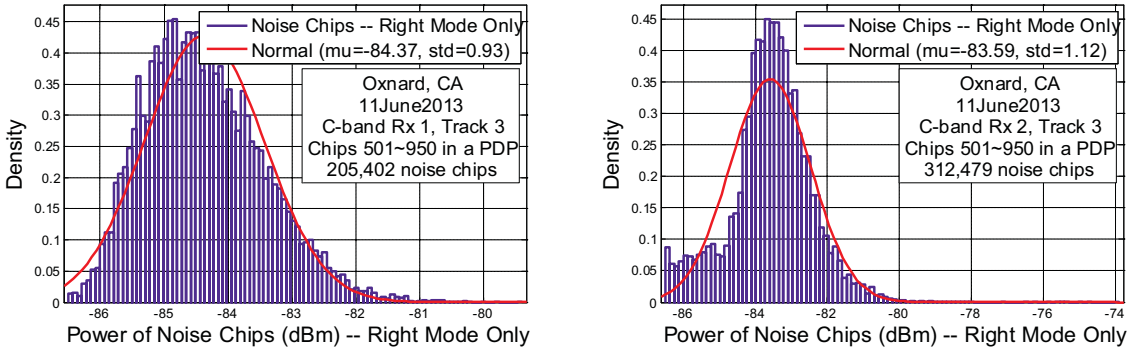

Figure C.4. Distribution of power of noise chips for the right (aircraft noise) mode only, for (a) C-band Rx 1; (b) C-band Rx 2.

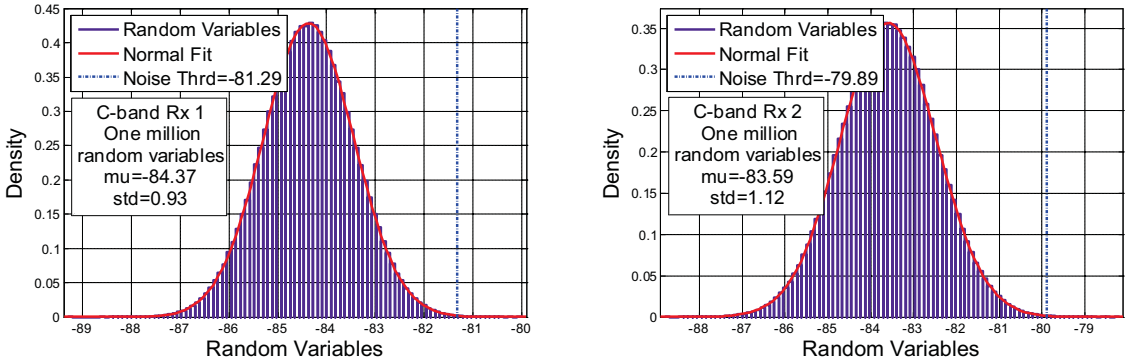

Figure C.5. Analytical distribution of noise chip power (dBm) for (a) C-band Rx 1; (b) C-band Rx 2.

We have selected a false alarm probability of 0.0005. This is the probability of mistaking a noise spike for a true MPC. Although the noise does not appear uniformly across PDPs, one can interpret this in an approximate sense as allowing only 5 PDPs out of every 10,000 to contain a mistakenly-labeled MPC, on average. For any PDPs that do retain the noise samples, our noise removal algorithm's subsequent steps are applied to remove them. Analytically, we have that the false alarm probability P_{fa} is

$$P_{fa} = Q\left(\frac{N_T - \mu}{\sigma}\right) \tag{C.2}$$

where N_T is the threshold to be determined given the desired P_{fa}, and μ and σ are the fitted values of noise mean and standard deviation. The Q-function is the tail integral of the zero-mean, unit-variance Gaussian pdf. For C-band Rx1 we obtain N_T= -81.29 dBm, and for C-band Rx2 N_T= -79.89. Note that for false alarm probabilities 0.001 and 0.0001, the thresholds change by very small amounts. To implement the noise thresholding, all the recorded chips smaller than N_T are set to an extremely small value (-220 dBm in our software program), effectively removing them from all the PDPs.

C.2 C-band Empirical Threshold

An empirical noise threshold is computed for each data file (10,000 PDPs) separately. The noise chips (index 501 to 950) are collected for all the 10,000 PDPs. Example distributions (Oxnard, Track 2, last data files) of noise chip power are shown in Figure C.6. The noise threshold can be found using the same false alarm probability of 0.0005 by finding the value below which 99.95% of the probability mass lies. These empirical thresholds for the example files in Figure C.6 were found to be -81.06 dBm for C-band Rx1 and -80.25 dBm for C-band Rx2. As with the analytical method, to implement the thresholding, all chips smaller than the noise threshold are set to an extremely small value (-220 dBm).

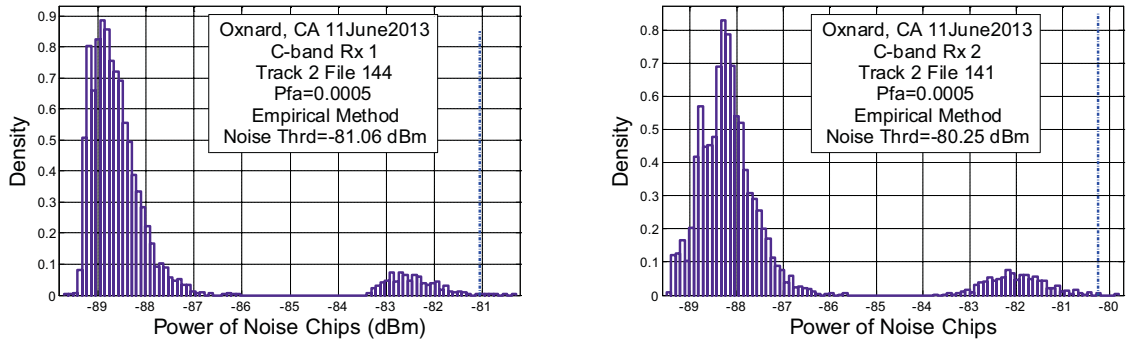

Figure C.6. Example distribution of noise chip power (dBm) of (a) C-band Rx 1; (b) C-band Rx 2.

The empirical noise threshold varies somewhat for different data files. We illustrate this in Figure C.7, which shows the empirical noise threshold for a few hundred files from FT2 and FT3. Values near -85 dBm and below are obtained when only the internal sounder noise mode is present—this illustrates that for some (albeit brief and randomly occurring) time periods, the aircraft electronic noise appears to be *absent*! For most of the files from Rx2, the empirical threshold value is near -80 dBm, with some values 1-2 dB smaller; for the files from Rx1, a larger fraction have thresholds between -82 dBm to -84 dBm. To be most conservative, the largest threshold should be used, but this carries the risk of removing potentially weak but real MPCs. From the results in Appendix B that show aircraft electronic noise distributions from a different flight test (Cleveland), we concluded that the aircraft noise appeared to be statistically stationary, whereas results in Figure C.7 indicate that it is not—the variation in threshold (between ~ -80 dBm to ~ -84 dBm) over multiple files may simply be due to the different realizations of the aircraft noise samples. It is the complete (yet rare) *absence* of the aircraft noise mode that evinces non-stationarity.

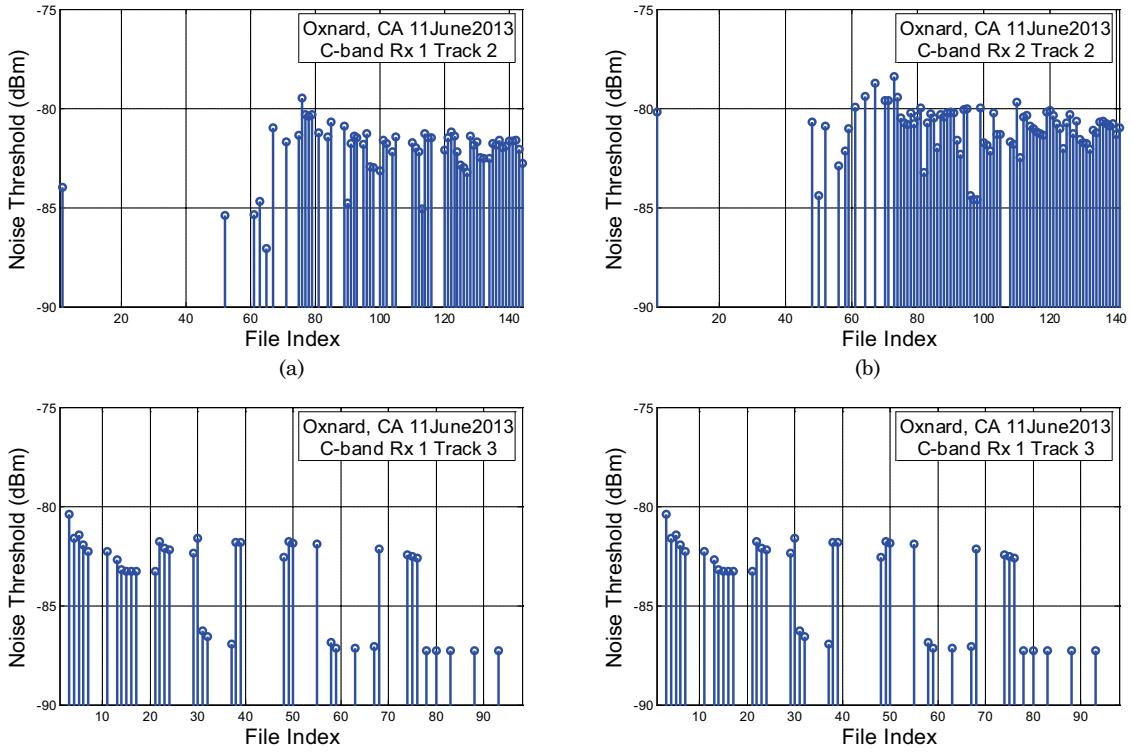

Figure C.7. Example empirical noise threshold (dBm) vs. file index for multiple files for (a) C-band Rx1 Track 2; (b) C-band Rx2 Track 2; (c) C-band Rx1 Track 3; (d) C-band Rx 2 Track3.

C.3 Comparison of C-band Thresholding Methods

Since it is not necessarily obvious which thresholding approach may be best, here we briefly compare results between the two methods. The original RMS-DS vs. PDP index for an example set of two files for the two C-band receivers is shown in Figure C.8. No thresholding—other than the sounder's 30 dB thresholding, has been applied, so RMS-DS values are often very large, over 2 microseconds. The RMS-DS resulting from application of our analytical threshold is shown in Figure C.9, and that resulting from application of our empirical threshold is shown in Figure C.10. As can be observed, both thresholding approaches *significantly* reduce the RMS-DS values by removing the relatively large-amplitude noise components that appear at arbitrary (and large) values of delay.

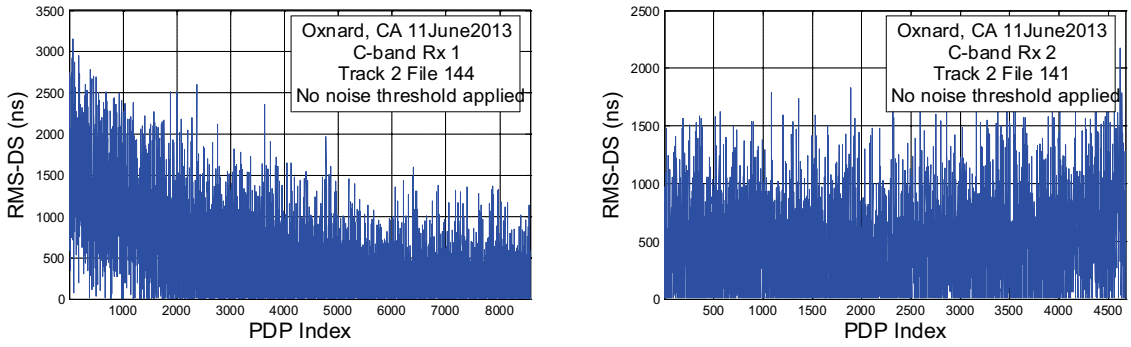

(a) (b)

Figure C.8. Original RMS-DS data for example files, no noise threshold applied, for (a) C-band Rx 1; (b) C-band Rx 2.

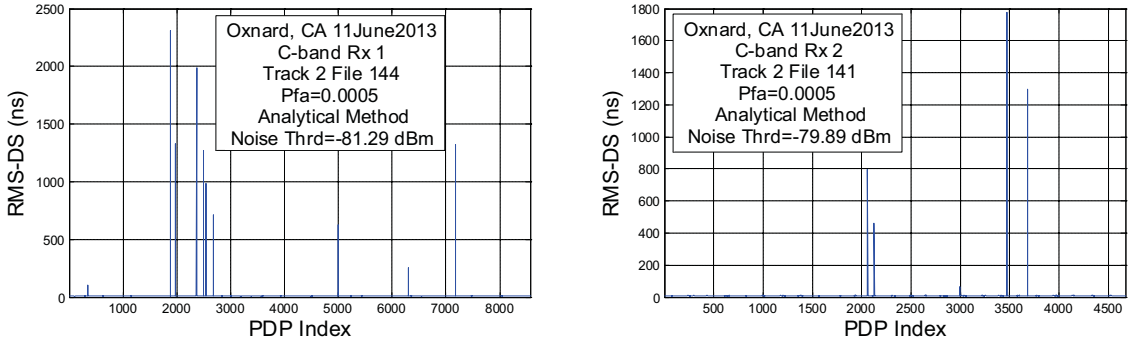

(a) (b)

Figure C.9. RMS-DS vs. PDP index for example files of Fig. C.8, after application of analytical threshold, for (a) C-band Rx 1; (b) C-band Rx 2.

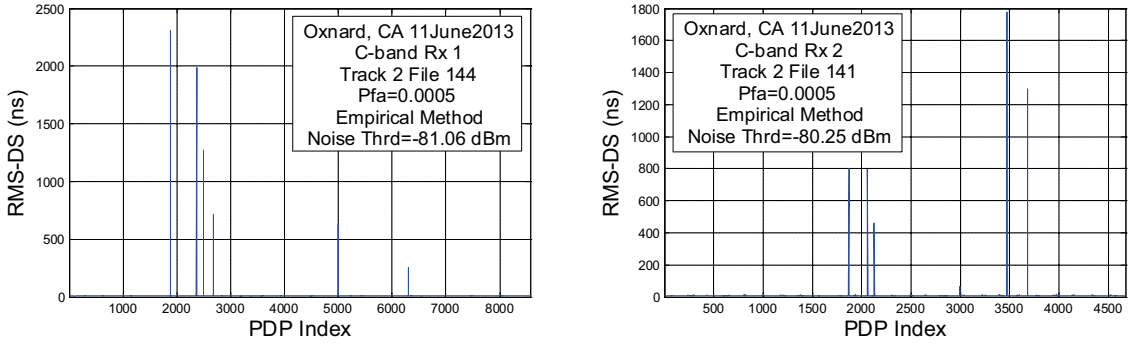

(a) (b)

Figure C.10. RMS-DS vs. PDP index for example files of Fig. C.8, after application of empirical threshold, for (a) C-band Rx 1; (b) C-band Rx 2.

Both the analytical and empirical methods have good performance, and the noise threshold values for the two methods are very close. The remaining large RMS-DS spikes in Figures C.9 and C.10 are due to some noise chips with relatively large value (above both the sounder's 30 dB threshold and either the analytical or empirical noise threshold). These are not removed by our algorithm. The RMS-DS spikes are examined in the third and fourth steps of our noise removal. Parameters of the two C-band methods are listed in Table C.1.

Ultimately though, given the variation seen across different files with the empirical threshold, the analytical threshold, derived using the largest set of samples, will be our preferred thresholding method. Noise samples will need to be analyzed in future data sets to see if the value of the threshold should be adjusted for each flight test.

Table C.1. Parameters of C-band noise thresholding algorithms.

Rx	**Chip Indices for Noise Analysis**	**Total # Noise Chips**	**# Noise Chips in Aircraft Noise Mode**	**Minimum Value of Aircraft Noise Mode (dBm)**	
1	501-950	1,529,012	205,402	-86.5	
2	501-950	2,080,906	312,479	-86.5	
Rx	**Mean of Aircraft Noise Mode (dBm)**	**Std Dev of Aircraft Noise Mode (dB)**	**P_{fa}**	**Analytical Noise Threshold (dBm)**	**Example Empirical Noise Threshold (dBm)**
1	-84.37	0.93	0.0005	-81.29	-81.06
2	-83.59	1.12	0.0005	-79.89	-80.25

C.4 L-band Empirical Threshold

As in the C-band PDPs, since the direct-sequence spreading code length is also 1023 for the L-band sounder, each L-band PDP contains 1023 chips. The PDPs are also delay aligned by circularly shifting the LOS component to the 5th chip. Here again we are confident that all chips with index larger than 50 are attributable to noise only (the same value of relative MPC delay as the 500-chip C-band value). We again ensure that chips we classify as noise do not persist beyond a single PDP. Thus for the Oxnard L-band data we classify chips 51 to 1023 as noise chips. As noted in regard to Figure C.2, if many noise chips exist in a PDP, the PDP is regarded as "bad," and is hence removed from the data set.

Plots of RMS-DS vs. PDP index for example L-band files, both before and after application of the empirical noise threshold, are shown in Figures C.11 and C.12. As with the C-band results, some large RMS-DS spikes still exist after thresholding. They too will be removed by subsequent steps of our algorithm.

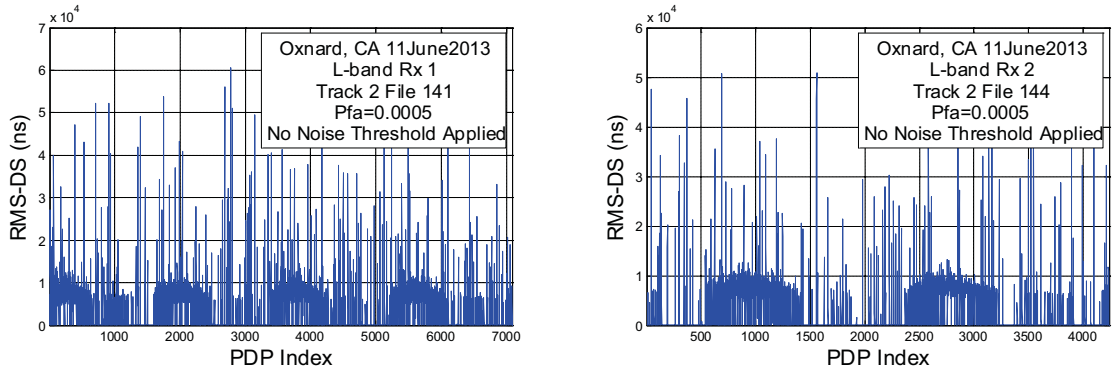

(a) (b)

Figure C.11. Original RMS-DS data for example files, no noise threshold applied, for (a) L-band Rx1; (b) L-band Rx2.

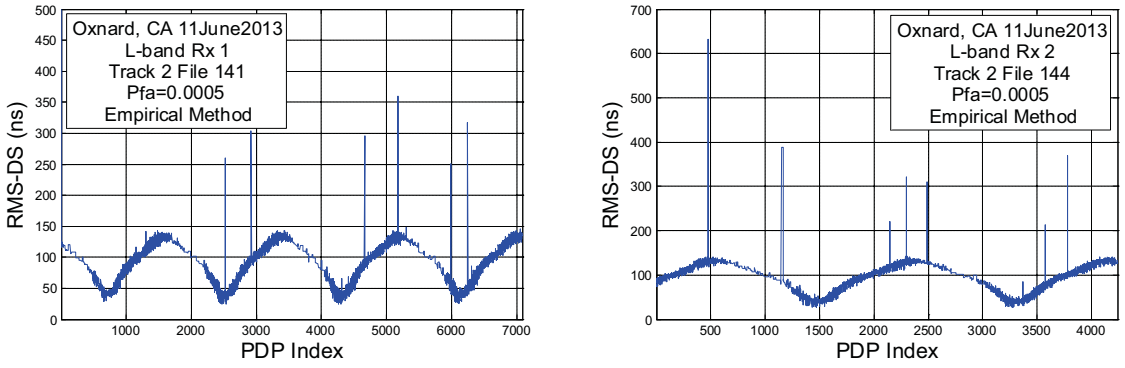

(a) (b)

Figure C.12. RMS-DS vs. PDP index for example files of Fig. C.11, after application of empirical threshold, for (a) L-band Rx1; (b) L-band Rx2.

C.5 RMS-DS Threshold

In this processing step, the RMS-DS of the noise-thresholded PDPs are compared with a threshold, denoted S_T. This threshold will vary depending on the test environment, and hence must be chosen with care. As noted, in complex environments with many MPCs expected, we may not use any RMS-DS threshold at all, or we might be able to establish some reasonable value of RMS-DS threshold, e.g., K times the mean RMS-DS of a data file, for some moderate value of K such as 3 or 4. For the case of our long-link-distance data taken in Oxnard, since we expect only the LOS and (unresolvable) sea-surface reflection, a value of S_T equal to 15 ns for C-band and 150 ns for L-band is reasonable. These values are near the maximum single-path delay spreads measured in back-to-back laboratory tests. Example RMS-DS vs. PDP index results for all four receivers, after application of these RMS-DS thresholds, are shown in Figures C.13 and C.14.

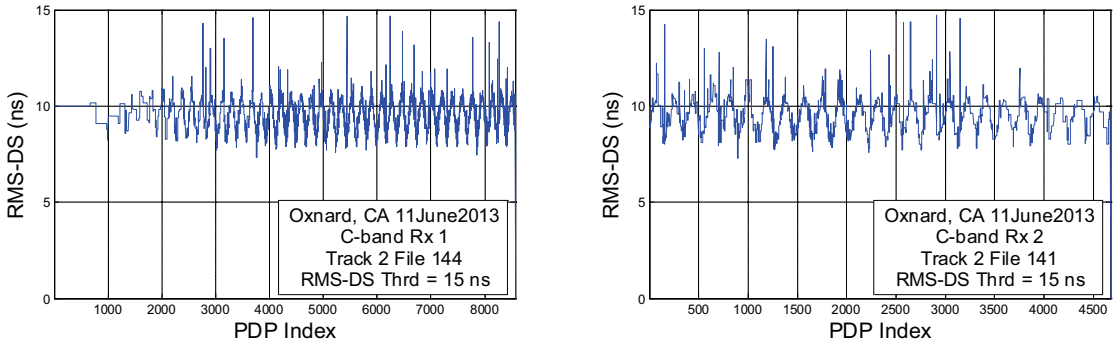

(a) (b)

Figure C.13. RMS-DS vs. PDP index after application of RMS-DS threshold, for (a) C-band Rx1; (b) C-band Rx2.

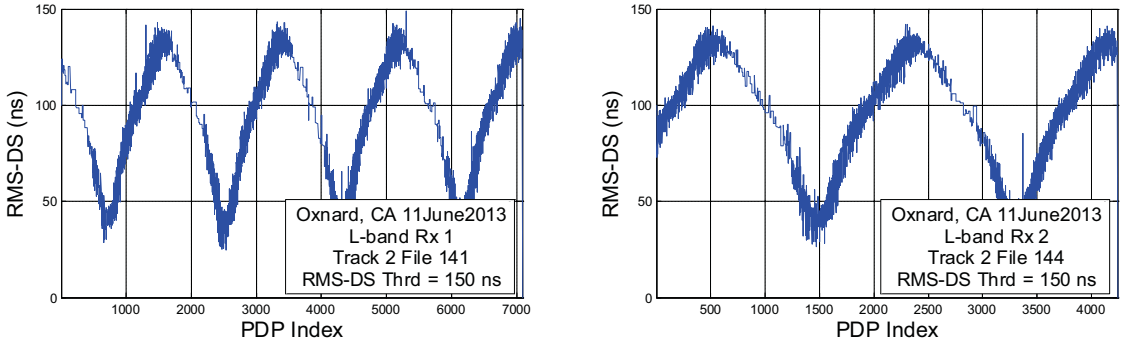

(a) (b)

Figure C.14. RMS-DS vs. PDP index after application of RMS-DS threshold, for (a) L-band Rx 1; (b) L-band Rx 2.

C.6 Testing MPC Persistence

We have already discussed this processing briefly in prior sections in which we described how we ensured that all chip values we classify as noise do not "persist" beyond a single PDP. Here we elaborate. For any PDPs that we retain after RMS-DS thresholding in step 3 (or step 2 if step 3 is not used), we again need to classify as "valid" or "questionable." In the simple over-sea environment, the classification of "questionable" again would mean PDPs with large RMS-DS. No such PDPs exist in the plots in Figures C.13 and C.14, but in more complicated environments, where we may be unsure of how large RMS-DS may be, and hence will not apply any RMS-DS threshold, we will need to test MPC persistence.

We illustrate this using Figure C.15. This figure shows a plot of a hypothetical sequence of PDPs, $P(\tau;t)$; each individual PDP is taken along the τ (delay) axis, at a fixed value of time t_i, with this time typically denoted PDP Index. In principle, each PDP is the response to an impulse input at time t_i. These input impulses are shown at delay τ=0 along the time axis. For the sequence of PDPs in Figure C.15, there are three valid MPCs that persist over multiple PDPs, at delays denoted τ_0, τ_1, and τ_2. The fading of these MPCs over time is also indicated. A noise spike is shown at delay τ_3 (and time t_3). This noise spike is *isolated*, and does not last beyond a single PDP, hence it is easily identified and removed. Also note that valid MPCs can appear and disappear, as illustrated for the MPC at delay τ_2; such disappearance is often termed a "death," and the appearance (or re-appearance) is termed a "birth." As these intermittent MPCs persist, they are also easily identified as valid.

Algorithmically, we test persistence as follows. For any PDP with a large value of RMS-DS, say PDP with index i, we can check the persistence of any potential MPC at chip value m over time. (Typically m ranges from 11 to 1023, since the strongest chip—LOS when present—is aligned to be

the 5th chip, and the pulse shape can extend an additional 5 chips [5].) If the m^{th} chip is not present in some number W of adjacent PDPs (indexed *i-W/2, i-W/2+1,…i-2, i-1,* and *i+1, i+2, …i+W/2,* with W a positive even integer), this m^{th} chip is very likely noise and will be removed, and RMS-DS will be re-computed. The length in time over which the *W+1* PDPs are checked is denoted the *persistence window*. Even a value for W as small as 2 (3 consecutive PDPs) should be sufficient for most cases, but we may need to allow for larger values of W in some circumstances.

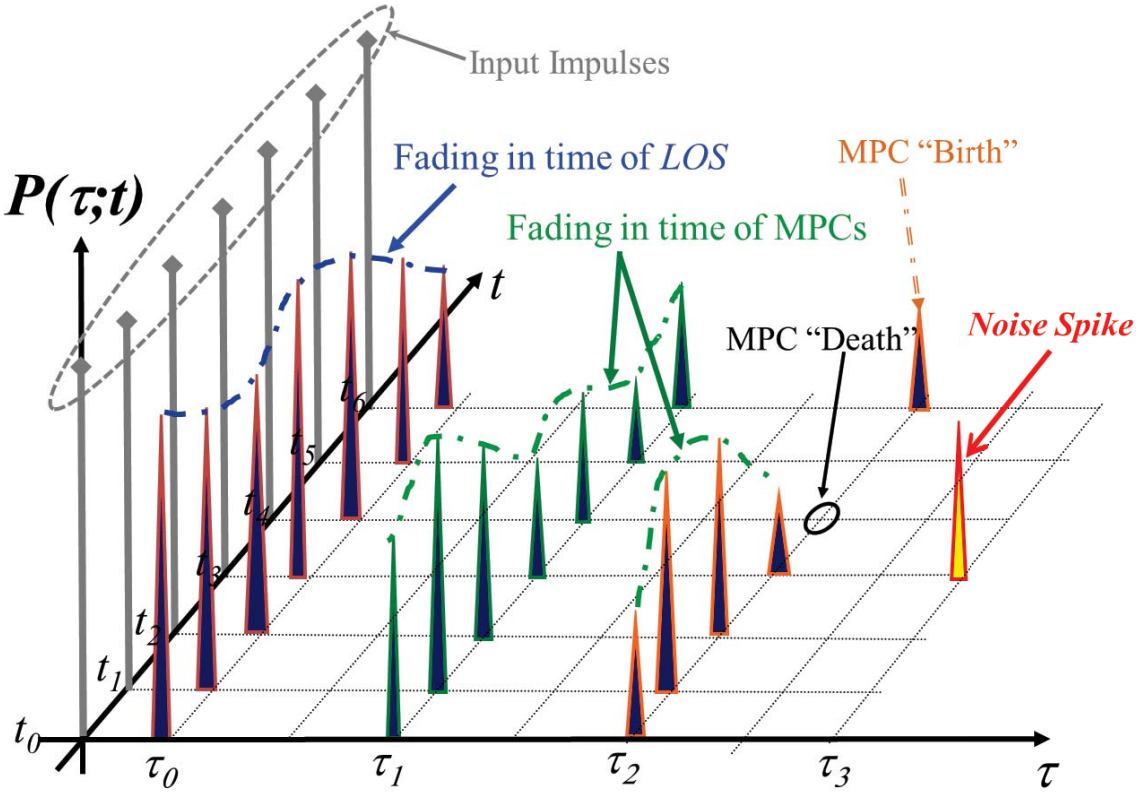

Figure C.15. Conceptual set of PDPs vs. time, showing (three) valid MPCs, and a noise spike.